EVALUATING AND IMPROVING THE PERFORMANCE OF RADAR TO ESTIMATE RAINFALL

A thesis presented to
the Faculty of the Graduate School
at the University of Missouri-Columbia

In Partial Fulfillment
Of the Requirements for the Degree
Master of Science

---

by

GEORGE LIMPERT

Dr. Neil Fox, Thesis Supervisor

August 2008

The undersigned, appointed by the dean of the Graduate School, have examined the thesis entitled

EVALUATING AND IMPROVING THE PERFORMACE OF RADAR TO
ESTIMATE RAINFALL

presented by George Limpert,

a candidate for the degree of master of science,

and hereby certify that, in their opinion, it is worthy of acceptance.

Dr. Neil I. Fox

Dr. E. John Sadler

Dr. Kannappan Palaniappan

Acknowledgements

I would first like to thank my Lord and Savior Jesus Christ. Without Him, I would not be here at the University of Missouri finishing up my M.S. and heading on my way to the University of Nebraska-Lincoln.

I would like to thank the University of Missouri. In particular, I would like to thank my advisor, Dr. Neil Fox for his guidance and direction in this research and for giving me the opportunity to attend MU and seeking funding for me.

I would like to thank the other members of my committee, Dr. John Sadler and Dr. Kannappan Palaniappan. I would in particular like to thank the USDA-ARS Cropping Systems and Water Quality research unit for providing me with a topic to research and for funding me for my three years at MU.

There are way too many students to thank along the way, so I will only thank a few. If I haven't mentioned you but you helped me along the way, I thank you, but just can't mention it here without writing an extremely long essay.

I would like to thank Steve Lack for giving me ideas and guidance in my research. I would also like to thank Steve for convincing me to make many a trip to McDonalds, talking Cleveland Indians and Penn State smack to me, and for making my time in 1-77 a fun time.

I would like to thank Chris Schultz for helping me find my way around the department and become accustomed to meteorology. I'm studying meteorology here because in part people like Chris welcomed me and gave me plenty of reasons to stay at MU.

I would like to thank Katy Morgan for working with me on my first conference presentation of my own and presenting with me. My first year in the department would not have been the same. I would also like to thank Katy for doing her best to convince me not to root for Kansas. Whether or not she was successful remains to be seen. Go Nationals!

I would like to thank Jeff La Montia for talking to me many a time about meteorology for hours. I would also like to thank Jeff for talking plenty of smack to me about the Nebraska Cornhuskers.

I would like to thank Kelly Scott for spending many hours with me in the GIS lab doing tedious work to process lots of radar data. I'm sure glad I didn't do all the data processing on my own.

I would like to thank Tara Travers for working with me on the part of the algorithm that distinguishes between rotating and non-rotating storms and for presenting this work with me. I also thank Tara for giving me plenty of encouragement to keep working and to finish my M.S. and my thesis. Rock Chalk Jayhawk KU! (Sorry, Katy) This one's for you.

I would like to thank Brittany Perrin for working with me on many projects, including some very cool tropical meteorology projects. I would like to thank Brittany for helping me prepare for my defense and giving me the needed encouragement and criticism. Go Royals!

Finally, I would like to thank my family for their encouragement and support to complete my M.S. and to finish up my thesis.

Thank you!

Table of Contents

List of Figures

List of Tables

Abstract

A network of 10 rain gages reports data from the Goodwater Creek catchment in central Missouri. Because such a network is expensive to operate, it could be useful instead to use only a few gages and augment the observations with radar-estimated rainfall. The purpose of this work is to evaluate the differences between using many gages and using only radar with, at most, a single gage.

Additional work was done to develop an algorithm for the purpose of improving the techniques used to estimate rainfall from radar observations. Frequently a single Z-R relationship is applied to the entire scanning area over which a radar observes. The purpose of the algorithm was to evaluate the characteristics of storms observed by radar and to select different Z-R relationships for individual portions of the scanning area. In addition to developing the algorithm to demonstrate the concept, a comparison was done to evaluate the differences between using a single Z-R relationship and multiple Z-R relationships simultaneously in one domain.

It was found that applying a single Z-R relationship to the entire domain underestimated rainfall over the catchment. Applying multiple Z-R relationships increased the estimated rainfall accumulation in most instances, often overestimating the rainfall accumulation. The results

strongly suggest tha the appropriate Z-R relationship to relate reflectivity to rain rate, varies highly spatially and temporally, even within a single storm.

Chapter 1

Introduction

Rainfall plays an important role in the water cycle by providing water to the surface of the Earth. Rain sustains agriculture and provides water to streams, which is important for aquatic life and navigation. Excess rainfall, however, can be quite hazardous by causing flooding, which is a significant threat to both life and property. Because of the important role of rainfall in many aspects of life, it is not only worthwhile to observe where rainfall has occurred and how much has fallen but also to forecast rainfall. The purpose of this project is twofold: to evaluate a method for improving observations of rainfall totals and to develop an algorithm that is useful in estimating rainfall from radar observations.

Observing rainfall is useful for evaluating moisture available for agriculture and determining how much will run off the surface into streams and rivers. For example, in moderate amounts, rainfall is necessary to grow crops, fill reservoirs, and maintain flow in rivers for navigation and shipping. However, in excess, rainfall runs off the surface in large amounts and can cause streams and rivers to overflow their banks and flood. Additionally, runoff can cause transport and loss of sediment and chemicals. Observations of rainfall are a necessary input in monitoring and forecasting soil moisture, drought, and river stages, as well as monitoring and modeling water quality.

Forecasting rainfall is yet another step removed from observing soil moisture, drought, and flow in rivers and streams and provides an opportunity to produce forecasts with longer lead time. Accurately forecasting heavy rainfall can allow for warning of floods before rainfall occurs instead of monitoring rainfall and warning based on observations. Additionally, such information is useful in agriculture to improve irrigation practices and the effectiveness of applying fertilizer, pesticides, and herbicides to crops. Effective forecasting of rainfall is very useful in agriculture and preparedness for flooding.

One purpose of this project is to evaluate a method to improve observations of rainfall. Traditionally, rainfall has been observed using only rain gages at the surface. Gages provide ground truth data, albeit with several known sources of error. Rain gages are also limited because they are observations at a single point and are often spaced sparsely and report data at infrequent intervals. Weather radars measure reflectivity, which can be related to rainfall rate. Radar observations occur much more frequently and at much higher resolutions than most rain gage networks can offer. Additionally, radar observations provide areal coverage instead of only point observations from rain gages. Although radar observations have many known limitations, they offer an attractive alternative to measuring rainfall through traditional rain gage methods. One purpose of this work is to evaluate the differences in rainfall observations from rain gages versus rainfall estimates produced from radar-observed reflectivity.

Additionally, an algorithm was developed to estimate rainfall using multiple conversions from radar-measured reflectivity to rainfall rate within a single radar image. This was done because the properties of rainfall vary greatly in space and time, and using a single conversion from reflectivity to rain rate over an entire radar scanning area for a whole event may not produce reasonable estimates of rainfall. The usefulness of the algorithm was evaluated using the same cases used in the intercomparison between rain gages and other radar-derived rainfall estimates. The purpose of developing the algorithm and performing this second intercomparison was to evaluate the difference between using a single Z-R relationship and multiple Z-R relationships within a single radar scanning area or domain during an event.

The goal of this work was to develop two seemingly unrelated projects that could be related through future work. The first part of this document describes the efforts to evaluate the performance of estimating rainfall using observations from radar. Following the discussion of radar estimates of rainfall, an algorithm is described to attempt to improve the estimation of rainfall, particularly for the highest intensity of rainfall during an event. Although an evaluation of algorithm performance is presented, the crux of the work was to develop the algorithm. These two projects are presented with the hope that future work will improve upon rainfall observations and forecasts.

1.1. Evaluation of Radar Estimates of Rainfall

Traditionally, rain gage observations have been used in many hydrological applications such as modeling of runoff and water quality. However, there are many drawbacks to using rain gages in such applications. Most rain gage networks report data with a very sparse spatial and temporal resolution. Additionally, rain gages are prone to sources of error such as evaporation, splashing, wind, and loss of rain during the tipping of buckets. Weather radar observations offer an alternative to estimating rainfall for hydrological purposes.

Radars measure reflectivity due to particles and objects in the atmosphere. Reflectivity has been related to rainfall through empirically-derived equations. Through these equations, it is possible to estimate rainfall using observations from weather radars. Radar observations are at a much finer spatial resolution than nearly all rain gage networks and report data much more frequently than most rain gages. Radars are also not prone to the same errors that frequently occur with rain gages. However, there are other sources of error that arise from using radar observations such as wind drift, hail, bright banding, and in determining an appropriate relation between reflectivity and rain rate.

The purpose of this work was to perform an intercomparison between rain gage observations and radar-estimated rainfall over central Missouri. A dense rain gage network is located within a small catchment and rain gage observations are reported every two minutes. Such a network is atypical of most rain gage networks but is useful for evaluating the performance of radar at estimating the characteristics of rainfall. A sparse rain gage network is also present around the catchment using data from a variety of sources including the National Weather Service (NWS), Federal Aviation Administration (FAA), and the Missouri Climate Center (MCC).

A challenge is presented in using radar observations because the area of interest is located approximately 130 km from the nearest radar. At this distance, the lowest beam is about 2,300 m above the ground. Because of the limited radar coverage over the rain gage network, errors such as bright banding and wind drift may be more pronounced than for areas nearer to the radar.

It is possible to attempt to correct for radar errors by calibrating the rainfall estimates using rain gage observations. One such product, the Multisensor Precipitation Estimator (MPE) is generated operationally and incorporates rainfall estimates from radar and satellite along with observations from rain gages. However, neither the MPE nor the rainfall estimates derived purely from radar data may accurately estimate rainfall over the rain gages in question. Therefore an additional step is to calibrate the rainfall estimates by matching a single gage with a rainfall estimate and correcting any bias in the rainfall estimate.

There were several goals of this work, which when considered together should provide a good evaluation of the usefulness of radar in estimating rainfall at fine temporal and spatial scales. The following steps were performed in evaluating the performance of the radar observations:

- Compare rainfall estimates from radar-derived products against rain gage observations at the gages
- Interpolate rain gage observations and compare total rainfall accumulation over the catchment against total rainfall accumulation estimated by radar
- Adjust radar-derived estimates of rainfall using observations from a single rain gage
- Compare adjusted rainfall estimates against rain gage observations at gages
- Interpolate rain gage observations and compare rainfall total accumulation in the catchment from gages against adjusted rainfall estimates

It is hoped that by performing all these steps the usefulness of radar estimates of rainfall can be evaluated. It is usually impractical to deploy a dense rain gage network such as the one used in this work. It is much more practical to operate a single rain gage and adjust radar-derived rainfall estimates using that single rain gage. Therefore, this study not only evaluates the usefulness of radar-derived rainfall products but also the need for a dense rain gage network to estimate rainfall.

1.2. Improving Radar Estimates of Rainfall

The goal of this work was to devise an algorithm to evaluate characteristics of rainfall that has been detected by radar and choose an appropriate conversion from reflectivity to rainfall rate. The purpose of the algorithm was to allow the conversion to vary from one part of a radar image to another instead of from one time to another or one event to another. The goal was to demonstrate that significant variations in estimating rainfall can be achieved by varying the conversion within a radar image. Several steps were performed to evaluate the characteristics of the precipitation.

Many methods exist to distinguish convection from stratiform precipitation and identifying storm cells using radar data. Much of the previous work on these topics relies on arbitrarily determined reflectivity thresholds. One purpose of this work was to develop an algorithm that objectively identifies precipitation structure and characteristics using not only reflectivity thresholds but also the spatial scale of structures. One application of identifying precipitation structures is to objectively choose on an appropriate conversion from reflectivity to rainfall rate at each pixel within a radar image. The goals of this work were to develop an algorithm using spectral analysis to identify different precipitation structures and to quantify the differences between using a single conversion from reflectivity to rainfall rate and an objectively determined conversion.

Spectral analysis has been used widely in some aspects of meteorology including analysis of climatic data, filtering of model output, and nowcasting. The Fourier Transform (FT) is a simple but well-studied method of performing spectral analysis in signal and image processing. Although more recent methods of spectral analysis such as the Wavelet Transform are becoming more widely used, the FT and related transforms remain widely used in many meteorological and non-meteorological applications. Because the FT is understood well and many algorithms have been developed to compute the FT rapidly even on very large data sets, the FT was the basis for the spectral analysis.

One goal of spectral analysis is to distinguish between convective and stratiform precipitation. Typically convection is characterized by small but strong reflectivity maxima and therefore strong horizontal gradients in reflectivity. Reflectivity tends to be weaker in stratiform precipitation and occurs over a wider area. Spectral analysis can be used to isolate different frequency bands or spatial scales within a radar image. Stratiform precipitation should be manifested by a signal in low frequency and high wavelength bands. Convective precipitation should exhibit a signal in higher frequency and lower wavelength bands.

An individual storm cell consists of a single updraft and downdraft. In many instances, multiple cells exist in clusters such as multicell clusters and squall lines. However, these larger structures still contain individual convective cells within. There is frequently a hierarchy of convective structures with large structures such as squall lines containing embedded individual cells. Spectral analysis is useful in identifying structures of multiple scales within images. By applying spectral analysis to radar imagery, both larger structures such as clusters and lines can be identified as well as the smaller individual cells.

It is of interest to identify rotating storms, because the rotation is indicative of a greater degree of organization than is found in disorganized thunderstorms. Rotation is found in supercell thunderstorms and is also frequently found in linear convective systems. Rotation indicates a greater degree of storm organization and may be useful to make inferences about other storm characteristics.

Using spectral analysis to distinguish between convective and stratiform precipitation, it is possible to select different relationships between reflectivity and rainfall rate for different portions of a radar image. Additionally, using properties of convective storms, including the presence of rotation, it is possible to further refine the choice of an appropriate relationship between reflectivity and rainfall rate. The goal of this work is to quantify the difference created from using a single relationship between reflectivity and rainfall rate for an entire radar image as opposed to selecting an appropriate relationship depending on properties of the image.

Therefore, the following goals were accomplished during this study:

- Develop an algorithm to select and apply multiple relationships between reflectivity and rainfall rate within a single radar image
- Quantify the differences between using multiple relationships between reflectivity and rainfall rate in a single radar image and using only a single relationship

Although some products of the algorithm may have other meteorological applications such as nowcasting, verification, and warning decisions, the primary purpose of this work was to produce an algorithm for estimating rainfall. Unlike previous algorithms for estimating rainfall, the algorithm developed for this work can apply multiple relationships between reflectivity and rainfall rate within the same radar image. It is believed that by selecting multiple relationships between reflectivity and rainfall rate in a single radar image that better estimates of rainfall can be produced using radar imagery.

Chapter 2

Background Information

This study is an intercomparison between rain gage observations and radar-derived estimates of rainfall. Background information on rain gages and radar-derived estimates of rainfall will be presented separately in sections. The rain gage discussion will focus on common errors associated with gages. Information specific to the gages used in this study will be described in the methodology. Background on radar scanning strategies will be presented with a focus on how rainfall is estimated and the errors associated with doing so.

2.1. Rain Gage Observations and Errors

Larson and Peck (1974) provide a good summary of rain gage errors and state that wind is the primary source of errors in rain gage observations. Increasing wind speeds also increase the gage errors. This is because turbulence near the gage carries raindrops or other hydrometeors past the rain gage that would have otherwise collected within the gage. Rain gage underreporting of rainfall is estimated to be around 10 to 20% on average and approximately 15% for a wind speed of 16 km h^{-1}.

2.2. Radar Estimation of Rainfall

Weather radars measure reflectivity (Z), which is in units of mm^6 m^{-3}. Frequently, radar reflectivity is presented on a logarithmic scale instead of a linear scale, in which case reflectivity will be given in decibels of Z (dBZ). Reflectivity increases as scattering by objects in the volume of air sampled by the radar increases. This can occur either due to more objects in the volume of air or as the objects increase in size.

Although radars do not directly measure rainfall, empirically-derived equations have attempted to relate reflectivity to rainfall rate. Such equations are known as Z-R relationships and frequently take the form of equation 2.1 (Marshall and Palmer, 1948).

$$Z = a R^b \tag{2.1}$$

In these equations, R is a rainfall rate, typically in units of mm hr^{-1}. The constants a and b are not typically expressed with units and are derived semi-empirically. An extended discussion of Z-R relationships is given in Appendix A. Operationally, a few Z-R relationships are made available to operators of WSR-88D radars. A single Z-R relationship is applied to the entire scan area at a given time to calculate a rain rate. The radar operator decides on a suitable Z-R relationship to apply to the scans.

The default Z-R relationship used by the WSR-88D radars for convective rainfall is (2.2) and is best used for deep moist convection during the summer.

$$Z = 300\,R^{1.4} \tag{2.2}$$

Although it is best suited for convective storms during the summer, it is also useful for any convection that is not tropical in nature.

One of the first Z-R relationships determined was for stratiform precipitation. Marshall and Palmer (1948) developed the equation in (2.3) to relate rain rate to radar reflectivity.

$$Z = 200R^{1.6} \tag{2.3}$$

This equation is still used operationally in many situations, including by the WSR-88D rainfall algorithm for some stratiform precipitation events. Later work has suggested that although this relationship is useful for many stratiform precipitation events, under some circumstances other Z-R relationships may provide better rainfall estimates. For example, other Z-R relationships may be substituted for stratiform precipitation during the cool season.

Although the Marshall-Palmer Z-R relationship is still used frequently for estimating rainfall from radar reflectivity, two additional Z-R relationships for stratiform precipitation were authorized in 1999 for use on the WSR-88D radar network, during the cool season (Belville, 1999). The Z-R relationship in (2.4) is best for cool season stratiform precipitation west of the continental divide and may also be used for orographic precipitation west of the continental divide. The Z-R relationship in (2.5) is for cool season stratiform precipitation to the east of the continental divide and is also useful for orographic precipitation east of the continental divide.

$$Z = 75\,R^{2.0} \tag{2.4}$$

$$Z = 130\,R^{2.0} \tag{2.5}$$

Rainfall from tropical convection is estimated using a Z-R relationship in (2.6) developed by Rosenfeld *et al*. (1993), which is referred to as the Rosenfeld Tropical Z-R relationship.

$$Z = 250\,R^{1.2} \tag{2.6}$$

In 1997, the Radar Operations Center (ROC) permitted radar sites to use this Z-R relationship (Belville, 1999).

Many errors are associated with estimating rainfall, which include beam blockage, anomalous propagation, beam filling, bright banding, and overshooting precipitation. Beam blockage occurs as the result of terrain partially or completely obscuring the radar beam. Anomalous propagation occurs as a result of strong refraction of a radar beam. Bright banding occurs as a result of strong scattering of the radar beam upon intersecting a layer of melting ice crystals. Beam filling occurs when only part of the volume that is being scanned scatters the beam. Overshooting precipitation occurs when the radar beam is completely above precipitation that is occurring below. Of these errors, beam blockage and anomalous propagation can and are frequently corrected without great difficulty. The other errors, however, can adversely affect detection and estimation of rainfall. Bright banding causes overestimation of rainfall whereas beam blockage and beam filling cause rainfall to be underestimated. An extended description of radar errors can be found in Appendix B.

The WSR-88D rainfall estimation algorithm (Fulton *et al.*, 1998) converts radar reflectivity detected by a single radar to a rainfall accumulation and performs some simple quality control operations on the data. The first step in the algorithm is detecting when the algorithm should calculate rain rates and accumulate precipitation. Precipitation accumulation begins when sufficient intensity and areal coverage of meteorological echoes are present within the scanning area of the radar.

Due to terrain around the radar, the beam may be partially or entirely blocked. If lower tilts are blocked by terrain, it may be useful to choose a higher tilt at which to observe reflectivity. A table is maintained for each radar to determine from which tilt it is suitable to be used to input reflectivity for the algorithm. The algorithm is restricted to using the lowest four tilts of a volume scan.

The algorithm attempts to limit underestimation of rainfall due to beam blockage by implementing Biscan Maximization, which chooses the higher reflectivity power to use in calculating rain rate at distances of 180 km and farther from the radar. Due to possible overestimation caused by bright banding, the technique is not used for areas closer to the radar. Additionally, for areas where beams are partially blocked, but not blocked enough to discard the tilt at that location, a correction factor is added to the reflectivity, which depends on the amount of beam blockage that occurs.

Vertical and horizontal continuity of echoes is used to perform some quality control on the reflectivity input to the algorithm. Ground clutter and other isolated unreasonably high reflectivity is removed by testing a range bin against neighboring range bins. If horizontal continuity is not present, the clutter is corrected by either setting the reflectivity to a very small value or setting the reflectivity at the point to the average of the neighboring range bins. Additionally, if all reflectivity areas within a range decrease by 75% from one tilt to the tilt above it, the lower tilt is discarded to remove echoes caused by anomalous propagation, which will be defined in section 2.3. Although some schemes that quality control radar data make use of radial velocity and other Doppler-derived products, the operational WSR-88D rainfall algorithm does not.

Following the quality control of radar reflectivity, a Z-R relationship is applied to the reflectivity derived from the hybrid scanning strategy. An appropriate Z-R relationship is determined subjectively by a forecaster based on the expected characteristic of the precipitation.

Because very strong reflectivity is likely due to hail and will produce unreasonably large rain rates, reflectivity is limited to a maximum of 53 dBZ through much of the United States with a higher threshold in regions near the Gulf Coast and a lower threshold in western parts of the United States.

Additional quality control is performed once a rain rate has been calculated. If, from one scan to the next, the rainfall over the entirety of the field changes at an unreasonable rate, the scan is discarded. This temporal continuity test further protects rainfall accumulations from contamination in addition to the earlier horizontal and vertical continuity tests.

2.3. Postprocessing of Rainfall Estimates

Rain rates can be integrated or summed over a period of time to produce rainfall accumulation products. These products include the gridded digital precipitation array (DPA) and polar one-hour, three-hour, and storm-total accumulations of rainfall.

The DPA contains a one-hour rainfall accumulation estimated by radar over the coverage area of the radar. Unlike the other products, however, the DPA is produced on the Hydrologic Rainfall Analysis Project (HRAP) grid. The HRAP grid contains square cells on a polar stereographic projection on the world. All of these products are part of level III radar data and are based only on radar observations and the choice of adaptable parameters by the operator of each radar.

The DPA data is also referred to as Stage I data. Unlike the other products produced as part of level III radar data, the DPA has a precision of 256 levels instead of 16. The DPA is used as the basis for additional postprocessing of the radar data.

Two additional products are produced when Stage II data is generated. Stage II data takes into account observations from rain gages in addition to radar observations. The gage observations used in creating Stage II data are from Automated Surface Observing Stations (ASOS) and the Hydrometeorological Data System (HADS) (Lin and Mitchell, 2006). Rain gage observations are compared against the DPA to compute whether across the entire coverage area of the radar the radar is underestimating or overestimating precipitation. The bias that is calculated is for the entire coverage area of the radar. Subjective interpretation is performed by a forecaster to determine whether rain gage observations are reasonable and to correct for any errors. In addition to computing the bias, a second product based only on rain gages is produced. The radar data, which has been adjusted for bias, is combined with the rain gage observations to produce Stage II data.

Stage III data uses data from multiple radars to produce a rainfall estimate over a larger area than the coverage of a single radar. When computing rainfall estimates for areas where coverage is provided by more than one radar, the forecaster may use a mean value or the maximum value. Gage data is used alone if radar data is not available for an area. When Stage III data is being computed, the forecaster may subjectively manipulate rain gage data and remove anomalous propagation. The forecaster can also manipulate how many observations are used for computing bias and whether the algorithm prefers radar or rain gage data for determining where rain is occurring and the intensity of rain.

2.4. Calibration of Rainfall Estimates

The Multisensor Precipitation Estimator (MPE) offers considerable improvements over Stage II and Stage III data. MPE data is now produced by River Forecast Centers instead of Stage II and Stage III data.

When producing MPE data, for areas covered by multiple radars, the lowest scan is chosen for which the beam is not blocked or contaminated by anomalous propagation. An improved method of calculating mean field bias (Seo *et al.*, 1999) is used in producing MPE output. Further adjustments are made at each point on the grid to adjust for local bias (Seo and Breidenbach, 2002). Optimal estimation is used to merge rain gage fields and radar derived fields (Seo, 1996). The climatological distribution of precipitation is also incorporated into the algorithm based on the Parameter-elevation Regression on Independent Slopes Model (PRISM).

Satellite data can be used to fill gaps in radar coverage in the precipitation field. Data from the Hydroestimator (Vicente *et al.*, 1998), which uses infrared satellite observations to generate precipitation estimates, is adjusted using rain gage observations that match with the surrounding radar-based estimates (Kondragunta *et al.*, 2005).

Although products resembling Stage III data, those using only rain gage data, radar mosaics, radar data adjusted for bias, and satellite data adjusted for bias are available as part of the MPE, the multisensor mosaic (MMOSAIC) is considered the best estimate of precipitation. Hourly MMOSAIC data are available for each river basin.

Chapter 3

Methodology of Intercomparison

The purpose of this intercomparison is to evaluate the differences between rainfall observed by gages at the surface and radar-derived estimates of rainfall in the Goodwater Creek catchment. The catchment is located in central Missouri near Centralia, Missouri. The first sections of this chapter focus on the characteristics of the catchment and the data sets used. Following these sections, a description of each case examined is provided. Then the procedure for evaluating the differences between the data sets is presented.

3.1. Catchment

The Goodwater Creek catchment is located in central Missouri and drains to the northeast. The southernmost part of the catchment is located in northeastern Boone County and the rest of the catchment is in western Audrain County. Water in the creek eventually drains into the Mississippi River. The extents of the catchment and the topography of the region are shown in figure 3.1. The area of the catchment is 70 km^2. Some of the land in the catchment is used for growing crops, including corn, wheat, sorghum, and soybeans. Fertilizers and herbicides used in the region may have significant impacts on water quality. Figure 3.2 shows the proximity of the Goodwater Creek catchment to nearby cities.

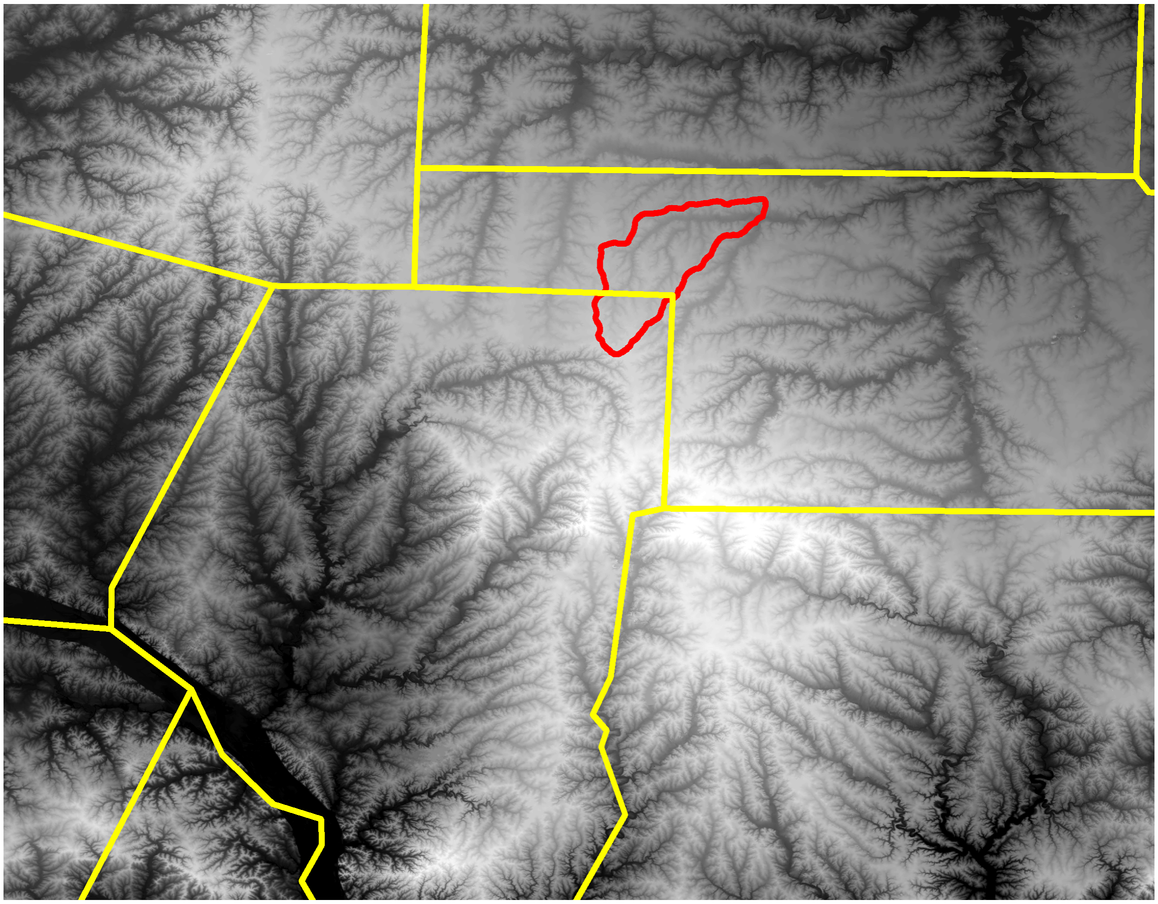

Figure 3.1: The outline of the Goodwater Creek catchment is shown in red over the topography of the region. Higher elevations are shown in brighter shades of gray and white. County lines are shown in yellow.

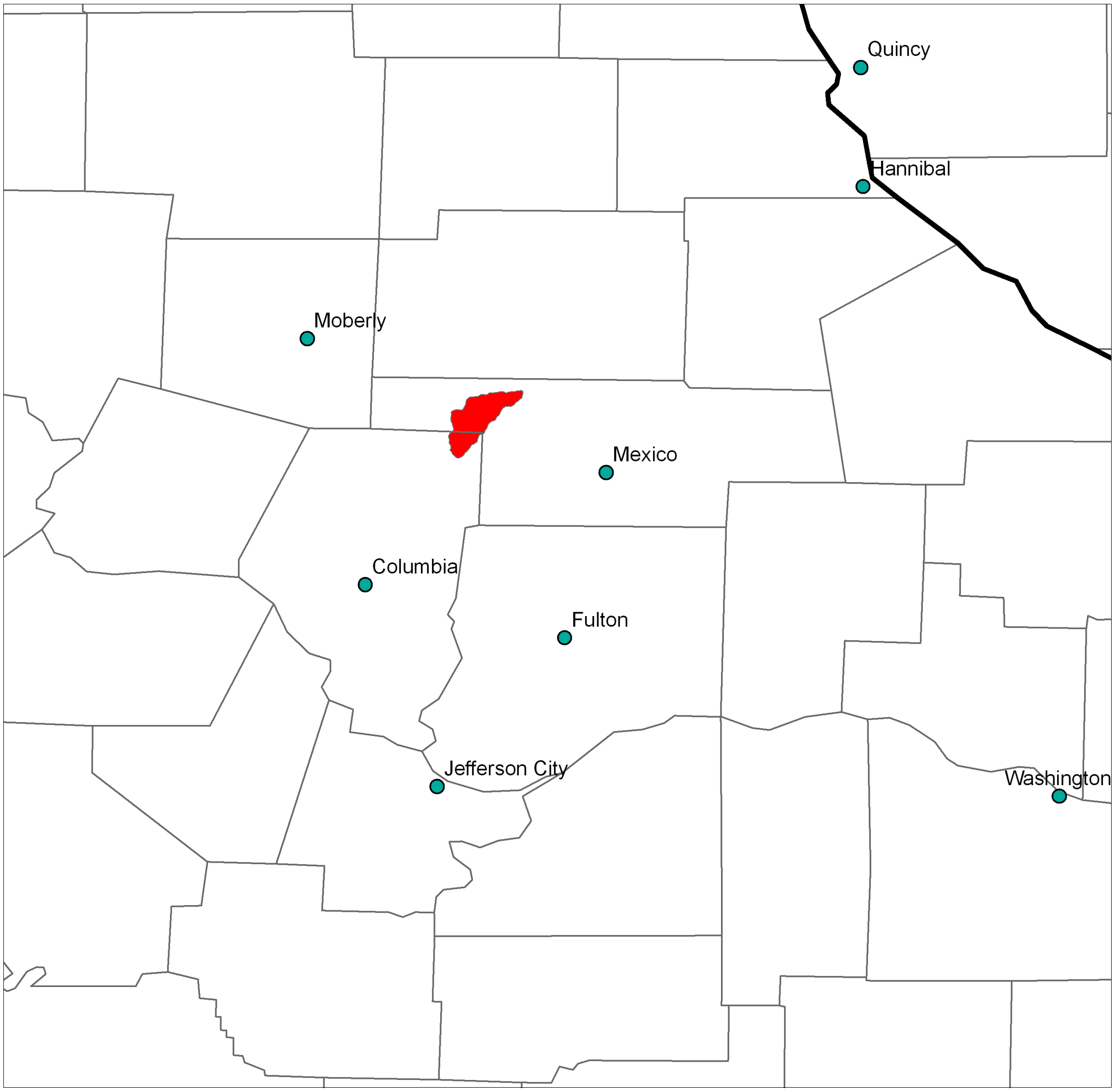

Figure 3.2: The Goodwater Creek catchment is shaded in red with county boundaries in thin lines and state lines in thick lines. Selected nearby cities are also shown on the map.

3.2. Rain Gages

Several rain gage networks are deployed in and around the Goodwater Creek catchment.This section will describe the three networks contributing data for use in this study.

3.2.1. Automated Surface Observing Stations

Automated Surface Observing Systems (ASOS) are deployed throughout the nation with many stations located at major airports. The network is operated by the Federal Aviation Administration (FAA) and the National Weather Service (NWS). ASOS stations report many data on an hourly basis including temperature, dewpoint, wind, sea level pressure, sky condition, and rainfall accumulation. Reports may be issued more frequently as needed under conditions of significant changes in weather.

Some older stations, known as Automated Weather Observation Systems (AWOS) are still deployed in some locations. These stations report less data than ASOS stations do. AWOS stations report every 20 minutes but do not issue more frequent reports during rapidly changing weather conditions.

The ASOS and AWOS stations used in this study are located in three states. In Missouri, stations are located in or near Columbia (KCOU), Jefferson City (KJEF), Kirksville (KIRK), Chillicothe (KCDJ), Sedalia (KDMO), Osage Beach (KAIZ), Fort Leonard Wood (KTBN), Rolla/Vichy (KVIH), Farmington (KFAM), Saint Louis (KSTL), Saint Charles (KSET), and Chesterfield (KSUS). Illinois stations used are located in or near Pittsfield (KPPQ), Alton (KALN), and Quincy (KUIN). One station, Keokuk (KEOK), is located in extreme southeastern Iowa. This network shall be referred to as the ASOS network.

ASOS and AWOS stations use tipping bucket gages to measure rainfall. Many stations also have a precipitation discriminator to distinguish between different types of precipitation such as rain, freezing rain, ice pellets, and snow.

3.2.2. Missouri Climate Center Stations

The Missouri Climate Center (MCC) operates a number of stations throughout Missouri. These stations report data every five minutes. However, data is archived on an hourly basis. Therefore when accessing past data such as for this study, only hourly data are available, even though the stations report every five minutes. MCC stations report temperature, dewpoint, wind, precipitation, and other data that vary from one station to another.

The MCC stations used in this study were located in or near Linneus, Brunswick, Auxvasse, Green Ridge, Versailles, Cook Station, Novelty, Monroe City, and Columbia. There are two MCC stations in the Columbia area. One station is located at Sanborn Field, on the University of Missouri campus. The other station is located at South Farm, just outside the southeastern edge of Columbia. This shall be referred to as the MCC network. Figure 3.3 shows all the gages used in this study with an emphasis on the ASOS and MCC networks.

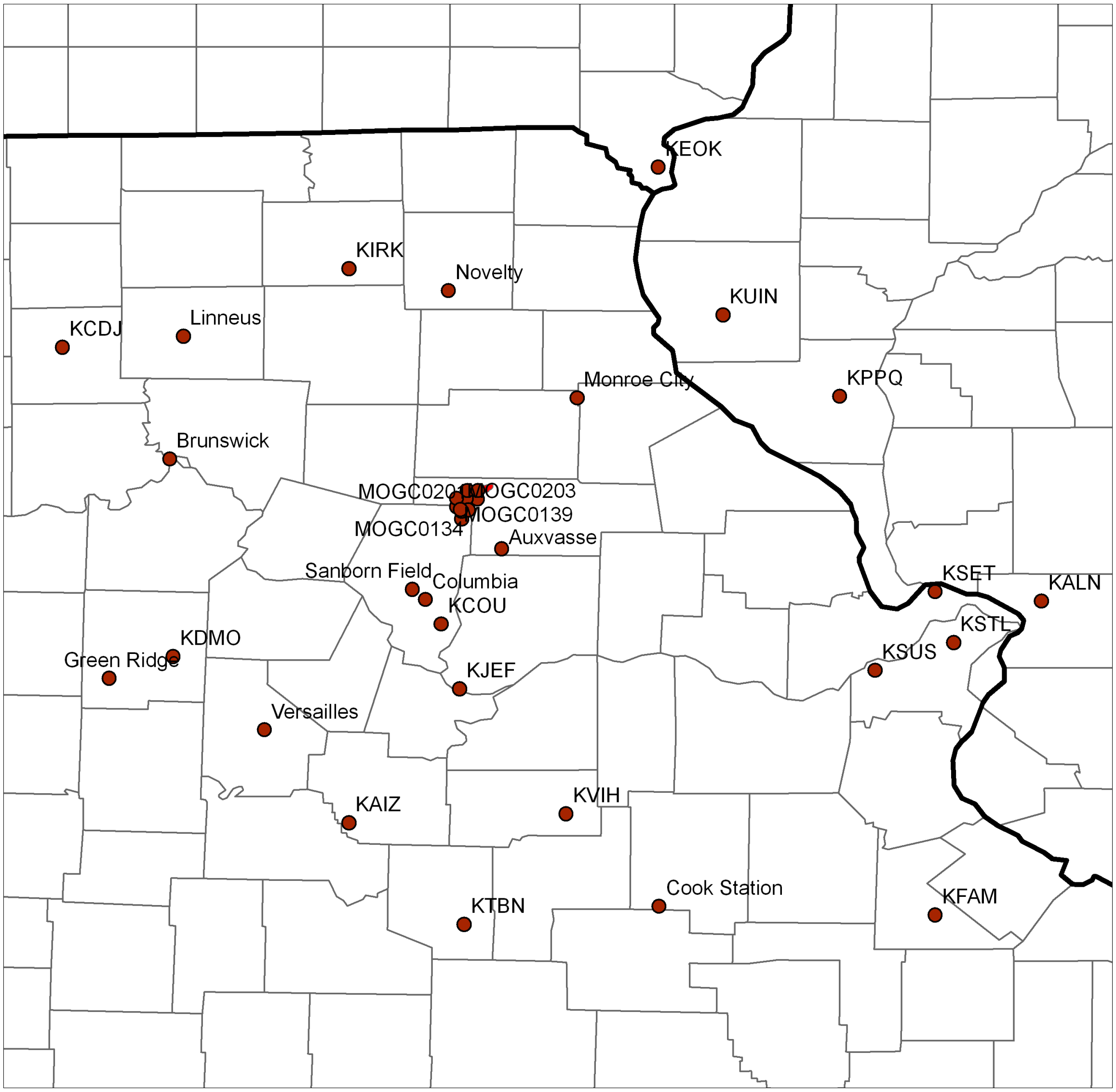

Figure 3.3: The Goodwater Creek catchment is shaded in red with county boundaries in thin lines and state lines in thick lines. All the gages used in this study are shown. However, due to the size of the image, several gages within the catchment that are part of the USDA-ARS network are not labeled.

3.2.3. USDA-ARS Stations

The Cropping Systems and Water Quality Research Unit of the United States Department of Agriculture (USDA) – Agriculture Research Service (ARS) operates ten rain gages within the Goodwater Creek catchment. These gages report data every two minutes. No other meteorological data are recorded at these stations. This network shall be referred to as the USDA-ARS network. Figure 3.4 shows the gages in the USDA-ARS network. The rain gages are Belfort 20-cm weighing rain gages that automatically record data every two minutes (Sadler *et al.*, 2006). Because the gages are weighing gages instead of tipping bucket gages, they are less prone to underestimating rainfall during periods of heavy rainfall.

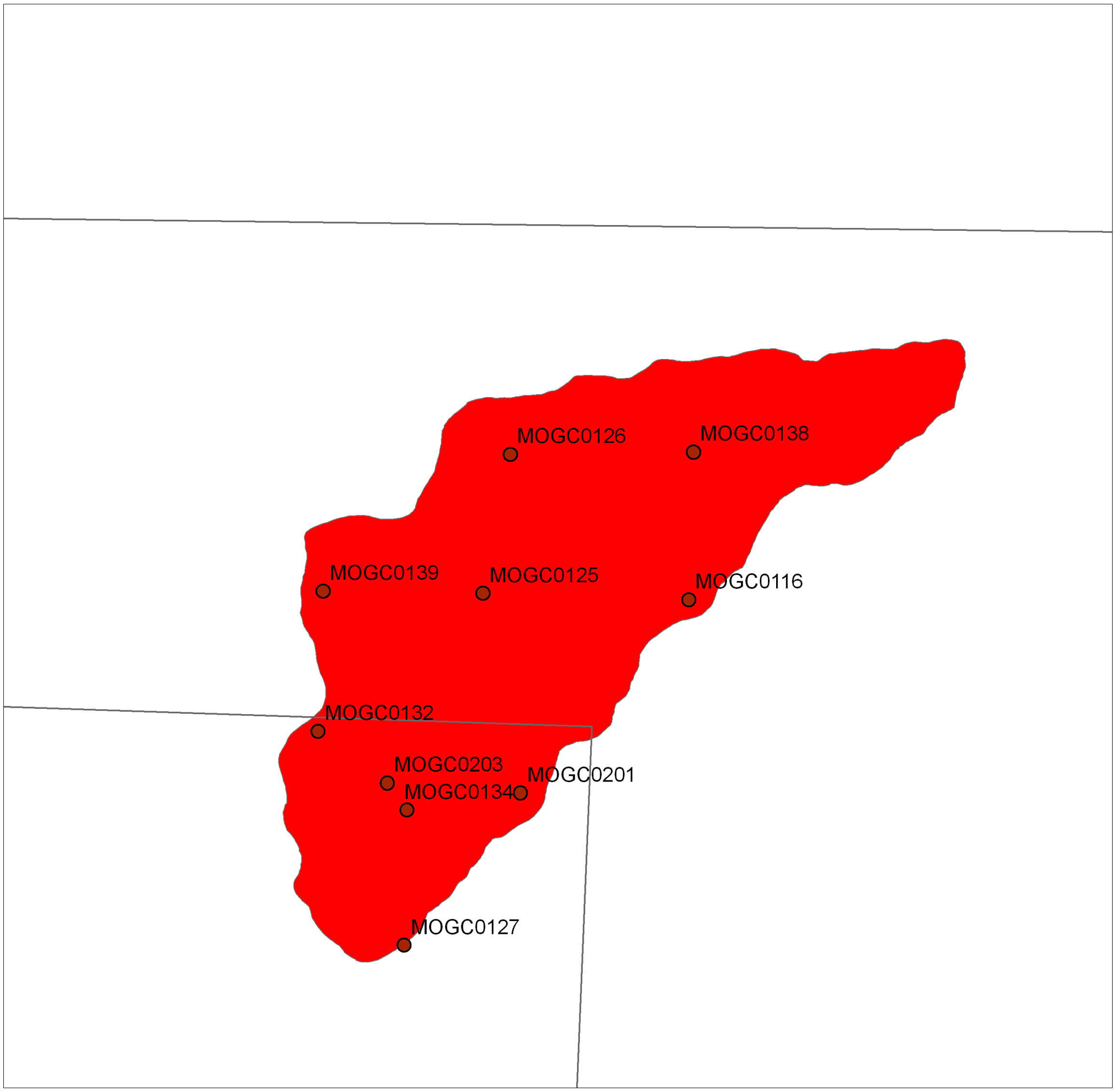

Figure 3.4: The Goodwater Creek catchment is shaded in red with county boundaries in black lines. Gages in the USDA-ARS network are shown.

Actual data from the USDA-ARS network were provided in ten minute intervals for this study. These data were summed over the period of an hour to produce hourly accumulations at each gage. The hourly accumulations from the USDA-ARS network were then used in the intercomparison.

3.3. Radar-Derived Observations

Two data sets, using primarily radar-derived rainfall rates and accumulations, are used in this study. One data set is derived from a national composite of level III radar reflectivity. The other data set is MPE data.

3.3.1. Rainfall Derived from Level III Data

National composites of level III data are available from the Iowa Environmental Mesonet (IEM) at Iowa State University. Data are composited from reflectivity observed by WSR-88D radars, and composites are available every five minutes. The composites are reflectivity data with a precision of 5 dBZ. The composites are provided as images that are easily georeferenced for use in Geospatial Information Systems (GIS) software. Data for each of the cases in this project were at a resolution of 2 km.

A convective Z-R relationship was applied to the data to produce a rainfall rate from reflectivity. Reflectivity was capped at 53 dBZ, which is consistent with the hail cap used in the operational WSR-88D rainfall algorithm. Because composites are available every five minutes, and the Z-R relationship produces rainfall rates in units of mm hr^{-1}, a mean of rainfall rates from 12 consecutive composites was computed to produce an average rainfall rate for the hour, or a rainfall accumulation. Because of the coarse precision of level III data, using data from a single composite would produce unrealistic discontinuities in rainfall rate and accumulation. However, the mean over an hour produces a smoothed and more realistic rainfall field. For the purposes of this paper, data derived in this way shall be referred to as convective radar-derived rainfall data.

3.3.2. MPE Data

MPE data were downloaded and ingested into GIS software. MPE data are available on an hourly basis. Unlike the convective radar-derived rainfall data, these data are clipped to the boundary of a River Forecast Center (RFC). Because the Goodwater Creek Catchment drains into the Mississippi River and is not part of the Missouri River Basin, the appropriate RFC is the North Central RFC (NCRFC). MMOSAIC data from the NCRFC were used in this study. The spatial resolution of these are approximately 4 km.

MPE data is produced from WSR-88D radar products, rain gage observations, and satellite imagery. Radar estimates of rainfall are calibrated using rain gage observations. Satellite estimates of rainfall, which are also calibrated using observations from rain gages, are used to fill in gaps where radar coverage is absent. Rainfall estimates are combined with rain gage output and mosaicked together to produce a composite over the area of a river forecast center. Subjective quality control is performed during the process, particularly in evaluating the performance of rain gage observations.

3.4. Cases

Because some data sets were not available prior to 2004 and some data sets were unavailable after 2004, only cases from 2004 were chosen. Additionally, cases chosen were high-intensity convective rainfall cases ,to simplify the choice of a Z-R relationship and because these cases were of the greatest interest. Eight cases from 2004 were chosen and each is described briefly in this section. Because some data are available only at a temporal resolution of one hour, such as the MPE data, each case includes one hour of a rainfall event. Times given of rainfall events are at the end of the hour, when stations such as ASOS stations are reporting hourly rainfall accumulation. Radar imagery from the middle of each one-hour event can be found in Appendix D.

3.4.1. May 19, 2004 at 07 UTC

At 06 UTC, a complex of thunderstorms was oriented nearly east to west from central Missouri to slightly north of Saint Louis, Missouri. The convection was quasi-linear with embedded convective cells. Small amounts of stratiform precipitation were also evident in the vicinity of the storms. The general motion of the cells in the complex of storms was to the east-southeast. Additional thunderstorms were evident over west central Missouri, although not organized in a quasi-linear fashion nor part of the complex over eastern and central Missouri. Rain gage observations from the USDA-ARS network are shown in table 3.1.

Rain Gage	**Rainfall (mm)**
MOGC0116	26.9
MOGC0125	26.2
MOGC0126	32.8
MOGC0127	5.3
MOGC0132	10.9
MOGC0134	8.4
MOGC0138	23.9
MOGC0139	25.1
MOGC0201	10.9
MOGC0203	9.4

Table 3.1: Rainfall observed at rain gages within the Goodwater Creek catchment for the hour leading up to May 19, 2004 at 07 UTC.

3.4.2. July 6, 2004 at 13 UTC

At 12 UTC, two large complexes of thunderstorms were ongoing with other convective activity occurring as well. One complex became quasi-linear in structure between 12 UTC and 13 UTC, oriented from northwest to southeast, and was slightly northeast of Columbia, Missouri at the beginning of the hour. A second complex was in Illinois, just east of Hannibal, Missouri. A smaller thunderstorm cell was slightly south of Monroe City, Missouri, between the two thunderstorm complexes.

Additional, weaker, thunderstorm activity extended northwest from the westernmost complex of thunderstorms into southwest Iowa. Stratiform precipitation was occurring between the two thunderstorm complexes, in addition to the convective cell near Monroe City. More stratiform precipitation was occurring to the west of the western complex to the south of the weak convection extending into southwest Iowa. The general motion of the thunderstorms was to the east-northeast during the period of interest. Rain gage observations from the USDA-ARS network are shown in table 3.2.

Rain Gage	**Rainfall (mm)**
MOGC0116	22.2
MOGC0125	19.9
MOGC0126	13.8
MOGC0127	34.7
MOGC0132	23.0
MOGC0134	27.4
MOGC0138	19.8
MOGC0139	16.8
MOGC0201	26.9
MOGC0203	27.0

Table 3.2: Rainfall observed at rain gages within the Goodwater Creek catchment for the hour leading up to July 6, 2004 at 13 UTC.

3.4.3. August 4, 2004 at 08 UTC

At 07 UTC, a large complex of thunderstorms was ongoing over much of the northern half of Missouri. A line of thunderstorms over northern central Illinois was oriented from northeast to southwest with a large region of stratiform precipitation observed to the north and west of the line. Although the line was broken through much of west central Illinois, the complex extended into northern Missouri where a line was evident at the beginning of the period from near Monroe City, Missouri to near Boonville, Missouri. Additional thunderstorms were occurring to the north and west of the line and extending as far west as into the Kansas City, Missouri area. The general track of individual cells within the complex was to the east while the complex as a whole propagated to the southeast. Rain gage observations from the USDA-ARS network are shown in table 3.3.

Rain Gage	**Rainfall (mm)**
MOGC0116	27.4
MOGC0125	27.7
MOGC0126	34.3
MOGC0127	29.0
MOGC0132	28.4
MOGC0134	24.4
MOGC0138	31.0
MOGC0139	29.7
MOGC0201	24.9
MOGC0203	25.9

Table 3.3: Rainfall observed at rain gages within the Goodwater Creek catchment for the hour leading up to August 4, 2004 at 08 UTC.

3.4.4. August 4, 2004 at 09 UTC

As a continuation from the previous hour, a large complex of thunderstorms over Missouri and Illinois continued to move to the southeast. Many of the thunderstorms over far northern Missouri weakened by the start of this period. The leading edge of thunderstorm activity across Missouri was generally to the south of the catchment and oriented east to west near Columbia, Missouri. Much of the precipitation over the catchment during the time period appeared to be stratiform in nature. During this period, the thunderstorms over Missouri appeared to continue to weaken. Supporting the qualitative observations of stratiform precipitation over the catchment and a general weakening of the storms during this period are lower rainfall totals in the catchment during this period as compared to the previous period. Rain gage observations from the USDA-ARS network are shown in table 3.4.

Rain Gage	**Rainfall (mm)**
MOGC0116	22.0
MOGC0125	16.7
MOGC0126	14.4
MOGC0127	21.5
MOGC0132	23.1
MOGC0134	26.9
MOGC0138	15.1
MOGC0139	17.1
MOGC0201	30.3
MOGC0203	25.8

Table 3.4: Rainfall observed at rain gages within the Goodwater Creek catchment for the hour leading up to August 4, 2004 at 09 UTC.

3.4.5. August 26, 2004 at 06 UTC

Thunderstorm activity in Missouri during this time period was very isolated in nature. Greater areal coverage of thunderstorms was evident in west central and southwest Illinois with a line of thunderstorms extending from northwest to southeast just east of the Mississippi River. Thunderstorms developed and increased in areal coverage over southeast Iowa and northwest Illinois during the time period. Isolated thunderstorm activity in extreme northeast Missouri also weakened during the time period. Precipitation in the catchment of interest was due to a complex of thunderstorms that extended from near Fayette, Missouri to near Perry, Missouri. The general motion of the thunderstorm complex over central Missouri was to the east-northeast. Rain gage observations from the USDA-ARS network are shown in table 3.5.

Rain Gage	**Rainfall (mm)**
MOGC0116	65.5
MOGC0125	71.6
MOGC0126	67.1
MOGC0127	25.9
MOGC0132	57.7
MOGC0134	36.8
MOGC0138	73.2
MOGC0139	60.7
MOGC0201	38.5
MOGC0203	44.7

Table 3.5: Rainfall observed at rain gages within the Goodwater Creek catchment for the hour leading up to August 26, 2004 at 06 UTC.

3.4.6. August 26, 2004 at 07 UTC

This was a continuation of the previous hour in which the complex of thunderstorms over the catchment at the beginning of the period tracked generally to the east and exhibited a weakening trend. Additional, very isolated, thunderstorms began to develop to the north and west during the time period over portions of north central Missouri. The weakening trend of the thunderstorms and their movement away from the catchment was supported by lower rainfall totals observed in the catchment during this hour than in the previous hour. Rain gage observations from the USDA-ARS network are shown in table 3.6.

Rain Gage	**Rainfall (mm)**
MOGC0116	12.0
MOGC0125	6.9
MOGC0126	5.6
MOGC0127	19.1
MOGC0132	7.7
MOGC0134	19.6
MOGC0138	5.1
MOGC0139	4.1
MOGC0201	20.7
MOGC0203	14.3

Table 3.6: Rainfall observed at rain gages within the Goodwater Creek catchment for the hour leading up to August 26, 2004 at 07 UTC.

3.4.7. August 27, 2004 at 18 UTC

At the start of the period, an east to west oriented line of showers and thunderstorms was present from near Novelty, Missouri through central Illinois. This complex exhibited a weakening trend during the period of interest. Thunderstorms were developing over portions of central Missouri with a cluster of cells positioned from near Harrisburg, Missouri to near Vandalia, Missouri. Additional thunderstorms were developing and moving northeast through parts of Moniteau and Cooper counties in central Missouri during the time period. The cluster from Harrisburg to Vandalia weakened during the period and tracked to the northeast. Rain gage observations from the USDA-ARS network are shown in table 3.7.

Rain Gage	**Rainfall (mm)**
MOGC0116	18.9
MOGC0125	23.9
MOGC0126	23.4
MOGC0127	1.3
MOGC0132	14.9
MOGC0134	6.5
MOGC0138	23.1
MOGC0139	29.5
MOGC0201	3.3
MOGC0203	9.9

Table 3.7: Rainfall observed at rain gages within the Goodwater Creek catchment for the hour leading up to August 27, 2004 at 18 UTC.

3.4.8. October 18, 2004 at 10 UTC

At the beginning of the event, a quasi-linear cluster of thunderstorms extended from central Missouri through central Illinois and into southern Indiana. A broad area of stratiform precipitation was occurring north of the line of storms. During the event, storms were weakening over central Missouri while some of the storms were intensifying over eastern Missouri and southern Illinois. At the start of the event, precipitation was already ongoing over the catchment. Throughout the event, storms moved out of the area. Rain gage observations from the USDA-ARS network are shown in table 3.8.

Rain Gage	**Rainfall (mm)**
MOGC0116	10.3
MOGC0125	8.1
MOGC0126	5.1
MOGC0127	19.9
MOGC0132	12.0
MOGC0134	15.1
MOGC0138	5.8
MOGC0139	6.3
MOGC0201	18.2
MOGC0203	11.8

Table 3.8: Rainfall observed at rain gages within the Goodwater Creek catchment for the hour leading up to October 18, 2004 at 10 UTC.

3.5. Procedure

The initial work focused on an intercomparison between four data sets, which are the combination of the ASOS and MCC networks, the combination of the ASOS, MCC, and USDA-ARS networks, the convective radar-derived rainfall data, and the MPE data. Later work focused on adjusting the output of the convective radar-derived rainfall data and the MPE data to match rain gage observations.

Processing of spatial data was done using the ArcInfo GIS software. Some calculations of data were done using Microsoft Excel. Additional software, provided by the National Oceanic and Atmospheric Administration (NOAA), for decoding the native format on which MPE data are delivered to produce text files with the data.

3.5.1. Ingesting Data

Rain gage data was available from three networks, all of which reported at least as frequently as on an hourly basis. Rainfall accumulations from networks that reported more frequently, such as the MCC network and the USDA-ARS network were summed over the period of an hour to produce an hourly accumulation. The data from the MCC network was already summed when it was acquired from the archive. However, the USDA-ARS network data was summed to create hourly rainfall accumulations as part of this procedure. This work was done in Microsoft Excel and spreadsheets were produced as output, which were then imported into ArcInfo by using ArcCatalog. Additional processing was performed to create shapefiles from the data that was imported from Excel.

National composites of reflectivity were available from the IEM and were downloaded. Composites were available every five minutes and so 12 composites were downloaded to cover events that were one hour long. These composites were georeferenced using ArcCatalog for use in ArcInfo. In the composites, data was not in units of dBZ but was instead 8-bit numbers assigned to colors that were frequently used for reflectivity color scales in radar imagery. A conversion was performed to convert from the raw numbers used in the file format to units of dBZ. An additional conversion was performed to produce reflectivity (Z) instead of decibels of reflectivity (dBZ). Following these conversions, a convective Z-R relationship was applied to calculate instantaneous rainfall rates. A flowchart of this process, generated in the ArcInfo Model Builder, is shown in figure 3.5. Figure 3.6 references figure 3.5 and includes the step of georeferencing the data. Using the cell statistics tool, the 12 instantaneous rainfall rates were averaged to produce an hourly accumulation of rainfall. This processing uses the output of the process shown in figure 3.6.

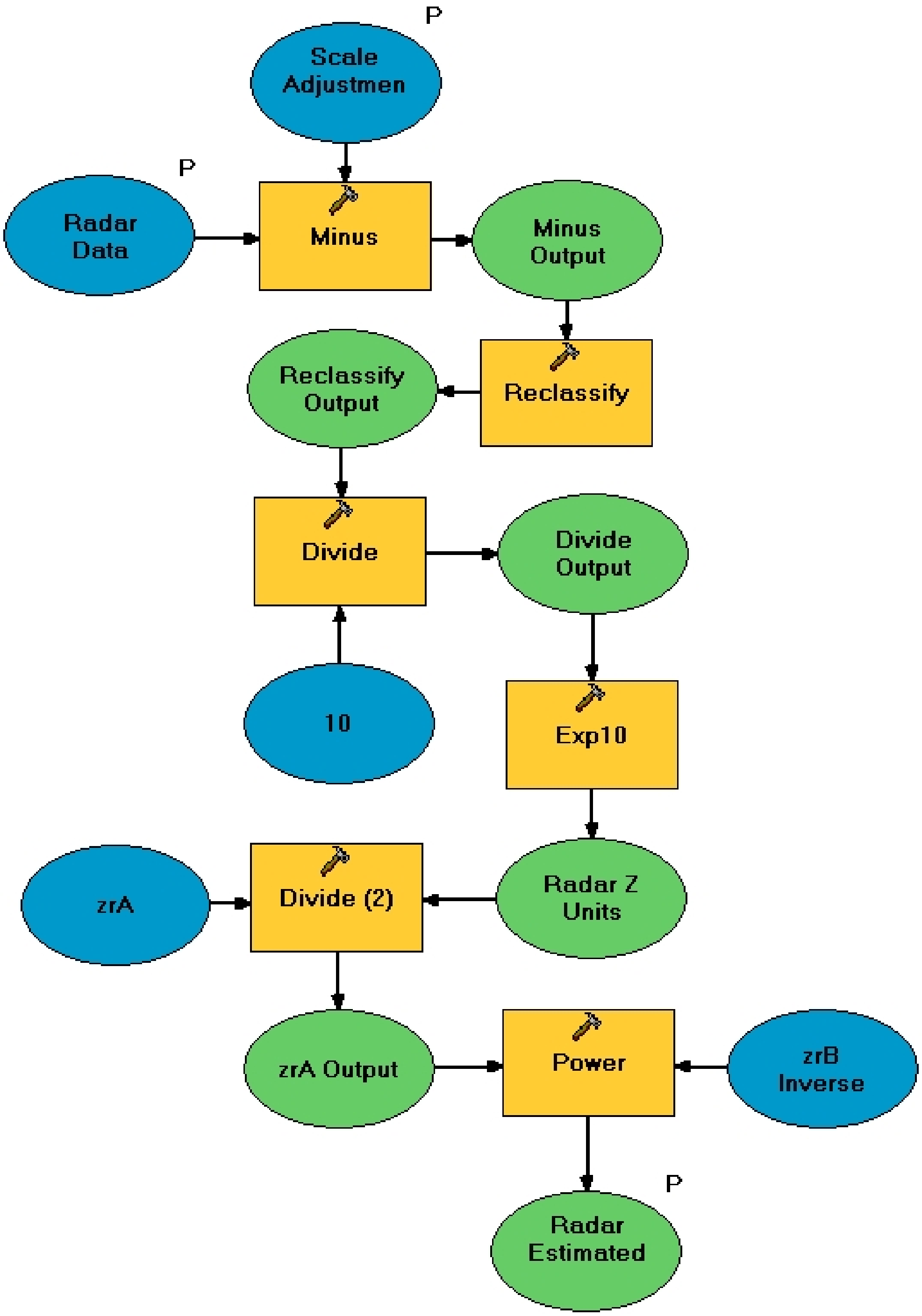

Figure 3.5: A flowchart of the process for ingesting a single radar composite to produce a rainfall rate from reflectivity.

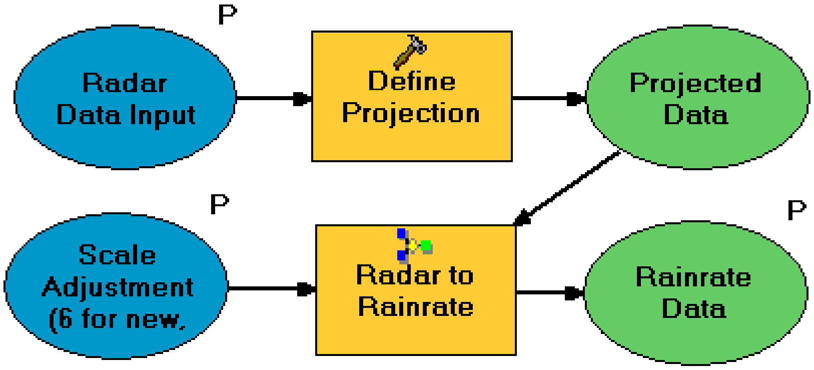

Figure 3.6: A flowchart for the process of ingesting a single radar composite, including the step of georeferencing the data.

MPE data were downloaded from NOAA and was available in the XMRG format. This format is not readily ingested by ArcGIS and therefore some conversions needed to be performed prior to ingesting and manipulating the data. Data was converted from the XMRG format to a plain text format using the xmrgtoasc tool available from NOAA. Then using the ASCII to GRID tool in ArcInfo, the text data was ingested into a raster GRID file.

3.5.2. Interpolation of Data

The data used in this intercomparison were very heterogeneous. Rain gage observations are observations at a single point whereas radar data consist of observations from many points. The rain gage data were best represented in a vector format in GIS whereas the radar data were best represented in a raster format. However, for some of the intercomparisons, a common format was needed. Some of the tools needed for the comparisons, such as the flow accumulation tool, operate only on raster data. Therefore it was useful to convert all the data sets to raster data.

Although many methods exist for interpolating point data to produce gridded data, kriging was chosen for this study. Kriging weights observations based on their distance from the grid point and on the distance between observations. A simpler interpolation scheme may assimilate redundant information if many observations are closely spaced together in an area while other areas have relatively sparse observations. Kriging not only produces gridded estimates of data but also measures of the accuracy of the interpolation. Although grids created by kriging may not match actual observations, the range of interpolated values is not constrained to the range of observed values. An extended discussion of other methods for generating grids from point observations can be found in Appendix C.

Point data were interpolated to a grid spacing of 100m. Additionally, the radar-based raster data sets were upsampled to a grid spacing of 100m using the resample tool in ArcInfo. This was done for the purpose of creating a high-resolution grid with a consistent resolution for each dataset. The high-resolution grids were then clipped to the boundaries of the catchment. The process of interpolating the rain gage observations is shown in figure 3.7. Figures 3.8 and 3.9 show the processes for upsampling and clipping convective radar-derived rainfall and MPE data, respectively.

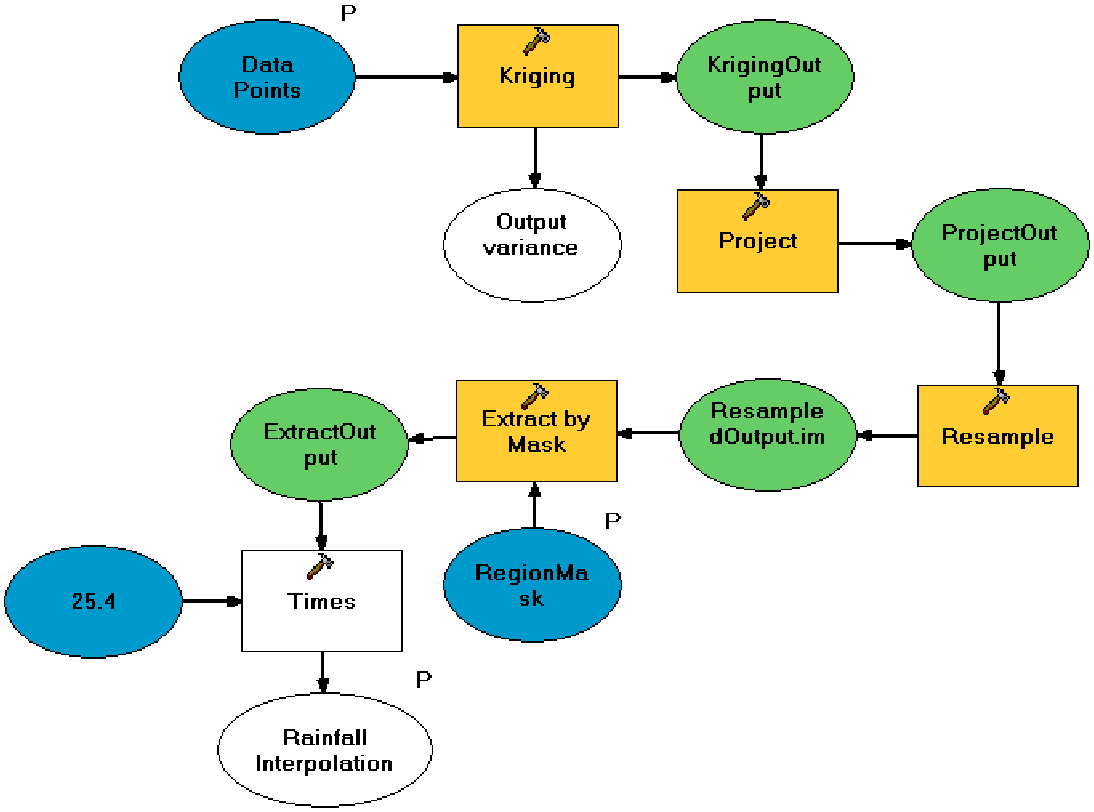

Figure 3.7: This figure shows the process of interpolating rain gage observations and clipping to the boundaries of the catchment. The input is in inches and the output is in millimeters.

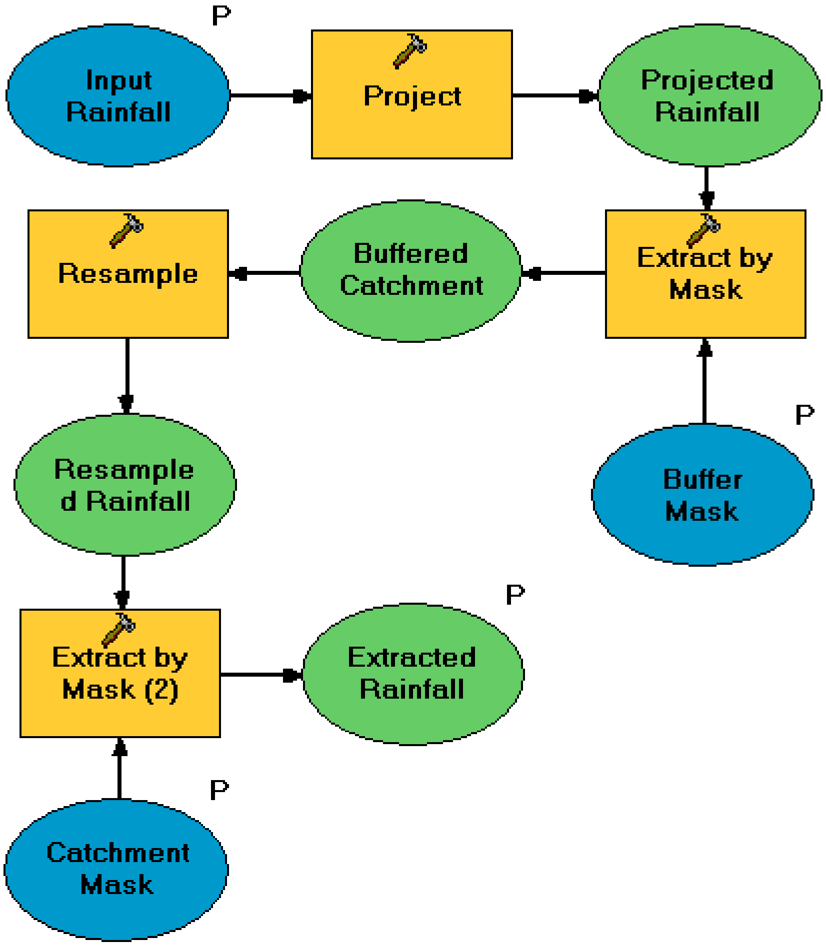

Figure 3.8: This figure shows a flowchart for upsampling and clipping convective radar-derived rainfall data.

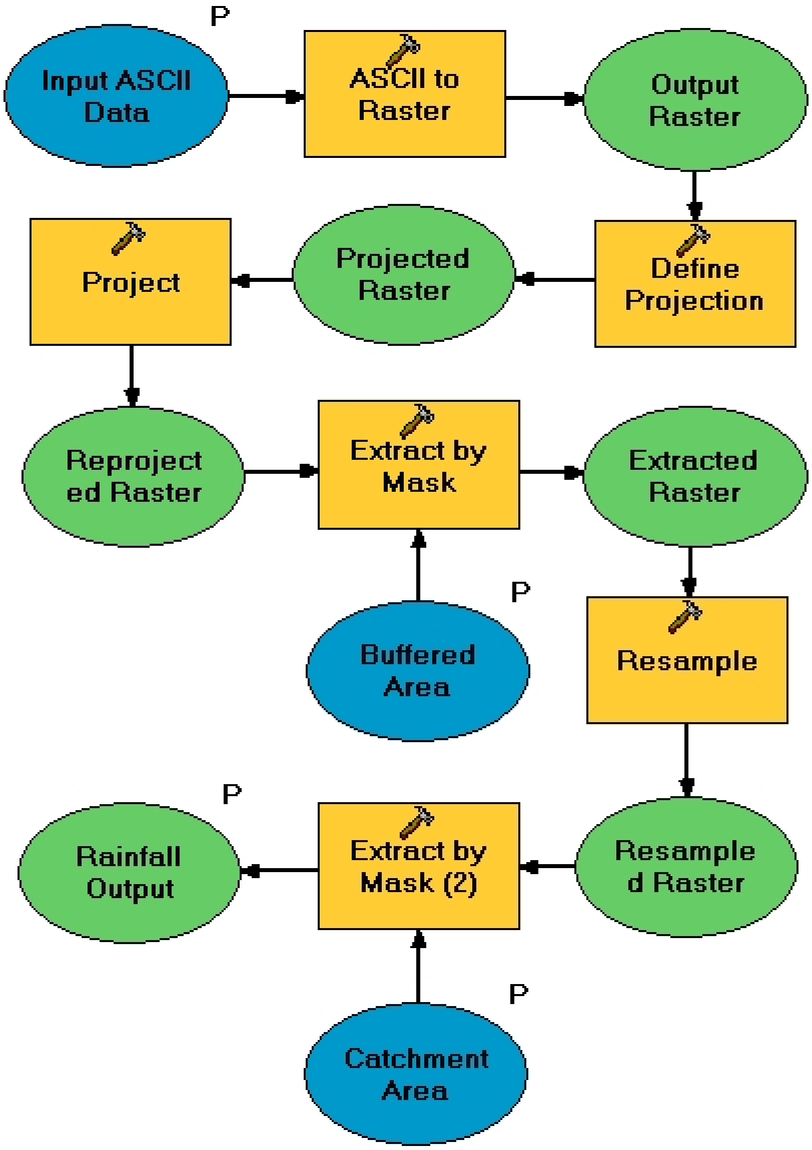

Figure 3.9: This figure shows the process of importing MPE data from a text file, upsampling it, and clipping it to the catchment boundaries. Part of this process is also described in Section 3.5.1.

3.5.3. Methods of Intercomparing Observations

Many methods exist for intercomparing observations from rain gages and radar-derived rainfall estimates. A few parameters were compared in this study and will be described here. One simple method of comparing rain gage and radar-derived projects is to merely compare the radar-derived estimate of rainfall at the point were a gage is located. This was one method used in this intercomparison. However, it was also useful to examine the maximum and minimum rainfall accumulation reported in the catchment, particularly because it is possible for maxima and minima to be located between gages where radar may still detect them. Additionally the flow accumulation tool available in ArcInfo was used. The flow accumulation at the outlet of the catchment is the total amount of rainfall that fell throughout the catchment. For the remainder of this project, the total amount of rainfall in the catchment shall be referred to as catchment total rainfall. These three methods of comparing different rainfall observations were used in evaluating the output of different data sets.

3.5.4. Intercomparison of Data Sets

Four raster data sets were created during the course of this part of the study. One was created using data from the ASOS and MCC networks. Another data set was created using data from the ASOS, MCC, and USDA-ARS networks. A third data set consisted of convective radar-derived rainfall. The fourth data set was MPE data.

Rain gage observations from the USDA-ARS network were compared against the point rainfall estimate in each raster data set. Additionally, the maximum and minimum rainfall in each raster data set was found and compared against the maximum and minimum rainfall observed by the USDA-ARS network. Additionally, the flow accumulation tool was used to calculate the total amount of rain over the entire catchment in each raster. Comparisons were done for each of the eight cases and then aggregate results were calculated as well.

3.5.5. Calibrating Radar-Derived Products

Because the work described in section 3.5.4 showed that both the convective radar-derived rainfall estimate and the MPE both underestimated rainfall over the catchment, additional work was done to attempt to calibrate the rainfall estimates. Additionally, the data set using only data from the ASOS and MCC networks was found to be unsuitable for this study and was not used beyond the work done in section 3.5.4. The question that was examined in this portion of the study was whether radar-derived products could be calibrated using only a single gage in the catchment to produce reasonable results or if the entire USDA-ARS rain gage network is needed to accurately represent the spatial characteristics of rainfall in the catchment.

A single gage, MOGC0125, was selected for calculating the bias of the radar-derived estimates and a correction factor. The gage is centrally located within the catchment, which is why it was chosen for the determining a bias and correction factor for the entire catchment. The bias was the rainfall estimated at the gage location divided by the observed rainfall at the gage. The correction factor was the observed rainfall at the gage divided by the radar-derived estimate of rainfall at the gage location. The radar-derived estimate of rainfall was multiplied by the correction factor over the entire catchment. Therefore, the entire raster was adjusted based on the correction factor determined at MOGC0125. Calibration was done for both the convective radar-derived rainfall data and the MPE data.

3.5.6. Intercomparing Calibrated Radar-Derived Products

The computations described in section 3.5.4 were done for the calibrated radar-derived rainfall products using the calibrated convective radar-derived rainfall data and the calibrated MPE data. As with the earlier data sets, both calibrated radar-derived data sets were compared against the observed rainfall in the USDA-ARS rain gage network.

Chapter 4

Results of Intercomparison

This chapter presents and analyzes results of the intercomparison as described in Chapter 3. As stated in the previous chapter, there are two sections to the intercomparison. Therefore, there will be two sections to this chapter. The first section will focus on analyzing results of the intercomparison between interpolating data from the ASOS and MCC networks, interpolating data from the ASOS, MCC, and USDA-ARS networks, convective radar-derived rainfall estimates, and MPE data. The second section will focus on the results of calibrating convective radar-derived rainfall estimates and calibrating MPE data.

4.1. Intercomparison of Unadjusted Data

The results from intercomparing the unadjusted rainfall data will be presented in this section. Although rain gage errors do occur, observations from gages were treated as ground truth. The differences of the interpolated rainfall products and radar-derived rainfall products are calculated against the ground truth.

Each rain gage was matched up against a grid point in each of four spatial representations of the rainfall during an event. A percent difference was calculated for each of the spatial representations by dividing the rainfall in the spatial representation at the grid point by the observed rainfall at the gage. A ratio over one indicates that the spatial representation is overestimating the rainfall. Conversely, a result under one indicates that the spatial representation is underestimating the rainfall. The mean ratio for the interpolations of gage products against all of the gages in an event is shown in Table 4.1. Table 4.2 shows the mean ratio of radar-derived products against all of the gages in an event.

Event	**ASOS/MCC/USDA-ARS Interp. Difference**	**ASOS/MCC Interp. Difference**
May 19, 2004 at 07 UTC	1.05	0.32
July 6, 2004 at 13 UTC	1.00	0.05
August 4, 2004 at 08 UTC	1.01	0.21
August 4, 2004 at 09 UTC	1.00	0.35
August 26, 2004 at 06 UTC	1.00	0.00
August 26, 2004 at 07 UTC	1.28	0.03
August 27, 2004 at 18 UTC	1.54	0.19
October 18, 2004 at 10 UTC	1.17	0.15

Table 4.1: The ratio of rainfall estimates from interpolating gages from various networks to actual gage observations is shown.

Event	Convective Radar-Derived Rainfall Bias	MPE Bias
May 19, 2004 at 07 UTC	0.46	0.46
July 6, 2004 at 13 UTC	0.83	0.61
August 4, 2004 at 08 UTC	1.05	0.71
August 4, 2004 at 09 UTC	0.62	0.53
August 26, 2004 at 06 UTC	0.82	0.64
August 26, 2004 at 07 UTC	1.25	1.79
August 27, 2004 at 18 UTC	0.93	0.36
October 18, 2004 at 10 UTC	0.83	1.19

Table 4.2: The ratio of radar-derived rainfall estimates to actual gage observations is shown.

It is notable that there is a high degree of variability from case to case in the ratio of the estimated rainfall to observed rainfall for most of the interpolations. Although one would expect the interpolation from the USDA-ARS, MCC, and ASOS networks to perform the best and nearly match the actual observations, this is not always the case. It is also clear that merely interpolating the MCC and ASOS networks greatly underestimates the rainfall in each case. Although not shown, there were many cases in which interpolating observations from the MCC and ASOS networks did not result in any variability in the interpolated rainfall across the catchment. However, as shown when describing the cases in Section 3.4, there is almost always strong variability in rainfall across the catchment. For these reasons, it is already apparent that merely interpolating the MCC and ASOS networks is unsuitable for estimating rainfall in the catchment. Not only is the rainfall underestimated, but the spatial variability of rainfall in the catchment is not represented.

Although both the MPE and the convective radar-derived rainfall underestimated rainfall in a majority of the cases, there is some difference between the two that is evident. The MPE underestimated rainfall by a greater amount than the convective radar-derived rainfall did in most cases. Additionally, there is a greater degree of variability in the bias of the MPE as compared with the convective radar-derived rainfall.

Event	**Conv. Radar-Derived Rainfall Ratio Range**	**MPE Ratio Range**
May 19, 2004 at 07 UTC	0.49	0.59
July 6, 2004 at 13 UTC	0.62	0.43
August 4, 2004 at 08 UTC	0.65	0.4
August 4, 2004 at 09 UTC	1.13	0.46
August 26, 2004 at 06 UTC	0.49	0.62
August 26, 2004 at 07 UTC	1.92	1.99
August 27, 2004 at 18 UTC	1.24	0.62
October 18, 2004 at 10 UTC	0.7	0.92

Table 4.3: The range of ratios of radar-derived rainfall estimates to actual gage observations is shown.

Table 4.3 shows the range in biases of radar-derived rainfall estimates against actual gage observations. The convective radar-derived rainfall biases had a greater mean range than did the MPE biases over these eight cases. However, in four cases, the MPE bias range was actually larger than the convective radar-derived rainfall. It is clear, however, that there is a strong variability in the performance of radar-derived products from event to event. Some of the thunderstorms actually spanned more than one event. By comparing the two events resulting from a single thunderstorm, it is clear that the performance of radar-derived products may change greatly during the duration of a single thunderstorm.

The statistics presented above were aggregate statistics for a single event. However, comparing radar-derived rainfall estimates against individual gage observations also yields some notable results. For example, the mean ratio of estimated rainfall using the convective radar-derived rainfall estimate to gage-observed rainfall for all events was 0.85, compared to 0.79 for the ratio of MPE estimated rainfall to gage observations. However, the median ratio was 0.83 for the convective radar-derived rainfall estimate and 0.65 for the MPE. This suggests that for most gages, the convective radar-derived rainfall estimate more closely matches the gage observations. The mean of the MPE ratio is being skewed upward, likely due to some outliers. This is also indicated by the standard deviation of the convective radar-derived ratios of 0.37 and the standard deviation of the MPE ratios of 0.53. The stretching of the distribution is evident at both ends. The maximum ratio of the convective radar-derived rainfall estimate is 2.47 and the minimum is 0.22. However, for the MPE, the maximum ratio is 3.18 and the minimum is 0.07.

Percentile	**10**	**20**	**30**	**40**	**50**	**60**	**70**	**80**	**90**
Convective Radar-Derived Rainfall Ratio	0.44	0.56	0.66	0.74	0.83	0.90	1.00	1.14	1.23
MPE Ratio	0.33	0.42	0.53	0.57	0.65	0.71	0.84	0.98	1.43

Table 4.4: The distribution of the ratios of radar-derived rainfall estimates to gage observations is shown in this table.

Similar trends are also represented by further examining the distribution of ratios. The median of the convective radar-derived rainfall ratio is at the 70th percentile whereas the median of the MPE ratio is approximately at the 80th percentile. The MPE underestimated rainfall to a greater extent than the convective radar-derived rainfall in most cases. However, the distribution clearly indicates the presence of outliers in the distribution of the MPE ratios above the 80th percentile. This confirms the previous analysis that the distribution of the ratios of MPE estimates is stretched to a greater extent than the distribution of ratios of convective radar-derived rainfall estimates.

Event	**Gage Min. (mm)**	**Gage Max. (mm)**	**Conv. Radar-Derived Rainfall Min. (mm)**	**Conv. Radar-Derived Rainfall Max. (mm)**
May 19, 2004 at 07 UTC	5.3	32.8	2.4	18.3
July 6, 2004 at 13 UTC	13.8	34.7	13.3	24.5
August 4, 2004 at 08 UTC	24.4	34.3	16.5	37.0
August 4, 2004 at 09 UTC	14.4	30.3	5.7	23.9
August 26, 2004 at 06 UTC	26.0	73.2	29.4	59.1
August 26, 2004 at 07 UTC	4.1	20.7	1.5	32.7
August 27, 2004 at 18 UTC	1.3	29.5	1.1	28.5
October 18, 2004 at 10 UTC	5.1	19.9	3.4	24.5

Table 4.5: The minimum and maximum rainfall totals observed at gages in the catchment are shown compared with the minimum and maximum rainfall totals estimated in the catchment by the convective radar-derived rainfall.

Event	**Gage Min. (mm)**	**Gage Max. (mm)**	**MPE Min. (mm)**	**MPE Max. (mm)**
May 19, 2004 at 07 UTC	5.3	32.8	3.8	13.4
July 6, 2004 at 13 UTC	13.8	34.7	10.1	14.5
August 4, 2004 at 08 UTC	24.4	34.3	14.5	26.1
August 4, 2004 at 09 UTC	14.4	30.3	9.2	13.8
August 26, 2004 at 06 UTC	26.0	73.2	17.6	53.1
August 26, 2004 at 07 UTC	4.1	20.7	2.4	39.5
August 27, 2004 at 18 UTC	1.3	29.5	0.7	16.3
October 18, 2004 at 10 UTC	5.1	19.9	3.2	16.9

Table 4.6: The minimum and maximum rainfall totals observed at gages in the catchment are shown compared with the minimum and maximum rainfall totals estimated in the catchment by the MPE.

Event	Gage Min. (mm)	Gage Max. (mm)	ASOS/MCC/USDA-ARS Min. (mm)	ASOS/MCC/USDA-ARS Max. (mm)
May 19, 2004 at 07 UTC	5.3	32.8	8.9	27.1
July 6, 2004 at 13 UTC	13.8	34.7	13.8	34.5
August 4, 2004 at 08 UTC	24.4	34.3	24.4	34.3
August 4, 2004 at 09 UTC	14.4	30.3	14.1	30.1
August 26, 2004 at 06 UTC	26.0	73.2	26.1	73.1
August 26, 2004 at 07 UTC	4.1	20.7	5.9	17.6
August 27, 2004 at 18 UTC	1.3	29.5	7.1	23.8
October 18, 2004 at 10 UTC	5.1	19.9	7.1	15.5

Table 4.7: The minimum and maximum rainfall totals observed at gages in the catchment are shown compared with the minimum and maximum rainfall totals estimated in the catchment by the interpolation of data from the ASOS, MCC, and USDA-ARS networks.

Event	**Gage Min. (mm)**	**Gage Max. (mm)**	**ASOS/MCC Min. (mm)**	**ASOS/MCC Max. (mm)**
May 19, 2004 at 07 UTC	5.3	32.8	4.0	4.0
July 6, 2004 at 13 UTC	13.8	34.7	0.2	1.8
August 4, 2004 at 08 UTC	24.4	34.3	5.5	6.4
August 4, 2004 at 09 UTC	14.4	30.3	6.4	7.4
August 26, 2004 at 06 UTC	26.0	73.2	0.1	0.1
August 26, 2004 at 07 UTC	4.1	20.7	0.2	0.2
August 27, 2004 at 18 UTC	1.3	29.5	1.2	1.2
October 18, 2004 at 10 UTC	5.1	19.9	0.5	1.9

Table 4.8: The minimum and maximum rainfall totals observed at gages in the catchment are shown compared with the minimum and maximum rainfall totals estimated in the catchment by the interpolation of data from the ASOS and MCC networks.

Shown in Tables 4.5 to 4.8 are the minimum and maximum rainfall totals estimated by each spatial product as compared against those observed by gages in the catchment. It is clear that merely using the ASOS and MCC networks to interpolate rainfall within the catchment is unsuitable and the rainfall is greatly underestimated. As with previous results, both the MPE and the convective radar-derived rainfall products appear to underestimate the rainfall in the catchment. The best performance was achieved by interpolating the ASOS, MCC, and USDA-ARS networks. The average ratio between estimated rainfall in the interpolation and actual gage observations of the maximum rainfall for this interpolation is 91% and is 176% for the minimum rainfall. However, this is greatly exaggerated due to the August 27, 2004 at 18 UTC case in which the minimum rainfall was overestimated by a factor of five in the catchment. It is also noted that in this interpolation, the maximum rainfall in the catchment is frequently slightly underestimated and the minimum rainfall in the catchment is frequently overestimated slightly. This is likely due to smoothing in the interpolation, but is not believed to introduce a bias in determining the volume of water over the entirety of the catchment.

Case	**MPE Vol.**	**Conv. Radar-derived Vol.**	**ASOS/MCC Vol.**	**ASOS/MCC/USDA-ARS Vol.**
May 19, 2004 at 07 UTC	56174.3	60859.9	30167.3	151761
July 6, 2004 at 13 UTC	100167	134374	9357.51	161696
August 4, 2004 at 08 UTC	158758	213879	44441.9	218221
August 4, 2004 at 09 UTC	83724.3	97446.9	52848.8	146941
August 26, 2004 at 06 UTC	278723	339608	381.86	455055
August 26, 2004 at 07 UTC	114860	88813.5	1527.45	80934.9
August 27, 2004 at 18 UTC	62128.9	122232	8782.87	127190
October 18, 2004 at 10 UTC	73867.2	61855.1	10960.5	78513.3

Table 4.9: Shown is the volume of water accumulated in the catchment in units of cubic meters during the duration of the event estimated from the four different data sets.

Table 4.9 shows the total volume of water accumulated in the catchment during the duration of the event as estimated by each interpolation. Because the best interpolation was deemed to be the interpolation using gage observations from the ASOS, MCC, and USDA-ARS gage networks, this was treated as equivalent to ground truth and biases were calculated against it. In nearly every case, however, both radar-derived rainfall products underestimated the volume of rainfall accumulated in the catchment. However, the worst performance was clearly from the interpolation of the ASOS and MCC networks, which greatly underestimated the volume of rainfall accumulated in each case.

4.2. Intercomparison of Adjusted Data

Interpolating rainfall using the ASOS and MCC networks was clearly unsuitable for estimating either the amount or the spatial structure of rainfall within the catchment. Both of the radar-derived products tended to underestimate rainfall in the catchment as well. However, this was to a much lesser degree than occurred merely by using gages outside the catchment to interpolate rainfall. However, additional work was done to determine if calibrating the radar-derived rainfall products using one gage in the catchment would produce better results. A gage located centrally within the catchment, MOGC0125, was chosen for calculating the bias used in the adjustment.

Event	Adj. Conv. Radar-Derived Rainfall Ratio	Adj. MPE Ratio
May 19, 2004 at 07 UTC	1.67	1.65
July 6, 2004 at 13 UTC	1.25	0.93
August 4, 2004 at 08 UTC	0.81	0.77
August 4, 2004 at 09 UTC	1.02	0.89
August 26, 2004 at 06 UTC	0.99	1.15
August 26, 2004 at 07 UTC	1.02	0.94
August 27, 2004 at 18 UTC	0.89	1.03
October 18, 2004 at 10 UTC	1.06	0.90

Table 4.10: The ratio of adjusted radar-derived rainfall estimates to actual gage observations is shown.

Table 4.10 shows the mean bias for each event of the MPE and convective radar-derived rainfall products following the adjustments. If the May 19, 2004 at 07 UTC case is treated as an outlier in this data set and the other seven cases are examined, the mean and median bias are close to 1. Even including the case that appears to be an outlier, the mean ratio of the adjusted convective radar-derived rainfall to gage observations is 1.09 and the mean ratio of the adjusted MPE is 1.03. The median ratio of the adjusted convective radar-derived rainfall is 1.00 and the median ratio of the adjusted MPE is 0.98. This suggests that the distribution is, indeed, skewed toward a higher ratio, because of an outlier.

Event	Adj. Conv. Radar-Derived Rainfall Ratio Range	Adj. MPE Ratio Range
May 19, 2004 at 07 UTC	1.75	2.13
July 6, 2004 at 13 UTC	0.92	0.65
August 4, 2004 at 08 UTC	0.50	0.43
August 4, 2004 at 09 UTC	1.86	0.78
August 26, 2004 at 06 UTC	0.60	1.10
August 26, 2004 at 07 UTC	1.57	1.04
August 27, 2004 at 18 UTC	1.18	1.80
October 18, 2004 at 10 UTC	0.93	0.70

Table 4.11: The range of ratios of estimated rainfall to gage-observed rainfall for each event for the adjusted radar-derived products is shown.

The range of the ratios for the adjusted radar-derived products for each event is shown in table 4.11. Because, for most cases, the bias adjustment increased the rainfall estimate throughout the catchment by multiplying by a bias correction factor greater than 1, the range of ratios actually increased. This is demonstrated in Table 4.12, which shows the bias correction factors by which the radar-estimates are multiplied for each case.

Event	Conv. Radar-Derived Rainfall Bias Correction Factor	MPE Bias Correction Factor
May 19, 2004 at 07 UTC	3.58	3.60
July 6, 2004 at 13 UTC	1.49	1.53
August 4, 2004 at 08 UTC	0.77	1.08
August 4, 2004 at 09 UTC	1.65	1.69
August 26, 2004 at 06 UTC	1.21	1.80
August 26, 2004 at 07 UTC	0.82	0.53
August 27, 2004 at 18 UTC	0.95	2.88
October 18, 2004 at 10 UTC	1.33	0.76

Table 4.12: Bias correction factors for each of the events are shown.

Percentile	**10**	**20**	**30**	**40**	**50**	**60**	**70**	**80**	**90**
Adjusted Convective Radar-Derived Rainfall Ratio	0.66	0.75	0.86	0.94	1.00	1.01	1.15	1.40	1.72
Adjusted MPE Ratio	0.62	0.68	0.76	0.86	0.98	1.00	1.15	1.29	1.61

Table 4.13: The distribution of the ratios of adjusted radar-derived rainfall estimates to gage observations is shown in this table.

The median of the distribution of ratios of adjusted radar-derived rainfall products to gage-observed rainfall appears to be near 1, as shown by the distribution in Table 4.13. The minimum ratio of the adjusted convective radar-derived rainfall is 0.36 and the maximum is 2.75. For the adjusted MPE, the minimum ratio is 0.21 and the maximum bias is 3.13. The standard deviation of both adjusted radar-derived rainfall products is 0.46. There does not appear to be a large difference between using the adjusted MPE or the adjusted radar-derived rainfall product. Both exhibit wide variability in bias within a single event. However, the mean biases tend to be relatively close to 1 as compared to the biases for unadjusted radar-derived rainfall estimates.

Event	**Gage Min. (mm)**	**Gage Max. (mm)**	**Adj. Conv. Radar-Derived Rainfall Min. (mm)**	**Adj. Conv. Radar-Derived Rainfall Max. (mm)**
May 19, 2004 at 07 UTC	5.3	32.8	8.5	65.6
July 6, 2004 at 13 UTC	13.8	34.7	19.9	36.5
August 4, 2004 at 08 UTC	24.4	34.3	12.7	28.4
August 4, 2004 at 09 UTC	14.4	30.3	9.3	38.3
August 26, 2004 at 06 UTC	26.0	73.2	35.7	71.6
August 26, 2004 at 07 UTC	4.1	20.7	1.2	26.8
August 27, 2004 at 18 UTC	1.3	29.5	1.0	27.0
October 18, 2004 at 10 UTC	5.1	19.9	4.5	32.4

Table 4.14: The minimum and maximum rainfall totals observed at gages in the catchment are shown compared with the minimum and maximum rainfall totals estimated in the catchment by the adjusted convective radar-derived rainfall.

Event	Gage Min. (mm)	Gage Max. (mm)	Adjusted MPE Min. (mm)	Adjusted MPE Max. (mm)
May 19, 2004 at 07 UTC	5.3	32.8	13.8	48.2
July 6, 2004 at 13 UTC	13.8	34.7	15.4	22.2
August 4, 2004 at 08 UTC	24.4	34.3	15.7	28.2
August 4, 2004 at 09 UTC	14.4	30.3	15.6	23.4
August 26, 2004 at 06 UTC	26.0	73.2	31.5	95.2
August 26, 2004 at 07 UTC	4.1	20.7	1.3	20.8
August 27, 2004 at 18 UTC	1.3	29.5	2.1	47.1
October 18, 2004 at 10 UTC	5.1	19.9	2.4	12.8

Table 4.15: The minimum and maximum rainfall totals observed at gages in the catchment are shown compared with the minimum and maximum rainfall totals estimated in the catchment by the adjusted MPE.

Tables 4.14 and 4.15 show the minimum and maximum rainfall within the catchment estimated by the radar-derived products and compares them to gage observations. In many cases, the minimum and maximum rainfall estimated are within a few millimeters of the observed values. However, in some cases, the maximum rainfall estimated is much larger than the maximum observed rainfall within the catchment. To a lesser extent, this is also observed when examining the minimum rainfall and minimum estimated rainfall in the catchment. This is consistent with the strong variation in bias during a single rainfall event from gage to gage as suggested previously.

Case	Adj. MPE Vol.	Adj. Conv. Radar-derived Vol.	ASOS/MCC/USDA-ARS Vol.
May 19, 2004 at 07 UTC	218070	202150	151761
July 6, 2004 at 13 UTC	200503	152968	161696
August 4, 2004 at 08 UTC	164428	171426	218221
August 4, 2004 at 09 UTC	160574	141399	146941
August 26, 2004 at 06 UTC	411373	500361	455055
August 26, 2004 at 07 UTC	72589.5	60314.8	80934.9
August 27, 2004 at 18 UTC	115863	179185	127190
October 18, 2004 at 10 UTC	82017.9	55850.5	78513.3

Table 4.16: Shown is the volume of water accumulated in the catchment in units of cubic meters during the duration of the event.

The total volume of rainfall estimated in the catchment for each adjusted radar-derived rainfall product is shown in Table 4.16 and is compared with the interpolation using the ASOS, MCC, and USDA-ARS rain gage networks. Although there is still some variability between the volume of rainfall accumulated using the radar-derived products and the volume of water accumulated using the interpolation ASOS, MCC, and USDA-ARS networks, it is less than the variability between estimated rainfall and gage observations. In most of the cases, the variation between the volume from radar-derived rainfall estimates and the volume from the interpolation of data from the ASOS, MCC, and USDA-ARS networks was under 25%.

4.3. Discussion of Results

A number of findings were made during the course of this study regarding the usefulness of different radar and rain gage networks to estimate the rainfall in the Goodwater Creek catchment. Most notably, the use of surrounding rain gage networks to estimate rainfall within the catchment performed very poorly and the network is unsuitable for estimating rainfall within the catchment. The rain gage networks surrounding the catchment both severely underestimated the rainfall and failed to accurately represent the spatial distribution of rainfall within the catchment. This indicates the need for a gage within the catchment to accurately represent the rainfall that occurred in the catchment.

Concerning radar products, when applying a convective Z-R relationship to reflectivity or when using the MPE data, which is derived in part from radar observations, the rainfall within the catchment was still underestimated in most situations. The bias of radar-derived products compared against rain gage observations varied greatly from event to event and from gage to gage during an event. This suggests that the ability of the radar products used here to accurately represent the spatial distribution of rainfall within the catchment is very limited at best.

There are a number of reasons why the performance of the radar-derived products may have been poor. One reason is that the height of the lowest elevation of the radar beam is over 2,000 m above ground over the catchment. Many processes may occur beneath the level at which the radar is scanning, including merging and splitting of raindrops, evaporation, and wind drift. Additionally, the choice of a convective Z-R relationship may not have been appropriate for all of these events.

Although the convective Z-R relationship is frequently used in the central United States, it is unclear as to whether is suited for relating reflectivity to convective rainfall during the summer. Often, an air mass with very tropical characteristics is situated over the central United States. Characteristics of this air mass include weak vertical wind shear, abundant moisture, moderate to strong instability, and warm temperatures both at the surface and aloft. These factors, along with the concentration of cloud condensation nuclei, can influence the drop size distribution of the rainfall and variations that may occur between the height at which the radar is scanning and the rainfall at the surface. These characteristics are also true of tropical airmasses such as those frequently found along the Gulf Coast, for example. Most of these cases were during the summer and it may have been appropriate to use the Rosenfeld tropical Z-R relationship instead of the WSR-88D convective Z-R relationship.

The MPE underestimated rainfall to a greater extent than did the convective radar-derived rainfall product. This is likely due to the postprocessing of rainfall estimates that were initially derived from reflectivity. It is unlikely that any rain gages within the catchment are used to pair radar estimates of rainfall to rain gage observations. If the calibration is done on the basis of rain gages outside the catchment, it may cause the rainfall within the catchment to be poorly represented.

This does not, however, explain fully the bias toward underestimating rainfall that was exhibited by the MPE. An additional reason is possibly the use of PRISM climate data in calibrating the rainfall. Although the climate data is likely useful in calibrating radar-estimated rainfall in typical events, most of the cases that were selected were atypical events. The frequency of rainfall events plotted against the intensity of the event would likely fit well to a curve resembling an exponential distribution. As the intensity of the event increases, the frequency of the event decreases. However, these events are very important to measure accurately because they can be responsible for flooding and other adverse effects such as soil erosion and transport of chemicals. The high-end convective events are likely to be poorly represented by climatology as compared to more typical rainfall events. This is another possible reason for the bias of underestimating rainfall in the catchment.

The adjustments applied to the radar-derived products do well to greatly limit the mean ratio of estimated rainfall to gage observations when averaged over several events. For individual events, adjusting radar-derived rainfall products based on a single gage within the catchment does not necessarily eliminate the difference between radar-derived rainfall estimates and gage observations at other locations. There is still a high degree of variation in the ratio of radar-derived rainfall estimates to gage observations from one location to another and from one event to another.

Despite the limitations in accurately modeling the finescale structure of rainfall over the catchment, the adjustments to the radar-derived rainfall estimates generally performed well in estimating the volume of rainfall over the entirety of the catchment. Although the techniques applied in this study to estimate rainfall using radar data may be unsuitable for use at individual sub-basins within the catchment, it may still be useful in estimating the total volume of rainfall over the entire catchment. One gage may be suitable for calibrating rainfall estimates over a catchment. Additional gages or more advanced techniques are needed to accurately estimate rainfall at individual locations within the catchment.

One such technique for improving upon the estimates of rainfall within the catchment is to apply a more advanced technique to choose an appropriate Z-R relationship. While it is likely that the WSR-88D convective Z-R relationship would perform quite well in some instances, other Z-R relationships may be more appropriate for midsummer convection in particular. Creating an algorithm to choose between multiple convective Z-R relationships may produce better results. In particular, the Rosenfeld tropical Z-R relationship is designed to produce higher rainfall rates, particularly for higher reflectivity. This may be a more appropriate choice of a Z-R relationship for some of the events. Assuming the typical hail cap of 53 dBZ in the central United States, it is impossible to achieve some of the rainfall rates during the event on August 26, 2004 at 06 UTC. Applying a Z-R relationship better suited for tropical convection, possibly along with raising the hail cap, may produce more realistic estimates of rainfall in these situations. Increasing the hail cap is likely appropriate considering the warm vertical profile typically associated with a tropical air mass. Additionally, the presence of abundant moisture, strong instability, and weak shear likely affects the drop size distribution. For these reasons, the Rosenfeld tropical Z-R relationship may be more appropriate in some instances. The remainder of this work focuses on an attempt to develop an algorithm to choose an appropriate Z-R relationship in an objective manner and apply it to radar-observed reflectivity to estimate rainfall.

Chapter 5

Rainfall Type Algorithm Methodology

The purpose of this chapter is to describe the background of the algorithm used for applying mutliple Z-R relationships within a single radar image. This includes explaining the mathematical basis of the algorithm and describing some of the tools used in performing the processing. The steps of the algorithm are described at the end of the chapter.

5.1. Purpose of Algorithm

The results of the work presented in Chapter 4 indicate that merely applying the WSR-88D convective Z-R relationship to reflectivity tended to underestimate rainfall. Although this could be attributed to poor radar coverage, it may also be due to the choice of an unrealistic Z-R relationship. The purpose of the algorithm is to choose an appropriate Z-R relationship based on radar observations and apply it to the radar observations. The choice of an appropriate Z-R relationship took into account many of the suggestions in Section 4.3. The algorithm that was developed was then evaluated using the eight cases described in Section 3.4. Although verifying the processing done by each step of the algorithm is difficult and subjective, the end result of the algorithm can be evaluated against actual rain gage observations.

5.2. Identifying Precipitation Type and Structure

The algorithm relies heavily on spectral analysis, which is accomplished through use of the Fourier Transform (FT). The mathematical basis for the FT is described extensively in Appendix D. This section will focus just on what the FT accomplishes without an extensive mathematical discussion. Additionally, the focus of this section will be on the use of the Discrete Fourier Transform (DFT).

The FT operates on an infinite domain and using continuous data. Although this is mathematically feasible, it is not possible using actual observed data sets. Domains are finite and data are collected at discrete intervals. The continuous form of the FT is not suited for this, and as a result, a discrete form of the transform, the DFT, is used.

The basis of the FT is to take a signal, regardless of ithe number of dimensions, and to transform it from the spatial domain to the frequency domain. In the spatial domain, the independent variables represent a position in space. The dependent variable is a power at the location specified by the independent variables. In the case of a radar image, the independent variables x and y represent a position on a grid and the dependent variable is reflectivity at that location. However, in the frequency domain, the independent variables represent wave numbers. Greater wave numbers indicate higher frequencies and shorter wavelengths. The dependent variable is the power of the wave with the wave numbers specified by the independent variables. In two dimensions, wave numbers u and v are used where u is the wave number in the x direction and v is the wave number in the y direction. This process is known as analysis of a signal or as decomposition.

The reason for transforming a signal or image from the spatial domain to the frequency domain is that some operations can be more easily performed in the frequency domain. This is more clearly explained by the Convolution Theorem, which states that multiplication in one domain is equivalent to convolution in the other domain. In particular, Gaussian filtering can be accomplished through multiplication in the frequency domain. This operation would be equivalent to convolution in the spatial domain.

Upon completing any operations in the frequency domain, it is possible to back transform the signal from the frequency domain into the spatial domain. A similar transform, the Inverse FT (IFT) is used to accomplish the transform to the spatial domain. As with the FT, both continuous and discrete forms of the IFT exist. For observed data sets, the discrete form of the IFT is used. This process is known as synthesis of a signal or as recombination.

The mathematics of the FT and IFT are beyond the scope of this chapter and are explained in Appendix D. For the purpose of this work, the FT is used to analyze a radar image and identify precipitation structures. Stratiform rain is frequently characterized as covering a broad area with relatively weak reflectivity and gradients in reflectivity as compared to convective precipitation. Convection usually occurs over smaller areas than stratiform precipitation and is characterized by strong localized updrafts and additionally strong but small reflectivity cores associated with downdrafts. Classification between convection and stratiform precipitation through horizontal reflectivity gradients, which is roughly equivalent to this description, was proposed by Klazura *et al.* (1999). Because of the larger size and weaker horizontal reflectivity gradients of stratiform precipitation, it should be manifested in the frequency domain as a low frequency signal. Convective precipitation, which occurs with stronger horizontal reflectivity gradients, should be manifested as strong power in higher frequencies. Gaussian filters can be used to isolate frequency bands of interest and retain the signal in those bands while attenuating the signal in other bands. Discrimination between convective and stratiform precipitation was accomplished in this work through Gaussian filtering and retaining signals in empirically derived frequency bands.

Similar procedures can be used to identify clusters of thunderstorms or individual storms. Clusters of storms are larger than individual storms and therefore should have a greater wavelength and lower frequency. Additionally, areas identified as storms should, as a prerequisite, be areas of convection. This forms the basis for discriminating between convective and stratiform precipitation and identifying thunderstorms at multiple scales. The detailed description of this algorithm is beyond the scope of this section and is described in detail in Appendix F.

5.3. Evaluating Thunderstorm Organization

It is also of interest to evaluate the organization of thunderstorms. Even during the summer in the central United States, organized thunderstorm activity is frequently associated with mid-latitude weather systems. As mid- and upper-level winds increase near mid-latitude cyclones, vertical wind shear is likely to increase. As a result, thunderstorms are more likely to organize into multicell clusters, multicell lines, and even supercells than in a weakly sheared environment. A Z-R relationship designed for use with tropical convection may be appropriate for air mass thunderstorms and other poorly organized thunderstorm activity. However, as thunderstorm organization increases, a Z-R relationship associated with mid-latitude convection may be more appropriate.

The algorithm that was developed made use of two ways to determine thunderstorm organization. One method was to detect the presence of rotation, which would typically be associated with the rotating updraft of a supercell thunderstorm or bookend vortices that are commonly associated with bow echoes. Rotation in thunderstorms is one indicator of organized thunderstorm activity. A second method is to approximate the shape of a thunderstorm as an ellipse and use the eccentricity of the ellipse to evaluate whether or not a storm is linear or quasi-linear in shape.

5.3.1. Detecting Rotation in Thunderstorms

A preliminary study was conducted to attempt to detect rotation in thunderstorms using radial velocity as detected by radar. The primary goal of the study was to attempt to distinguish between supercells and non-supercells. The algorithm described in Section 5.2 and Appendix F was used to detect storms in 27 cases. In these 27 cases, 314 storms were identified.

These storms were considered supercells if they were either a discrete supercell or were a cluster of thunderstorms containing an embedded supercell. For each of the storms identified, a subjective determination was made as to whether or not the storm was a supercell. The classification was based primarily on examining reflectivity to determine the organization of thunderstorms and examining radial velocity for persistent rotation. Thunderstorms that appeared to be poorly organized, such as air mass thunderstorms, were not identified as supercells. Linear thunderstorms were also not identified as supercells. Several tilts of radial velocity were examined in several successive volume scans for evidence of persistent rotation. If persistent rotation was found and the storm was not linear nor disorganized, it was identified as a supercell in the subjective analysis.

Shear vorticity was calculated using the w2circ algorithm (Smith and Elmore, 2004) and interpolated to a latitude-longitude-height grid using w2merger (Lakshmanan *et al.*, 2006), both of which are algorithms in WDSS-II (Lakshmanan *et al.*, 2007b). The shear vorticity was averaged over the lowest four kilometers above mean sea level and was smoothed using a low-pass filter. The strongest shear vorticity within each storm was identified. Shear vorticity strength of $0.002 s^{-1}$ was found to be a good discriminator between supercells and non-supercells. Approximately 80% of the supercells identified in the subjective analysis exhibited rotation stronger than the threshold and approximately 80% of the non-supercells identified in the subjective analysis exhibited rotation weaker than the threshold.

The threshold of $0.002s^{-1}$ is on the same order of magnitude as previous thresholds used in identifying mesocyclones. Stumpf *et al.* (1998) provided a good description of two mesocyclone detection algorithms. The mesocyclone detection algorithm implemented prior to that required vorticity of $0.006s^{-1}$ within 100 km of the radar. The required vorticity strength decreased linearly to $0.003s^{-1}$ at a distance of 200 kilometers from the radar, and remained constant at greater distances. The algorithm they devised by halved the vorticity thresholds but retained the range dependence from the radar. Additionally, the algorithm ranked mesocyclones as stronger as the vorticity increased.

The vorticity threshold of $0.002s^{-1}$ is approximately equivalent to values identified in previous work and is also consistent with what a human might identify as a supercell from examining radar imagery. Therefore it seems reasonable to use this approximate value for identifying rotating thunderstorms when determining thunderstorm organization.

5.3.2. Detecting Linear Thunderstorms

Upon identifying a thunderstorm, many metrics can be calculated, including approximating the shape of the storm. The metrics calculated by the algorithm include approximating an ellipse to the shape of the storm and then determining the eccentricity or aspect ratio of the ellipse. Large aspect ratios could be a good indicator of linear organization of storms. Using a similar method for identifying thunderstorms, Lack (2007) found that an aspect ratio of 3.2:1 is a reasonable threshold for distinguishing between linear and non-linear storms. The algorithm that was developed here also used an aspect of 3.2:1 as a threshold between linear and non-linear storms.

5.4. Selecting an Appropriate Z-R Relationship

Three Z-R relationships were used in the algorithm, which were the Marshall-Palmer Z-R relationship (equation 2.3), the WSR-88D convective Z-R relationship (equation 2.2), and the Rosenfeld tropical Z-R relationship (equation 2.6). The Marshall-Palmer Z-R relationship typically is used for stratiform precipitation, and was used for precipitation that the algorithm identified as stratiform precipitation. Rainfall from convective precipitation was estimated using either the WSR-88D convective Z-R relationship or the Rosenfeld tropical Z-R relationship, depending on the characteristics of the precipitation.

Not all convection identified by the algorithm must actually be identified as part of actual storms. Convection that was not associated with a particular storm was assigned a Z-R relationship depending on the time of year. During the summer, and in the algorithm this is defined as the months of June, July, and August, the Z-R relationship used is the

Rosenfeld tropical Z-R relationship. However, in the other months, rainfall from convection not associated with storms that have been identified is estimated using the WSR-88D convective Z-R relationship. This is primarily due to the frequent presence of tropical air masses over the central United States, which are less common on other months. It was speculated that the Rosenfeld tropical Z-R relationship could more accurately estimate higher rainfall intensities.

For storms that were identified, the characteristics of each storm determined the Z-R relationship that was used to estimate rainfall. For cases from May 15 through September 15, the algorithm chose between the WSR-88D convective Z-R relationship and the Rosenfeld tropical Z-R relationship. For cases from the rest of the year, the WSR-88D convective Z-R relationship was always used. This was done because tropical airmasses are more frequently found in the central United States during the summer and are less likely during other times of the year.

Very strong reflectivity is almost always associated with hail. Therefore if the strongest reflectivity in a storm was at or greater than 60 dBZ, the WSR-88D convective Z-R relationship was chosen. This is because tropical airmasses tend to be very warm at the surface and in a deep layer above the surface. The warm layer melts hail before it reaches the surface and also makes production of large hail very difficult. For these reasons, hail is unlikely in tropical convection, and therefore the WSR-88D convective Z-R relationship is likely to be appropriate if hail is present.

In the algorithm, if conditions for a storm were met for possible tropical convection, the Rosenfeld tropical Z-R relationship was applied. These conditions are: a climatologically favorable time of year, lack of hail, and convection that is not organized as a line or with rotation. If any one of these conditions was not met, however, the WSR-88D convective Z-R relationship was used for the storm.

5.5. Limiting Hail Contamination

It is also of interest to consider the hail cap, which limits rainfall rate to a predefined upper bound. Hail caps are implemented in rainfall estimation algorithms because hail contamination can produce unreasonably high estimated rainfall when estimating rainfall rate from reflectivity. One drawback of applying a hail cap is that it may also prevent estimation of very high rainfall rates that are realistic. Although a hail cap may not interfere with estimating most rainfall rates, it may prevent accurate estimation of unusually high rainfall rates. These unusual rainfall rates, although not frequent, are very important to measure accurately because of the possibility of flooding and extreme soil loss due to runoff. Typically, the hail cap in the central United States is set at 53 dBZ. This may be adjusted upward in other regions, such as near the Gulf Coast, where hail is less likely during the summer. Typically, near the Gulf Coast, the hail cap is used to limit rainfall rate to 150 mm hr^{-1} regardless of the Z-R relationship in use. Such a hail cap may not be reasonable, even in the central United States. Upon examining two years of data from 2003 and 2004 recorded by gages in the catchment, rainfall rates over ten minutes were observed above 150 mm hr^{-1} twice. In such situations, implementing a hail cap of 150 mm hr^{-1} will not produce good estimates of rainfall. Additionally, using the 53 dBZ hail cap and the WSR-88D convective Z-R relationship, rainfall rate is limited to 104 mm hr^{-1}, which was exceeded during four ten minute periods during 2003 and 2004. Although the hail cap is not exceeded by most storms, the data also suggests that such extreme rainfall events are not particularly rare, either.

For these purposes, the algorithm used a hail cap of 53 dBZ, or 104 mm hr^{-1}, when using the Marshall-Palmer and WSR-88D convective Z-R relationships during the months of September through May. However, during June through August, the hail cap was raised to 55 dBZ. When using the WSR-88D convective Z-R relationship, a reflectivity of 55 dBZ produces a rainfall rate of 144 mm hr^{-1}. Using a hail cap of 55 dBZ with the Marshall-Palmer Z-R relationship allows a maximum rainfall rate of approximately 100 mm hr^{-1}. The hail cap was always 52 dBZ when the

Rosenfeld tropical Z-R relationship was used. This produces a rainfall rate of 216 mm hr^{-1}. Although this is unreasonable over a significant length of time, it is possible that such a rainfall rate could occur over a short length of time. These hail caps should be sufficient for estimating most rainfall rates from radar reflectivity, including extreme events.

5.6. Procedure

The algorithm operated using a square domain with a horizontal length of 256 km and a resolution of 1 km. Each gage was matched with a single pixel, which represented a 1-km square in which the gage was located. Rainfall totals were summed over one hour, the duration of each event as defined here, and were compared against both the results that would be produced using purely the WSR-88D convective Z-R relationship and the observations made by the gages. The procedure for comparing gage observations to radar-estimated rainfall was identical to the procedure for comparing gages against other radar-derived products, which was described in section 3.5.4.

Rain gage data with observations taken every two minutes were compared against radar-estimated rainfall to investigate whether the rainfall rates produced by the algorithm were realistic. The USDA-ARS rain gage network records observations of intensity and accumulation over two minute intervals. This data was acquired for the rainfall events occurring on August 26, 2004 because the highest rainfall rates in any of the eight cases were observed during events on that day. A WSR-88D radar can only complete a volume scan as frequently as every four minutes. However, because data from two radars, located in Weldon Spring, MO (LSX), and Pleasant Hill, MO (EAX), were used, observations in areas scanned by both radars will occur more frequently than every four minutes. Because data from the two radars was composited using the w2merger algorithm (Lakshmanan *et al*, 2006), it is justifiable to compare these data against rain gage observations taken every two minutes. Data from the LSX radar were unavailable during the May 19, 2004 event. No data was available from the EAX radar during the events on August 26, 2006.

The algorithm procedure can be summarized in the following steps:

1. Identify regions of convection and stratiform precipitation
2. Identify individual storms within the convection
3. Determine the properties of individual storms such as the strongest reflectivity within the storm, whether or not rotation is present, and the aspect ratio of the storm
4. Determine at each point in the image which Z-R relationship should be used

5. Determine the hail cap that should be used at each point within the radar image
6. Apply the appropriate Z-R relationship and hail cap at each point within the radar image

Chapter 6

Results of Algorithm

The purpose of this chapter is to describe the results of using the algorithm for applying multiple Z-R relationships to a single radar image as described in Chapter 5. For the eight cases, radar estimates were only compared only at locations where a gage was located and not for the entire catchment or domain. The reader may note that radar estimates using the convective Z-R relationship in this chapter may differ from those presented in Chapter 4. This is due entirely to a different source of data. The estimates in Chapter 4 were generated from level III data, which has a precision of 5 dBZ. The rainfall estimates in this chapter used level II data, which has a precision of 0.5 dBZ. Additionally, data from two WSR-88D radars, located in Weldon Spring, MO and Pleasant Hill, MO, may affect the reflectivity that is input to the algorithm.

6.1. Algorithm Output

For every gage, in each of the eight cases, the rainfall estimate using multiple Z-R relationships produced the same or greater rainfall accumulations than by using only the WSR-88D convective Z-R relationship. It was also apparent that some of the bias of using only the

WSR-88D convective Z-R relationship as described in Chapter 4 was due to the data set. The quantization of reflectivity to 5 dBZ intervals introduced some errors. Because the scale is logarithmic, the quantization introduces a bias that causes precipitation to be underestimated. However, this error was not a factor when examining the MPE, which is not quantized in this way. Results are shown in Table 6.1 on a case-by-case basis of the average percent differences in using a single Z-R relationship and the algorithm to estimate rainfall.

Event	Conv. Z-R Difference from Observations	Multiple Z-R Difference from Observations
May 19, 2004 at 07 UTC	68.3%	83.2%
July 6, 2004 at 13 UTC	96.4%	204.5%
August 4, 2004 at 08 UTC	154.8%	211.1%
August 4, 2004 at 09 UTC	72.4%	138.9%
August 26, 2004 at 06 UTC	122.7%	155.2%
August 26, 2004 at 07 UTC	126.0%	135.3%
August 27, 2004 at 18 UTC	145.6%	172.3%
October 18, 2004 at 10 UTC	61.0%	62.8%

Table 6.1: This table shows the percent of rainfall estimated by the WSR-88D convective Z-R relationship and multiple Z-R relationships as compared to rain gage observations. These percentages computed by dividing the radar-estimated rainfall by gage observations and multiplying by 100.

It is apparent that using the multiple Z-R relationships does have an impact on the rainfall rate estimated by radar. In each of these eight cases, moderate to heavy rainfall was falling over the catchment. Just because in each of these eight cases higher rainfall rates were produced by using multiple Z-R relationships does not mean that the algorithm will always produce higher rainfall rates than the WSR-88D convective Z-R relationship. In particular, in situations where precipitation is primarily stratiform, multiple Z-R relationships as implemented in the algorithm may produce lower rainfall estimates than using the WSR-88D convective Z-R relationship. Therefore it is unclear whether the bias toward heavier rainfall being estimated by the algorithm as compared to the WSR-88D convective Z-R relationship would occur in most cases or if it is largely a result of the cases that were selected.

During the summer, there is a clear bias toward overestimating rainfall, regardless of whether or not just the WSR-88D convective Z-R relationship or multiple Z-R relationships are used. Outside of the summer, the bias was toward underestimating rainfall in the catchment. This seasonal bias may be partially due to the restriction against using the Rosenfeld tropical Z-R relationship outside of the summer. It is likely that the slightly higher rainfall rates found when using multiple Z-R relationships in the October 18, 2004 at 10 UTC event were due to the selection of the Marshall-Palmer Z-R relationship at times during the event. At weaker reflectivity, values at and below approximately 35 dBZ, the Marshall-Palmer Z-R relationship produces heavier rainfall rates than the WSR-88D convective Z-R relationship does.

Reducing the strongest reflectivity in a storm at which the Rosenfeld tropical Z-R relationship can be selected from 60 dBZ to 55 dBZ had little influence on the rainfall accumulation estimated by the algorithm. Instead, both the Rosenfeld tropical Z-R relationship and the WSR-88D convective Z-R relationship overestimate rainfall over the catchment during the summer when using this data set.

The heaviest rainfall totals in any of the cases occurred during the August 26, 2004 at 06 UTC event. During this event, radar-estimated rainfall tended to more closely match observations from gages recording the heaviest rainfall. Also of note is that the algorithm chose the WSR-88D convective Z-R relationship instead of the Rosenfeld tropical Z-R relationship throughout almost all of the event, as shown in figure 6.1.

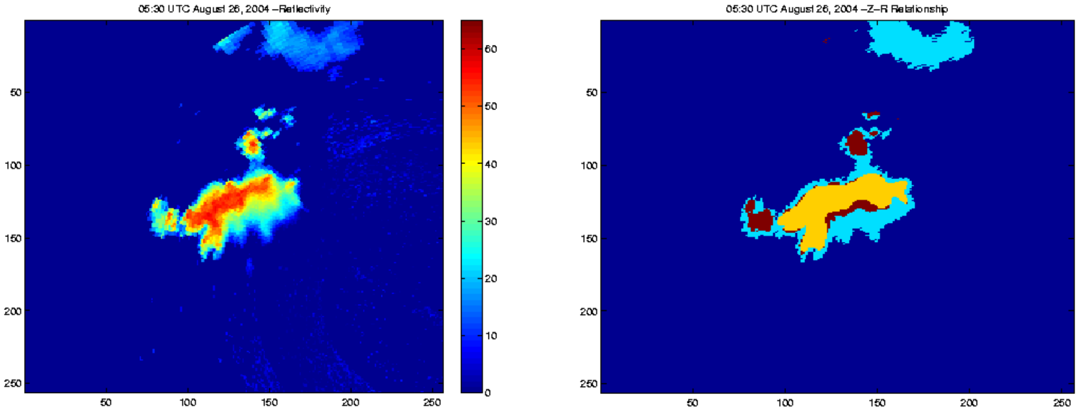

Figure 6.1: Reflectivity from 0530 UTC on August 26, 2004 is shown to the left. To the right, the Z-R relationship chosen by the algorithm is shown. Dark blue indicates areas where precipitation was not occurring. Light blue indicates where the Marshall-Palmer Z-R relationship was selected. Orange indicates where the WSR-88D convective Z-R relationship was selected. Dark red indicates where the Rosenfeld tropical Z-R relationship was used.

It is likely that choosing the Rosenfeld tropical Z-R relationship would have produced unreasonably high rainfall estimates. Rainfall totals and estimates for this event are shown in Table 6.2.

Gage	Gage-Observed Rainfall (mm)	Multiple Z-R Rainfall (mm)	Conv. Z-R Rainfall (mm)
MOGC0116	65.5	75.2 (114.7%)	61.9 (94.4%)
MOGC0125	71.6	87.9 (122.8%)	74.2 (103.5%)
MOGC0126	67.1	90.3 (134.6%)	76.9 (114.7%)
MOGC0127	25.9	59.4 (228.8%)	40.9 (157.5%)
MOGC0132	57.7	81.1 (140.6%)	63.0 (109.3%)
MOGC0134	36.8	70.5 (191.6%)	55.8 (151.6%)
MOGC0138	73.2	87.9 (120.2%)	73.6 (100.7%)
MOGC0139	60.7	98.8 (178.1%)	86.7 (142.9%)
MOGC0201	38.5	68.5 (157.8%)	49.1 (127.6%)
MOGC0203	44.7	70.5 (155.2%)	55.8 (124.9%)

Table 6.2: Gage observations and rainfall estimates using the WSR-88D convective Z-R relationship and multiple Z-R relationships during the August 26, 2004 at 06 UTC event. The percentages are comparing the radar-estimated rainfall to the gage observations.

In some instances, using a single Z-R relationship underestimated the rainfall whereas using multiple Z-R relationships overestimated the rainfall. This result suggests that neither the WSR-88D convective Z-R relationship nor the Rosenfeld tropical Z-R relationship is the appropriate Z-R relationship to relate reflectivity to rainfall rate during the event. Results from an example event, August 4, 2004 at 09 UTC, are shown in Table 6.3.

Gage	Gage-Observed Rainfall (mm)	Multiple Z-R Rainfall (mm)	Conv. Z-R Rainfall (mm)
MOGC0116	22.0	35.9 (163.1%)	17.7 (80.6%)
MOGC0125	16.7	32.6 (196.0%)	16.5 (98.8%)
MOGC0126	14.4	28.1 (195.3%)	14.7 (102.0%)
MOGC0127	21.5	15.5 (71.9%)	9.6 (44.8%)
MOGC0132	23.1	21.6 (93.4%)	13.1 (56.6%)
MOGC0134	26.9	24.7 (91.9%)	13.0 (48.3%)
MOGC0138	15.1	32.7 (215.9%)	16.4 (108.5%)
MOGC0139	17.1	26.9 (157.1%)	13.8 (80.7%)
MOGC0201	30.3	32.8 (108.1%)	16.2 (53.5%)
MOGC0203	25.8	24.7 (95.8%)	13.0 (50.3%)

Table 6.3: Gage observations and rainfall estimates using the WSR-88D convective Z-R relationship and multiple Z-R relationships during the August 4, 2004 at 09 UTC event. The percentages are comparing the radar-estimated rainfall to the gage observations.

An additional comparison was done between rainfall observations taken every two minutes and radar-estimated rainfall using a single Z-R relationship and multiple Z-R relationships. Two gages were selected during the August 26, 2004 events. One gage, MOGC0138, was selected because it recorded the highest rainfall during the 06 UTC hour. The other gage that was selected, MOGC0203, produced a more typical rainfall rate during that hour. Below, four figures, 6.2 through 6.5, are presented to show the variations in rainfall accumulation over the period as well as the variation in rainfall rate.

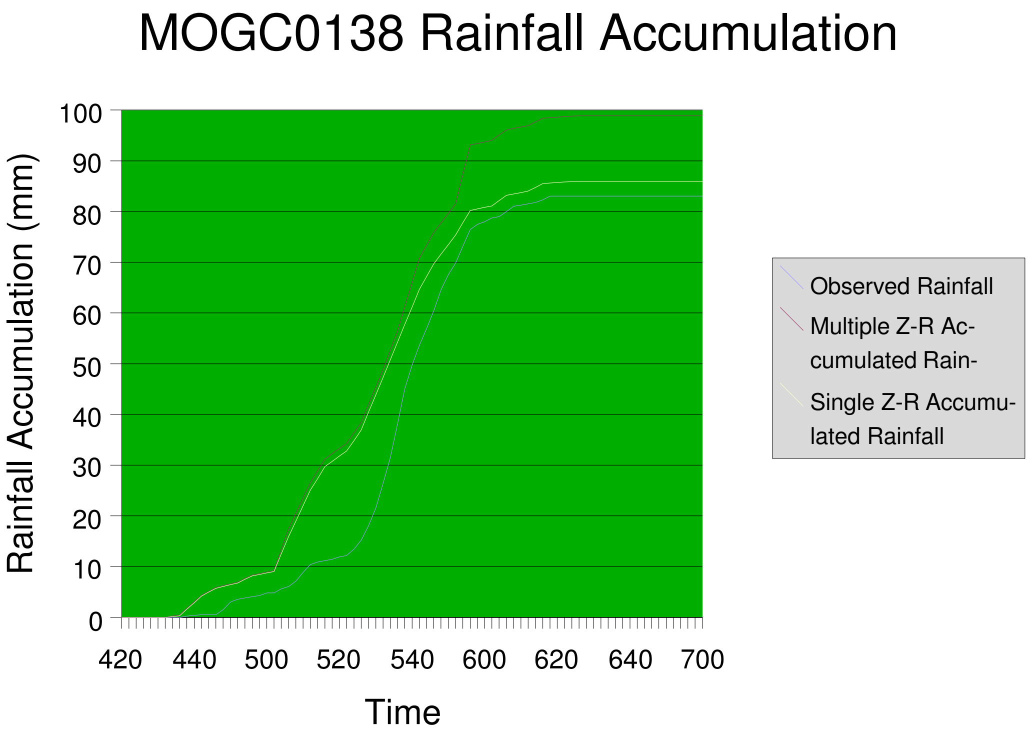

Figure 6.2: Rainfall accumulation at the gage MOGC0138 beginning at 0420 UTC on August 26, 2004 and recording until to 0700 UTC.

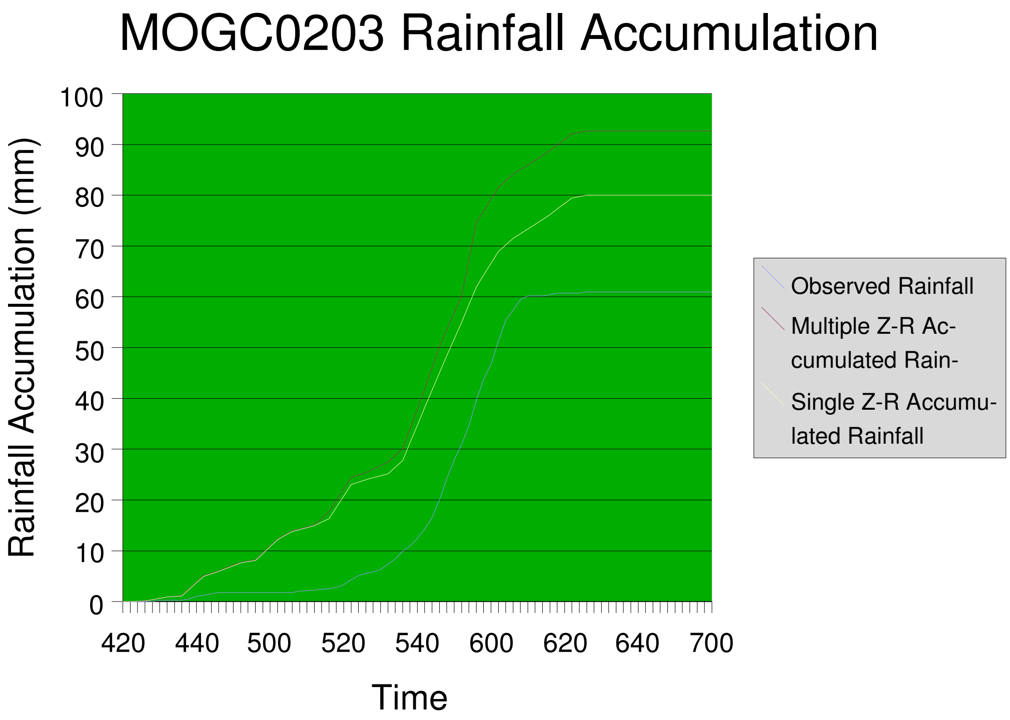

Figure 6.3: Rainfall accumulation at the gage MOGC0203 beginning at 0420 UTC on August 26, 2004 and recording until to 0700 UTC.

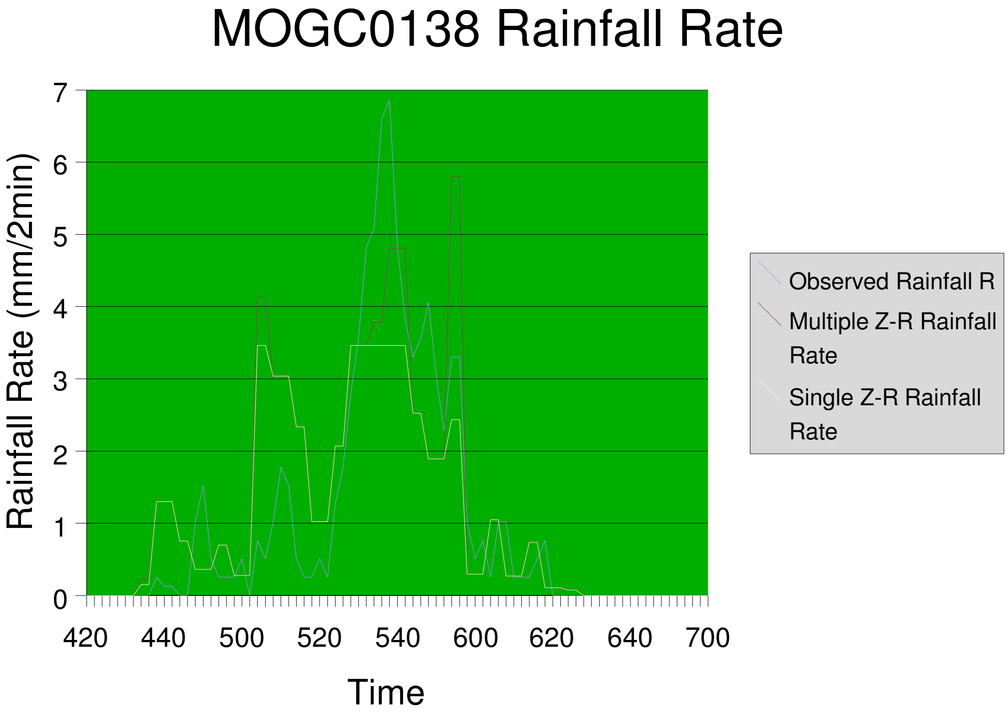

Figure 6.4: Rainfall rate at the gage MOGC0138 beginning at 0420 UTC on August 26, 2004 and recording until to 0700 UTC.

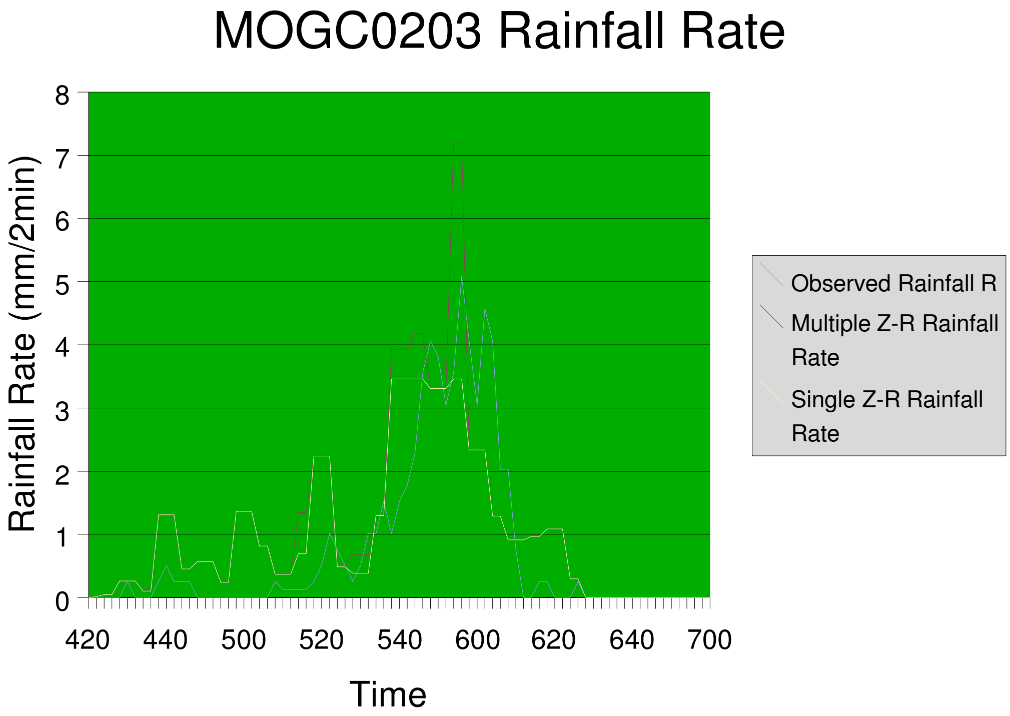

Figure 6.5: Rainfall rate at the gage MOGC0203 beginning at 0420 UTC on August 26, 2004 and recording until to 0700 UTC.

Much of the overestimation of rainfall appears to occur at lower actual rain rates when the Z-R relationships produce much higher rainfall rates than were actually observed. It did not appear that overestimating the highest rainfall rates led to most of the error. Instead, overestimating rainfall rate for an extended period of time at times when actual rain rates were lower led to a large portion of the error. In some instances throughout the data, increases in estimated rainfall rate occurred a few minutes before the actual rainfall rate was observed to increase. This could be explained by the time needed for a raindrop to fall from the height at which the radar is scanning to the surface or possibly a mismatch in time stamps. It is also apparent that the hail cap is frequently reached when applying the WSR-88D convective Z-R relationship and this is a source of underestimating rainfall.

6.2. Discussion of Results

There are several conclusions to be drawn from these results. One important conclusion, when comparing against results presented in Chapter 4 from the same events is that the data set plays a role in affecting the rainfall rate that is estimated by radar. It is clear that choosing multiple Z-R relationships within a single radar image can produce greatly different rainfall estimates than would be calculated using a single Z-R relationship. Additionally, the choice of Z-R relationships in this algorithm yielded higher rainfall rates than what would be produced using WSR-88D convective Z-R relationship. The adjustments seem to aid in estimating the heaviest rainfall produced by a storm, but also tend to greatly overestimate lighter rainfall rates. This suggests that not only is the appropriate Z-R relationship highly variable throughout a single radar image, but also even within a single storm.

6.2.1. Effects of Different Data Sets

Although level III data may be suitable for estimating rainfall when reflectivity is relatively weak, it is less suited for estimating rainfall in situations where reflectivity is stronger. This is due to, when working with reflectivity in units of dBZ, the exponential increase in rainfall rate as reflectivity becomes stronger. As a result, the difference in rainfall rate between 20 dBZ and 25 dBZ is much less than the difference in rainfall rate between 45 dBZ and 50 dBZ. It is unclear if the use of data from two radars, both of which scan over the catchment, also affected the rainfall estimate.

It is also apparent that precise measurements of reflectivity are needed to properly estimate high-intensity rainfall. This relates to not only the source of the data but also to the calibration of the radar. In particular, a poorly calibrated radar could cause significant overestimation or underestimation of the heaviest rainfall within a storm.

The distance from the radar and interpolation used in generating the data set may also adversely affect the output of the algorithm. Although a single pixel in the domain had an area of 1 km^2, the area of a single range bin is actually greater. The reflectivity observed is an average across the entire range bin and may not be representative of the reflectivity at the actual gage location. Although this would generally cause rainfall to be underestimated, it is another source of error.

6.2.2. Z-R Relationship Selection

The Rosenfeld tropical Z-R relationship may be appropriate in estimating the heaviest rainfall that could be possible from a storm. This could be useful in flash flooding events. However, in areas where rainfall is lighter, the WSR-88D convective Z-R relationship, or even the Marshall-Palmer Z-R relationship may be better suited to estimating rainfall.

In several instances, the WSR-88D convective Z-R relationship underestimated rainfall while using multiple Z-R relationships overestimated rainfall. This suggests that, at least in those instances, that neither Z-R relationship is appropriate for estimating rainfall but instead that an intermediate rainfall estimate should be used. It may be more realistic to transition smoothly from one Z-R relationship to another instead of transitioning abruptly at the edge of a storm. Additional processing could be done to choose different Z-R relationships within a single storm. For example, one could expect the heaviest rain near the centroid of the storm, and an appropriate Z-R relationship could be applied. However, elsewhere in the storm, a different Z-R relationship may be more appropriate. This would preserve the ability of the algorithm to detect the heaviest rainfall rates within a storm while limiting the overestimation of rainfall at other locations.

In other cases, the heaviest rainfall was estimated well, but lesser rainfall totals were overestimated by radar. Although the reasons for this are not entirely clear, the finding is consistent with other studies. For example, Fulton (1999) investigated radar-estimated rainfall during a flash flooding event in Colorado. The radar, during the case study, was found to overestimate rainfall by about 60% over the entire scanning domain. However, Fulton (1999) also found that rainfall estimates from the storm that produced the flash flooding were very close to the total observed by a gage near the location. Additionally, Fulton (1999) adjusted the hail cap and found that, although rainfall accumulations were decreased, they still were well above gage observations. Speculated reasons for the overestimation of rainfall included a poor choice of Z-R relationship or a radar that was poorly calibrated at measuring reflectivity. If the errors noted in Fulton (1999) are partially due to a poor choice of a Z-R relationship, but in some regions the radar estimated rainfall well, it emphasizes the usefulness in applying multiple Z-R relationships across a single domain.

Both the WSR-88D convective Z-R relationship and the algorithm using multiple Z-R relationships did not do a poor job of estimating the highest rainfall rates. In some instances, these were actually underestimated, partially due to the effects of the hail cap. These Z-R relationships seem somewhat appropriate for estimating rainfall in the portion of the storm where the rainfall is heaviest. However, through periods of lighter rain, the WSR-88D convective Z-R relationship and the algorithm using multiple Z-R relationships tended to overestimate rainfall. This suggests that another Z-R relationship may be better suited for estimating rainfall during these times. It is also entirely possible that rainfall was overestimated during those times because the radar was scanning approximately 2,300 m above the surface and most or all of the raindrops may have evaporated before reaching the surface.

6.2.3. Hail Cap Effects

It is also notable that, in many instances, instantaneous rainfall rates were at the maximum permitted by the hail cap that was selected. Additionally, some storms were identified as organized convection at some times during an event and not identified as organized convection at other times. For these reasons it is unsuitable to use the algorithm in its current form to estimate instantaneous rainfall rates or rainfall accumulation over a very short period of time. However, over longer durations, such as an hour, the algorithm should perform better. It is not necessarily incorrect for a storm to be identified as organized convection and disorganized convection at different times during an event. This could be a result of a transition during the life cycle of a storm or representing that the storm is a borderline case and exhibits characteristics of both organized and disorganized convection at times. This would suggest, as well, that neither the WSR-88D convective Z-R relationship nor the Rosenfeld tropical Z-R relationship would be particularly well suited to estimate rainfall from such storms.

When using the WSR-88D convective Z-R relationship and the hail cap selected with it, rainfall was frequently underestimated during the heaviest rainfall observed in the storm. This was not an issue when the Rosenfeld tropical Z-R relationship was selected because the hail cap was not reached in these instances. During extended periods of heavy rainfall, the hail cap may lead to significant underestimation of rainfall. This is not a desirable result because, although these heaviest rainfall rates are uncommon, extended periods of heavy rainfall are capable of causing flooding. This occurred even when using the algorithm because the Rosenfeld tropical Z-R relationship was not chosen in some of these instances. Therefore higher and more accurate rainfall rates were not possible with the chosen Z-R relationship, leading to underestimated rainfall.

6.2.4. Other Sources of Error

There are a number of other errors that may be a factor in the overestimation of rainfall. One is that during heavy rainfall events, rainfall is most likely to be underreported by gages. The gages in the USDA-ARS network are weighing rain gages, which are not prone to underestimating rainfall in the same ways as tipping-bucket rain gages. Wind is still a factor in causing rainfall to be underestimated. Although in many instances, it is likely that radar still overestimated the rainfall, it would be to a lesser degree than is indicated by the results. It is also likely that because of the height at which the radar is scanning is well above the surface that other influences such as wind drift and evaporation may affect the rainfall totals. Although evaporation is likely to lead to radar overestimation of rainfall, it is unclear whether wind drift would introduce a bias. It is quite possible that due to the generation of a cold pool at the surface that winds would spread the rain over a larger area. Because the radar is scanning well above the surface, it would not be possible to detect this occurring.

6.3. Future Work

For these reasons, it may be necessary to use different methods in intercomparing rainfall estimates with gage observations. It may be more useful to pair a gage with a neighboring pixel instead of the pixel directly above the gage to more closely match the observed rainfall. This is one possible method to compensate for wind drift, both in terms of background winds and winds induced by the storm. Another problem that depends on range is the size of a single range bin at the distance at which the catchment is from the radar.

6.4. Summary

The conclusion from this work is that there is some usefulness in applying multiple Z-R relationships within a single radar image. Although the algorithm likely suffers from a poor choice of a Z-R relationship in some instances and also the inability to apply multiple Z-R relationships within a single storm, it does suggest that applying such a technique does have a significant impact on rainfall estimation.

The greatest overestimation of rainfall occurred during the summer months. For the two cases outside of the summer months of June, July, and August, rainfall tended to be underestimated by radar. This was contrary to the hypothesis that rainfall during the summer would be underestimated by radar. It may be necessary to, instead of having a seasonal dependence on the choice of Z-R relationship to instead use actual meteorological parameters, either from surface observations or numerical model output.

It is clear that there is some usefulness in applying multiple Z-R relationships to a single radar image, but also that additional work is also needed. Some of the heaviest rainfall estimates produced may actually be reasonable. That suggests that there may, indeed, be some use for the Rosenfeld tropical Z-R relationship in the central United States. However, also of importance is to limit the overestimation of rainfall in other areas. In many instances, a large degree of variability in rainfall was noted across the catchment. This was less evident in the radar-estimates of rainfall.

Chapter 7

Conclusion

The results of this project indicate that a sparse network of rain gages, such as the ASOS and MCC rain gage networks cannot accurately detect the rainfall from localized high-intensity convective rainfall events. This leads to poor detection of both the location and intensity of the heaviest rainfall during a heavy rainfall event, if the event is even resolved by the rain gage network. Other alternatives exist, such as deploying many rain gages over an area, as was done by the USDA-ARS network. However, due to the expense of deploying such a network, the primary goal of this work was to determine the usefulness of radar-estimated rainfall as a substitute for a very dense network of rain gages.

The usefulness of radar to estimate rainfall depends both on the temporal and spatial scales at which an estimate is needed. Radar estimates likely are insufficient for detecting rainfall at small scales, both temporally and spatially. This was demonstrated by adjusting the radar-estimated rainfall by comparing the initial estimate to a single gage. Although the overall volume of rainfall within the catchment was reasonable, following the adjustment, there were still large errors at individual gages. This was also demonstrated by the inability of radar to estimate the highest intensities of rainfall that were observed. For these reasons, it is apparent that radar-estimated rainfall may be reasonable for large time and spatial scales such as on the order of at least an hour in length and for a catchment of at least the size of the Goodwater Creek catchment. At smaller scales, other processes, likely including wind drift and variations in drop size distribution due to wind and merging and splitting of raindrops make radar estimates less accurate.

Additionally, there is a limited area over which gages can be used to calibrate radar-estimated rainfall. This was demonstrated by the underestimation of rainfall by the MPE in nearly every case. It is likely that the MPE performs better in areas where a gage is present from which to calibrate rainfall estimates. The MPE is also limited in estimating high-intensity rainfall events because of the influence of climatological parameters in estimating rainfall and the relatively unusual nature of high-intensity rainfall events such as those that were chosen for this project.

The choice of an appropriate Z-R relationship is also highly variable in space and time. It varies between convective and stratiform precipitation, but also within storms. Results showed that from one time to the next, the characteristics of a storm may change necessitating the use of a different Z-R relationship. Additionally, different Z-R relationships may be needed even within a single storm at a single time. It is likely that the drop size distribution varies from the core of a downdraft of a storm to the outer edges of where rainfall is occurring. This would be due to greater saturation and less evaporation within the core of the downdraft as well as less influence of wind on larger hydrometeors within this region of a storm. The growth of raindrops is also influenced by the strength of the updraft. It may be difficult to assess this from radar imagery and it may also not be particularly useful to use numerical model output for these purposes. Although models may be quite useful in assessing the environment around storms or even within large regions of stratiform precipitation, they are far less likely to be useful when assessing the environment within a storm. It may be more useful to apply conceptual models of the distribution of the heaviest rainfall within a storm by weighting it so the heaviest rain occurs near the estimated centroid of the storm.

It is clear that choosing multiple Z-R relationships within a single radar image can greatly affect the estimates of rainfall. Although this led to overestimation of rainfall in some instances, the heaviest rainfall within a storm was frequently quite well estimated through using multiple Z-R relationships. Because a single Z-R relationship was applied to an entire storm in this project, this result suggests the need to adjust the selection of a Z-R relationship on an even smaller scale than just individual storms.

There is clearly some usefulness to estimating rainfall using radar observations, particularly over large enough temporal and spatial scales. However, at smaller scales, calibrations are less accurate. This is also supported by strong variability in the accuracy of rainfall estimates, even when applying multiple Z-R relationships. It is clear that variability in Z-R relationships occurs not only from one storm to another but within a single storm. It is unclear how much of the error noted in Chapter 4 was due to a poor choice of Z-R relationship at some gages, even following the adjustment, and how much was due to other factors that may also be highly variable such as wind drift.

It may be useful to derive an appropriate Z-R relationship from model output, but that alone is also insufficient with current models to select different Z-R relationships within a single storm. Without better observation networks, it is likely that conceptual models will need to be applied within a single storm to vary the Z-R relationship and maintain the heaviest rainfall rates near the core of the storm while not overestimating rainfall in other parts of the storm.

The poor performance in some instances using multiple Z-R relationships was likely due to variability in drop size distribution with a single storm and not due to the poor choice of a hail cap or thresholds that discriminate between the selection of Z-R relationships. Instead, drop size distribution varies from one part of a storm to another, and the influence of hail contamination would be most likely only near the core of the storm.

There are clear differences between using a single Z-R relationship throughout an entire radar image and using multiple Z-R relationships for different places in a radar image. Although it is likely that there is some use in varying the Z-R relationship within a single radar image, more work is needed to refine the selection of a Z-R relationship. In particular, it is probably necessary to vary the selection of a Z-R relationship not just from one region of a radar image to another or one storm to another but also within a single storm.

Although it is evident that the algorithm developed to apply multiple Z-R relationships within a single domain needs to be defined, the concept was successfully demonstrated. The algorithm did objectively identify regions where different Z-R relationships could be applied. Additionally, it was demonstrated that using mutliple Z-R relationships within a single domain can yield significantly different rainfall rates and totals than would be produced by using a single Z-R relationship.

References

Atlas, D., 1959: Meteorological “angel” echoes. *J. Atmos. Sci.*, **16** (1), 6-11.

Austin, P. M. and A. C. Bemis, 1950: A quantitative study of the “bright band” in radar precipitation echoes. *J. Atmos. Sci.*, **7** (2), 145-151.

Battan, L. J., 1973: *Radar observations of the atmosphere*. The University of Chicago Press, 324 pp.

Belville, J. D., 1999, Recommended Parameter Changes to Improve WSR-88D Rainfall Estimates During Cool Season Stratiform Rain Events. [Available online at http://www.roc.noaa.gov/ops/z2r_osf5.asp.]

Blanchard, D. C., 1953: Raindrop size distribution in Hawaiian rains. *J. Atmos. Sci.*, **10**, 457-473.

Brown, R. A., V. T. Wood, and T. W. Barker, 2002: Improved detection using negative elevation angles for mountaintop WSR-88Ds: simulation of KMSX near Missoula, Montana. *Wea. Forecasting*, **17** (2), 223-237.

Cataneo, R. A., 1969: A method for estimating rainfall rate-radar reflectivity relationships. *J. Appl. Meteor.*, **8**, 815-819.

Caton, P. G. F., 1964: A study of raindrop size distributions in the free atmosphere. Preprints, *11th Wea. Radar Conf.*, Boston, MA, Amer. Meteor. Soc., 136-141.

Diem, M., 1966: Rains in the arctic, temperate, and tropical zones. Sci. Rept., Meteorologisches Institut Tech. Hoch., Karlsruhe, Contract DA 91-591 EUC-3634, 93 pp.

Dinku, T., E. N. Anagnostou, and M. Borga, 2002: Improving radar-based estimation of rainfall over complex terrain. *J. Appl. Meteor.*, **41** (12), 1163-1178.

Fabry, F. and I. Zawadzki, 1995: Long-term radar observations of the melting layer of precipitation and their interpretation. *J. Atmos. Sci.*, **52** (7), 838-851.

Fulton, R. A., J. P. Breidenbach, D. J. Seo, D. A. Miller, and T. O'Bannon, 1998: The WSR-88D Rainfall Algorithm. *Wea. Forecasting*, **13** (2), 377-395.

Fulton, R. A., 1999: Sensitivity of WSR-88D rainfall estimates to the rain-rate threshold and rain gage adjustment: A flash flood case study. *Wea. Forecasting*, **14** (5), 604-624.

Gorelik, A. G., I. V. Gritskiv, L. A. Penyaz', and V. V. Tsykunov, 1967: Results of joint radar and ground measurements on the microstructure of precipitation. *Izvest. Akad. Nauk SSSR, Fiz. Atmos. i Okeana*, **3** (9), 961-966.

Gourley, J. J. and C. M. Calvert, 2003: Automated detection of the bright band using WSR-88D data. *Wea. Forecasting*, **18** (4), 585-599.

Imai, I., 1960: Raindrop size-distributions and Z-R relationships. Preprints, *8th Wea. Radar Conf.*, Boston, MA, Amer. Meteor. Soc., 214-221.

Jones, D. M. A., 1955: 3 cm and 10 cm wavelength radiation backscatter from rain. Preprints, *Fifth Wea. Radar Conf.*, Boston, MA, Amer. Meteor. Soc., 281-285.

Klazura, G. E., J. M. Thomale, D. S. Kelly, and P. Jendrowski, 1999: A comparison of NEXRAD WSR-88D radar estimates of rain accumulation with gauge measurements for high- and low-reflectivity horizontal gradient precipitation events. *J. Atmos. Oceanic Technol.*, **16** (11), 1842-1850.

Kondragunta, C., D. Kitzmiller, D. J. Seo, and K. Shrestha, 2005: Objective integration of satellite, rain gauge, and radar precipitation estimates in the multisensor precipitation estimator algorithm. Preprints. *19th Conf. On Hydrology*, San Diego, CA, Amer. Meteor. Soc., CD-ROM, paper 2.8.

Lack, S.A., 2007: Cell identification, verification, and classification using shape analysis techniques. Ph.D. Dissertation, University of Missouri, Columbia, MO. 141pp.

Lakshmanan, V., T. Smith, K. Hondl, G. J. Stumpf, and A. Witt, 2006: A real-time, three dimensional, rapidly updating, heterogeneous radar merger technique for reflectivity, velocity, and derived products. *Wea. Forecasting*, **21** (5), 802-823.

———, A. Fritz, T. Smith, K. Hondl, and G. J. Stumpf, 2007a: An automated technique to quality control radar reflectivity data. *J. Appl. Meteor.*, **46** (3), 288-305.

———, T. Smith, G. J. Stumpf, and K. Hondl, 2007b: The warning decision support system – integrated information (WDSS-II). *Wea. Forecasting*, **22** (3), 592-608.

Larson, L. W. and E. L. Peck, 1974: Accuracy of precipitation estimates for hydrologic modeling. *Water Resources Res.*, **10**, 857-863.

Lennon, W. W. and C. P. Thomas, 1970: A WSR-57 radar presentation of anomalous propagation of superrefraction type. *Mon. Wea. Rev.*, **98** (2), 161-163.

Lin, Y. and K. E. Mitchell, 2006: The NCEP stage II/IV hourly precipitation analyses: Development and applications. Preprints, 20*th* *Conf. on Hydrology*, Atlanta, GA, Amer. Meteor. Soc., P1.2.

Marshall, J. S. and W. M. K. Palmer, 1948: The distribution of raindrops with size. *J. Atmos. Sci.*, **5**, 165-166.

Moszkowicz, S., G. J. Ciach, W. F. Krajewski, 1994: Statistical detection of anomalous propagation in radar reflectivity patterns. *J. Atmos. Oceanic Technol.*, **11** (4), 1026-1034.

Ramana Murty, Bh. V., A. K. Roy, and K. R. Biswas, 1965: Radar echo intensities below bright band. *J. Atmos. Sci.*, **22** (1), 91-94.

Rosenfeld, D., D. Atlas, D. B. Wolff, and E. Amitai, 1992: Beamwidth effects on Z-R relations and area-integrated rainfall. *J. Appl. Meteor.*, **31** (5), 454-464.

———, D. B. Wolff, and D. Atlas, 1993: General probability-matched relations between radar reflectivity and rain rate. *J. Appl. Meteor.*, **32**, 50-72.

Sadler, E. J., R. N. Lerch, E. E. Alberts, and T. L. Oster, 2006: Long-term hydrologic database: Goodwater Creek, Missouri. Preprints, 2nd Interagency Conf. on Res. In the Watersheds, Otto, NC, U.S. Forest Service Southern Research Station, 161-169. [Available online at http://www.treesearch.fs.fed.us/pubs/28765.]

Seo, D. J., 1996: Nonlinear estimation of spatial distribution of rainfall – An indicator cokriging approach. *Stochastic Hydrol. Hydraul.*, **10**, 127-150.

——— and J. P. Breidenbach, 2002: Real-time correction of spatially nonuniform bias in radar rainfall data using rain gauge measurements. *J. Hydrometeorol.*, **3**, 93-111.

———, J. P. Breidenbach, and E. R. Johnson, 1999: Real-time estimation of mean field bias in radar rainfall data. *J. Hydrol.*, **223**, 131-147.

———, J. Breidenbach, R. Fulton, D. Miller, and T. O'Bannon, 2000: Real-time adjustment of range-dependent biases in WSR-88D rainfall estimates due to nonuniform vertical profile of reflectivity. *J. Hydrometeor.*, **1** (3), 222-240.

Smith, C. J., 1986: The reduction of errors caused by bright bands in quantitative rainfall measurements made using radar. *J. Atmos. Oceanic Technol.*, **3** (1), 129-141.

Smith, T. M. and K. L. Elmore, 2004: The use of radial velocity derivatives to diagnose rotation and divergence. Preprints, *11th Conf. on Aviation, Range, and Aerospace*, Hyannis, MA, Amer. Meteor. Soc., P5.6.

Steiner, M. and J. A. Smith, 2002: Use of three-dimensional reflectivity structure for automated detection and removal of nonprecipitating echoes in radar data. *J. Atmos. Oceanic Technol.*, **19** (5), 673-686.

Stewart, R. E., J. D. Marwitz, J. C. Pace, and R. E. Carbone, 1984: Characteristics through the melting layer of stratiform clouds. *J. Atmos. Sci.*, **41** (22), 3227-3237.

Stumpf, G. J., A. Witt, E. D. Mitchell, P. L. Spencer, J. T. Johnson, M. D. Eilts, K. W. Thomas, and D. W. Burgess, 1998: The National Severe Storms Laboratory mesocyclone detection algorithm for the WSR-88D. *Wea. Forecasting*, **13** (2), 304-326.

Vicente, G. A., R. A. Scofield, and W. P. Menzel, 1998: The operational GOES infrared rainfall estimation technique. *Bull. Amer. Meteor. Soc.*, **79**, 1883-1898.

Wexler, R. and D. Atlas, 1963: Radar reflectivity and attenuation of rain. *J. Appl. Meteor.*, **2**, 276-280.

Woodley, W. L., A. R. Olsen, A. Herndon, and V. Wiggert, 1975: Comparison of gage and radar methods of convective rain measurement. *J. Appl. Meteor.*, **14** (5), 909-928.

Appendix A. Z-R Relationships

A variety of Z-R relationships exist for estimating rain rates from radar reflectivity. Radar reflectivity is usually considered to be related to rain rates by an equation of the form of equation (2.1). The variations in Z-R relationships occur due to different types of storms and different physical processes in storms as well as differing environmental conditions, which cause variations in drop size distributions.

Typically radar reflectivity is given in decibels of power or dBZ. This can easily be converted to Z and substituted into a suitable Z-R equation. Many pairs of *A* and *b* values have been empirically determined. These values are used for a particular type of precipitation or may be specific to a geographic region.

In addition to the Z-R relationships that are used operationally and described in section 2.2, additional Z-R relationships have been developed for a variety of precipitation types. Blanchard (1953) developed an equation in (A.1)

$$Z = 31R^{1.71} \tag{A.1}$$

for orographically induced precipitation. Additional Z-R relationships for convective and orographic precipitation have since been developed.

Other Z-R relationships have been developed for use in different environmental conditions. One such attempt relates surface dewpoint

(Td) and relative humidity (RH) to the values of *A* and *b* in a Z-R relationship (Cataneo 1969). This implicitly takes into account surface temperature because relative humidity is present in the equation. The equations for calculating *A* and *b* are in equations (A.2) and (A.3) respectively.

$$A = 1.372(Td) - 4.702(RH) + 571 \tag{A.2}$$

$$b = -0.00444(RH) + 1.776 \tag{A.3}$$

Additionally, Z-R relationships have been proposed that adjust *A* and *b* based on surface temperature (Wexler and Atlas 1963). Equation (A.4)

$$Z = 295R^{1.45} \tag{A.4}$$

is a Z-R relationship to be used at a surface temperature of 0ºC and equation (A.5)

$$Z = 210R^{1.6} \tag{A.5}$$

is for a surface temperature of 18°C.

It has been noticed that there is little change in suitable Z-R relationship when scanning anywhere between the cloud base and the melting level and Caton (1964) used equation (A.6)

$$Z = 240R^{1.3} \tag{A.6}$$

as a suitable Z-R relationship. Equation (A.7)

$$Z = 263R^{1.3} \tag{A.7}$$

was determined by Gorelik *et al.* (1967) in a similar study.

Additional Z-R relationships were determined by Diem (1966) for a variety of geographic locations and also in different seasons. Imai (1960) calculated Z-R relationships for differing storm types in Tokyo, Japan. These show variation based on season, location, and storm type can significantly affect the choice of Z-R relationship.

Jones (1955) calculated Z-R relationships for a variety of storm types in central Illinois. These include equations for all types of rain in equation (A.8), thunderstorms in equation (A.9), showery rain in equation (A.10), and continuous rain in equation (A.11).

$$Z = 396R^{1.35} \tag{A.8}$$

$$Z = 486R^{1.37} \tag{A.9}$$

$$Z = 380R^{1.24} \tag{A.10}$$

$$Z = 313R^{1.25} \tag{A.11}$$

Although many other Z-R relationships have also been derived through empirical methods, this presents a good survey of some that have been presented in literature for a variety of conditions. This shows that choices of A and *b* vary greatly depending on the characteristics of precipitation, temperature, and location and there is a continuum of possible relationships.

Appendix B. Radar Errors

A wide variety of radar errors may occur under and limit the accuracy of rainfall estimates. Many of the common errors will be described in this section along with techniques for detecting the errors and mitigating their effects.

B.1. Bright Band

Austin and Bemis (1950) presented an early explanation of the "bright band" sometimes observed by radar when observing stratiform precipitation. Because the complex index of refraction is greater for liquid water than for ice, an ice crystal with the same scattering cross-section as a water droplet will have greater reflectivity. However, because of the typical shape of ice crystals, when the crystals begin to melt and become covered with water, they have a larger scattering cross-section than a typical raindrop, but have the complex index of refraction of liquid water. The result is greater radar reflectivity than for either the ice crystals or completely liquid raindrops. Bright banding is explained by the melting of ice crystals and coalescence of melting crystals to produce particularly high reflectivity. The melting layer is observed as a band when scanning at a single tilt because the beam rises as it becomes more distant from the radar and intersects the melting layer at a nearly constant height above the radar level. Ramana Murty *et al.* (1965) stated that the reflectivity profile beneath the bright band is nearly constant.

During stratiform precipitation events in California, the 0°C layer in the atmosphere was observed and was about 200 m thick according to Stewart *et al.* (1984). The greatest concentration of ice crystals was observed near the -5°C level with the crystals melting by around the time the temperature reached 2°C. The absorption of latent heat to change the phase of water from solid to liquid cooled the temperature of the air enough to maintain an isothermal layer around 0°C. Klaassen (1988) found that a lesser concentration of ice crystals increases the intensity of the bright band and that deeper and wider bright banding typically occurs during heavier stratiform rain events. Huggel *et al.* (1996) noted that the bright band is less intense when there are many small raindrops and no large raindrops. Greater intensity of the bright band is observed when there are fewer small raindrops but some large raindrops. Accounting for the bright band can improve rainfall estimates by 20% to 40%.

Fabry and Zawadzki (1995) observed that for rainfall reflectivity at or below 20 dBZ, reflectivity in the bright band is only about 8 dBZ stronger. However, for rainfall reflectivity above 20 dBZ and near 30 dBZ, the bright band may be as much as 13 dBZ stronger. Reflectivity below the level of the bright band is only about 2 dBZ stronger than reflectivity immediately above the bright band where only ice crystals are present. The aggregation and coalescence of melting ice crystals was a small contributor in the increase of reflectivity beneath the bright band.

Gourley and Calvert (2003) proposed an algorithm to detect the bright band based on radar reflectivity characteristics and Rapid Update Cycle (RUC) model output. The algorithm considers all tilts of the radar and searches for points where reflectivity immediately above and below the point decreases by at least 20%. Additionally, the reflectivity must at least be 30 dBZ to constitute a bright band. If model output indicates that the 0°C level is not at least 1 km above the height of the radar, the algorithm will not detect a bright band. The algorithm searches within a range of 10 km to 30 km from the radar site. Bright band detection is based on average reflectivity around the entire radar. Additionally, heights of the bright band are averaged over 30 minutes to produce better output. The algorithm only detects bright banding and does not make an attempt to remove or correct for bright banding.

Smith (1986) stated that the bright band can produce significant errors in the estimates of rainfall from radar reflectivity and proposed an algorithm to limit the error. In the algorithm, the bright band is detected through scanning at multiple tilts. The bright band is detected by the algorithm as a peak in radar reflectivity at the same height above the radar level when observed at multiple tilts. Additional processing is performed to minimize false positives when detecting potential bright bands. The intensity of the bright band is determined by dividing the reflectivity within the bright band by the reflectivity measured below the bright band.

Correcting the bright band in the algorithm involves calculating values for the intensity of the bright band and the power profile of the radar beam. These calculations were simplified in the algorithm because it is designed for limited computing resources. Based on these two values, a correction factor was calculated and applied every 15 minutes.

B.2. Anomalous Propagation

Battan (1973) described anomalous propagation as occurring when the path of a radar beam is greatly altered from a path during typical atmospheric conditions. Superrefraction has the effect of bending a radar beam toward the surface and subrefraction bends a radar beam away from the surface. As shown by Lennon and Thomas (1970), Atlas (1959) and others, superrefraction may cause the radar beam to intersect the surface. When this process occurs, as Battan (1973) describes, distant ground targets may greatly increase in radar imagery.

Because of the strong reflectivity sometimes associated with anomalous propagation, it can cause significant issues in using radar data to estimate rainfall. Woodley *et al.* (1975) found anomalous propagation severe enough in some instances as to completely discard cases when performing an intercomparison of radar and gage measurements of rainfall. Moszkowicz *et al.* (1994) stated that in unfiltered radar images, anomalous propagation represented 59% of rainfall estimated during one month and 97% of estimated rainfall during another month as detected by a radar in Poland.

Moszkowicz *et al.* (1994) developed a statistical method using Bayes' Theorem to detect anomalous propagation. Five parameters were used at a given location, which were derived from the angle of maximum reflectivity, the highest angle where an echo was detected, the maximum reflectivity detected, the strongest horizontal gradient in reflectivity, and the height of the echo top above the radar level. Although Moszkowicz *et al.* (1994) state that temporal characteristics of echoes were useful in subjectively determining anomalous propagation, it was not incorporated into the algorithm.

The operational WSR-88D algorithm (Fulton *et al.*, 1998) detects anomalous propagation by examining the vertical continuity of echoes. If sufficient vertical continuity is not present, an entire scan elevation may be ignored. Steiner and Smith (2002) consider not only the vertical structure of radar echoes but also the horizontal structure and variability of echoes when detecting anomalous propagation. Lakshmanan *et al.* (2007a) implemented a quality control algorithm designed to remove anomalous propagation and other unwanted echoes in the w2qcnn algorithm in the Warning Decision Support System – Integrated Information (Lakshmanan *et al.*, 2007b). The algorithm uses a neural network and examines the lowest two tilts of radar data using values calculated based on reflectivity, velocity, and spectrum width along with other horizontal and spatial characteristics.

B.3. Beam Filling

Rosenfeld *et al.* (1992) observed that in storms with sharp reflectivity gradients, if only part of a radar beam was filled, rainfall would be overestimated in some areas. However, this also usually results in underreporting the maximum reflectivity, due to sampling with weaker reflectivity. Additionally, at a long range, reflectivity is underestimated frequently because the radar beam is above part or all of the strongest reflectivity. Klazura *et al.* (1999) observed that rainfall observed at distant ranges associated with precipitation that was likely convective in nature was typically overestimated. However, precipitation that was likely stratiform in nature was underestimated at all ranges, possibly due to the radar beam being partially or completely above the strongest reflectivity. Operationally, the WSR-88D radars can attempt to correct for underestimation of beam hight at distant ranges from the radar (Fulton, *et al.* 1998).

Seo *et al.* (2000) proposed an algorithm for using statistical properties of the vertical structure of observed reflectivity to adjust estimated rainfall rates in areas where the radar beam is above the strongest reflectivity. This algorithm also determines the maximum distance at which radar estimates of rain rate is reliable, beyond which overshooting occurs.

B.4. Beam Blockage

In regions of complex terrain, the radar beam may be partially or completely blocked. The effects of beam blockage are significant enough that the operational rainfall estimation algorithm used by WSR-88D radars applies a correction factor or completely discards data at some elevations for some locations if beam blockage is significant enough (Fulton *et al.*, 1998).

Dinku *et al.* (2002) developed an algorithm to attempt to correct for partial and complete beam blockage. The initial step of the algorithm is to account for attenuation of the radar beam by applying an appropriate correction factor. Partial beam blockage is addressed by determining the portion of the beam that is blocked and using the possibly unrealistic assumption that scattering would be uniform through the entirety of the beam. The algorithm then transforms the data from a polar grid relative to the radar location to a Cartesian grid. A correction factor is computed for points where beam blockage is occurring based on a vertical reflectivity profile computed using nearby points where beam blockage is not occurring. Additional processing is performed following the corrections for beam attenuation and blockage in the algorithm described.

In addition to other methods for attempting to compensate beam blockage such as the use of satellite data, work has also been done to adopt different scanning strategies to detect precipitation. Brown *et al.* (2002) developed a scanning strategy for the Missoula, Montana (KMSX) WSR-88D radar, which is located on a mountain. Because valleys receive poor coverage when using a typical scanning strategy, a customized scanning strategy was developed. The volume coverage pattern would scan at lower angles than 0.5°, which is the lowest tilt in a typical scanning strategy. The volume coverage pattern included negative tilts to detect echoes in valleys.

Appendix C. Interpolation Schemes

Although there are multiple methods to downsample or upsample gridded data, variations of interpolation schemes are not of interest to this study. However, a variety of methods exist to interpolate between irregularly spaced data points such as rain gage networks to produce gridded output. A number of methods were used to interpolate rain gage data including kriging, inverse distance weighting (IDW), natural neighbor interpolation, and spline interpolation.

Kriging and IDW are similar in that they estimate a value at each grid point by averaging neighboring grid points based on a weighting function. IDW weights observed values based entirely on their distance from the grid point assigning less weight to more distant observations. Instead of using all available observations, a limit may be placed to only consider observations within a set distance of a grid point or to only consider a set number of observations. IDW produces a deterministic solution and grid values may not match observed values. Additionally, IDW constrains the interpolated values to within the range of observed values.

Kriging uses a semivariogram to calculate the spatial variability of the data that are being interpolated. In the semivariogram, variance of data increases until the sill is reached, at which point the variance stops increasing. The semivariogram is then used to interpolate data between points. Kriging is often known as optimal interpolation. Parameters such as distance from data points at which the sill begins is often determined empirically. In addition to interpolating the data, kriging also produces an output variance field, which is a measure of the quality of the interpolation.

Another interpolation scheme of interest is spline interpolation. Unlike predicted grid point values computed through IDW and kriging, spline interpolated values match actual observed values. Splines are created over small areas and joined together to produce a continuous smooth surface. Like IDW, spline interpolation produces a deterministic solution. However, unlike IDW, spline interpolated values may be outside the range of observed values. In addition to computing a field with interpolated values of the data, a field expressing the maximum error of the interpolation can also be computed.

The natural neighbor interpolation scheme is based off Thiessen polygons and begins by computing Thiessen polygons for the observed values. Then Thiessen polygons are compoted with the observed values and the grid point. The polygon for the computed grid point is overlaid with the original polygons and observations are weighted based on the portion of the polygon area within each of the original polygons. Maxima and minima are only located at observations and grid points do match observed values. The interpolated values are constrained to the range of observed values. Natural neighbor interpolation produces a deterministic solution.

Each of these interpolation schemes produces different grid point values and the output may be very different depending on the data values and spatial distribution of observations. It is unclear which interpolation scheme provides the best estimate of the spatial distribution of rainfall. However, for the purposes of this work, kriging was chosen for interpolating the data.

Appendix D. Radar Imagery from Cases

Radar imagery from the eight cases observed by the USDA-ARS network are shown here in this appendix. The purpose of this is to provide the reader with a greater familiarity of the events. Brief meteorological descriptions of the cases are provided in Section 3.4. Images are selected from the middle of an event. For example, a rainfall event beginning at 10 UTC and lasting until 11 UTC will have an image from 1030 UTC.

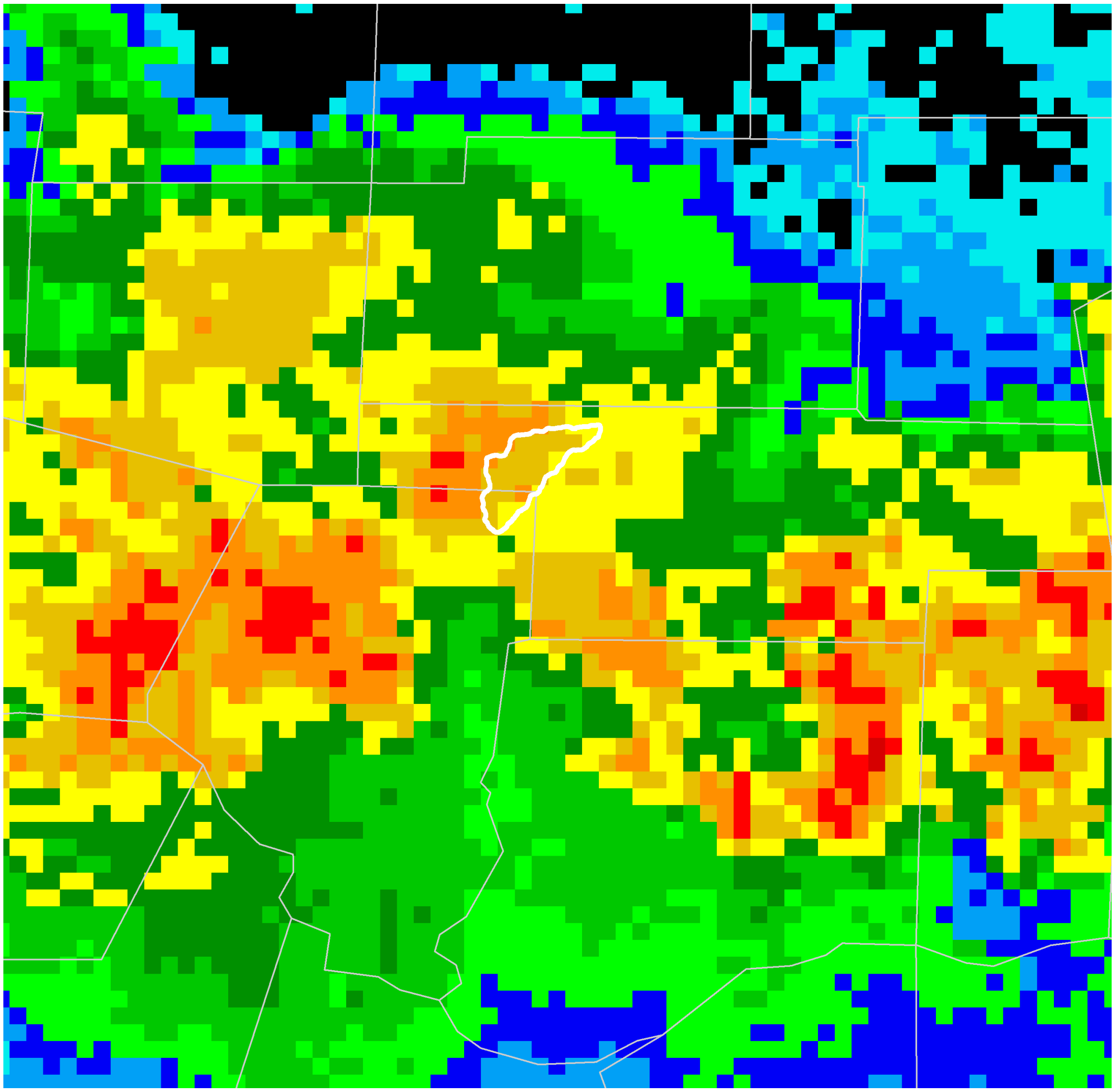

Figure D.1: A radar image during the May 19, 2004 at 07 UTC event is shown. The Goodwater Creek catchment is outlined in white and county boundaries are outlined in gray.

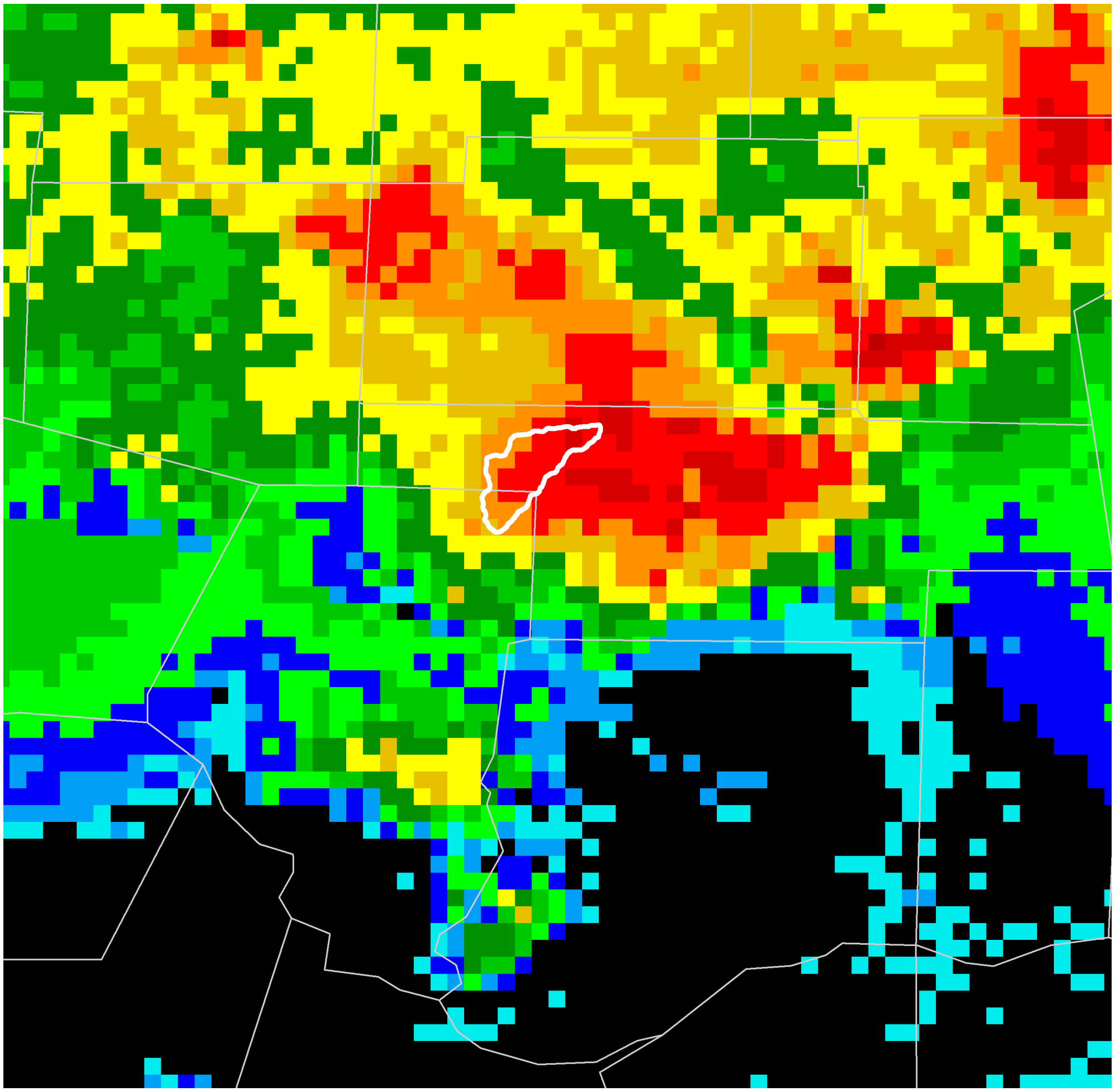

Figure D.2: A radar image during the July 6, 2004 at 13 UTC event is shown. The Goodwater Creek catchment is outlined in white and county boundaries are outlined in gray.

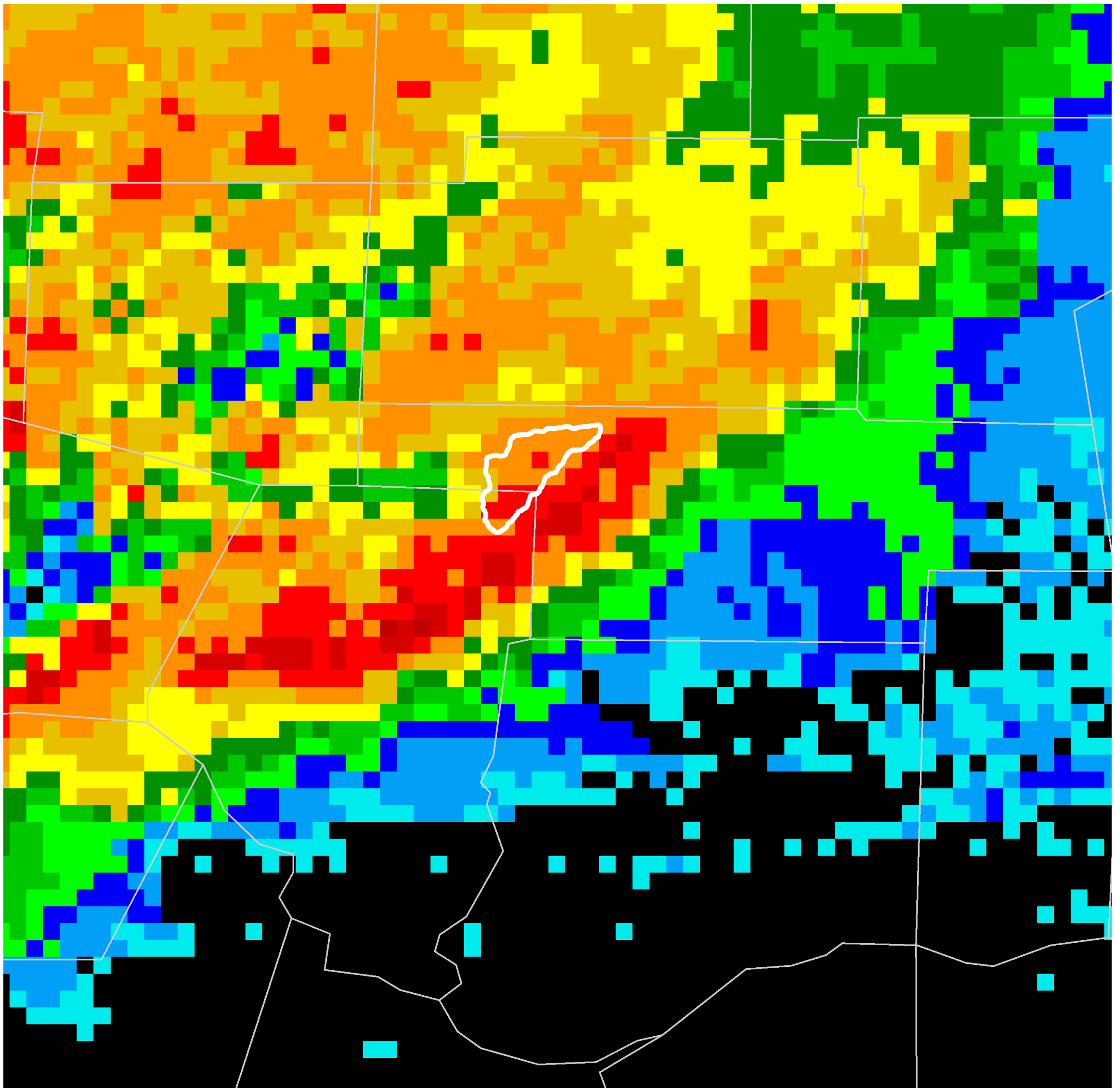

Figure D.3: A radar image during the August 4, 2004 at 08 UTC event is shown. The Goodwater Creek catchment is outlined in white and county boundaries are outlined in gray.

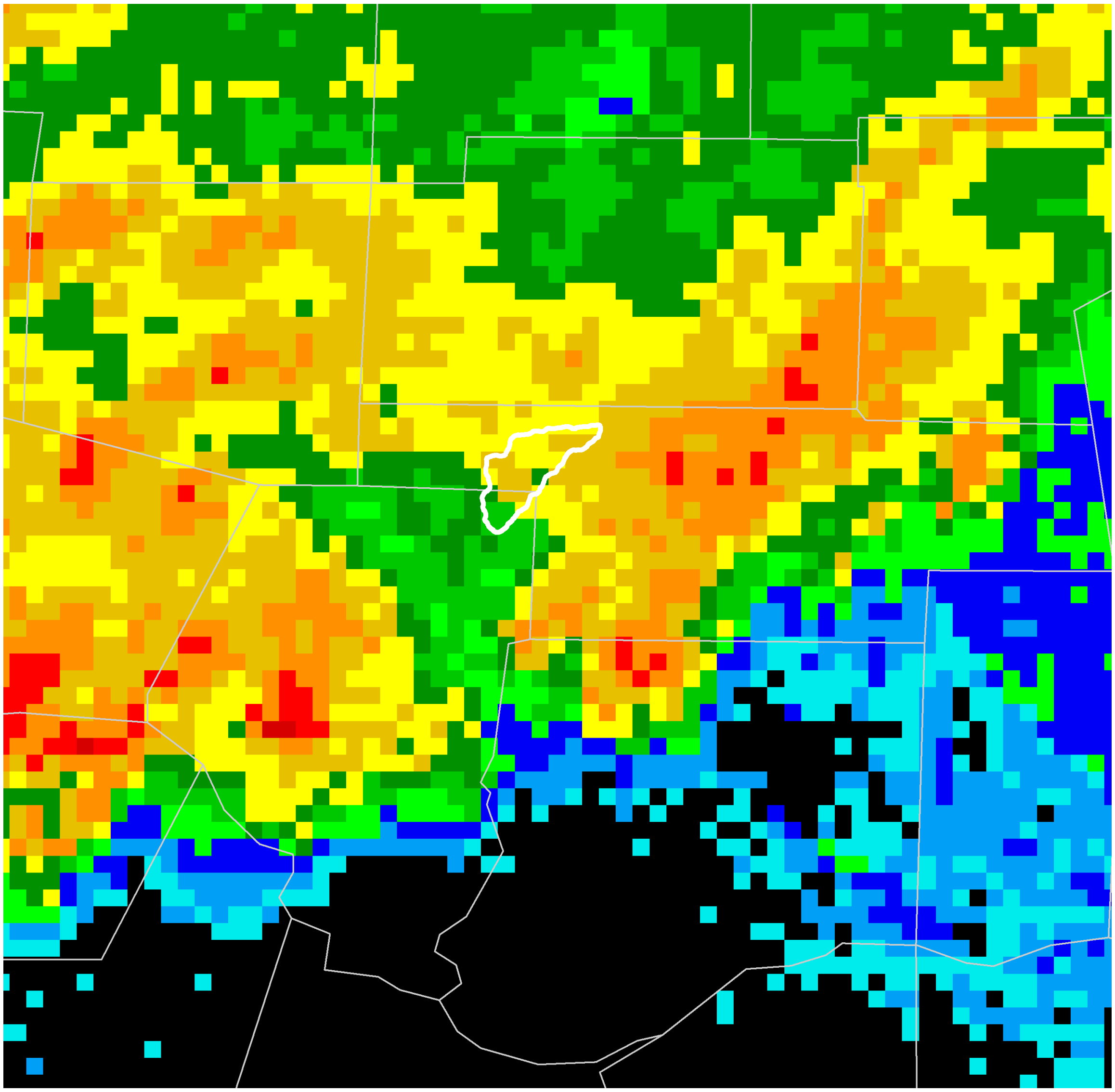

Figure D.4: A radar image during the August 4, 2004 at 09 UTC event is shown. The Goodwater Creek catchment is outlined in white and county boundaries are outlined in gray.

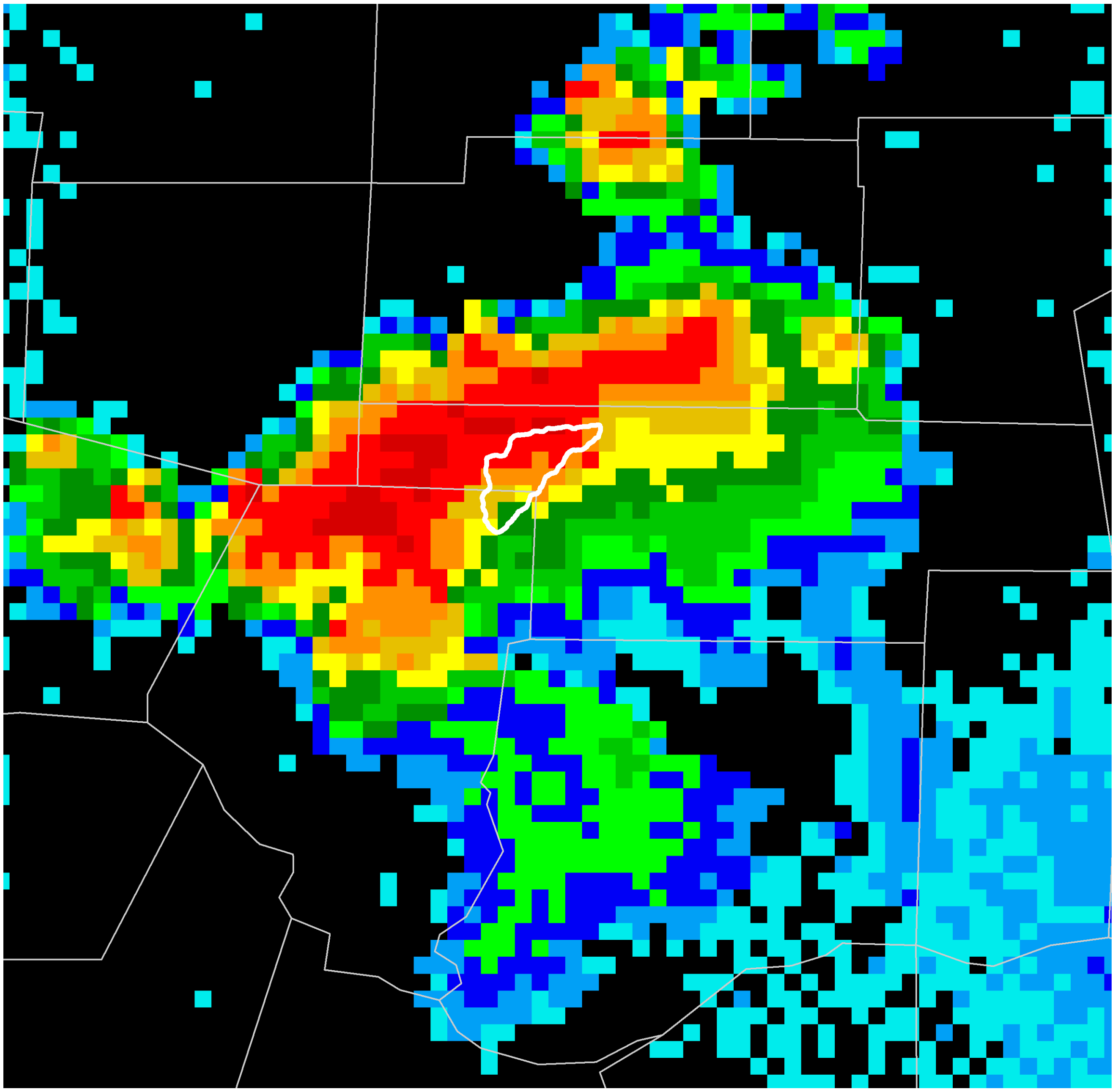

Figure D.5: A radar image during the August 26, 2004 at 06 UTC event is shown. The Goodwater Creek catchment is outlined in white and county boundaries are outlined in gray.

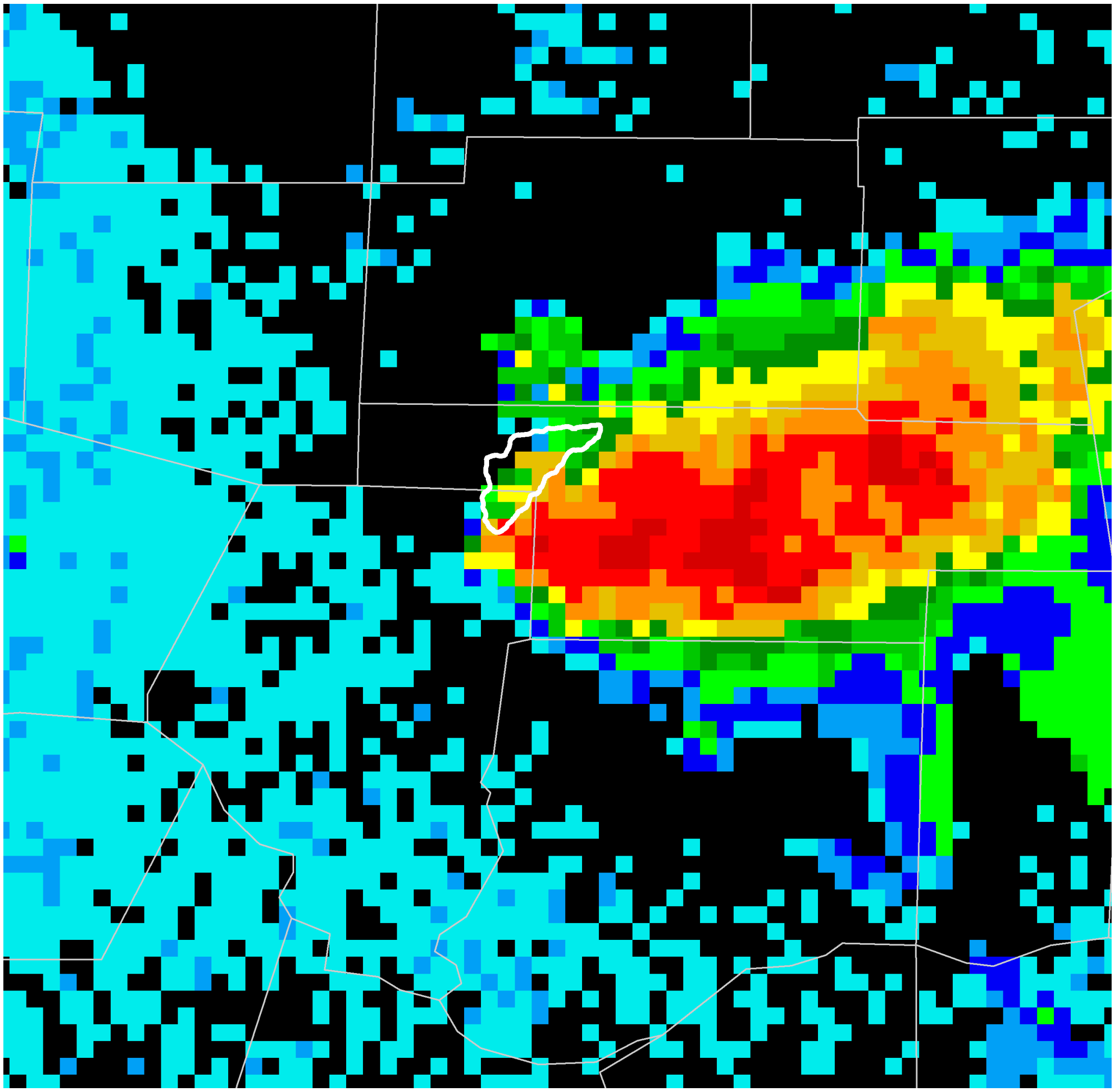

Figure D.6: A radar image during the August 26, 2004 at 07 UTC event is shown. The Goodwater Creek catchment is outlined in white and county boundaries are outlined in gray.

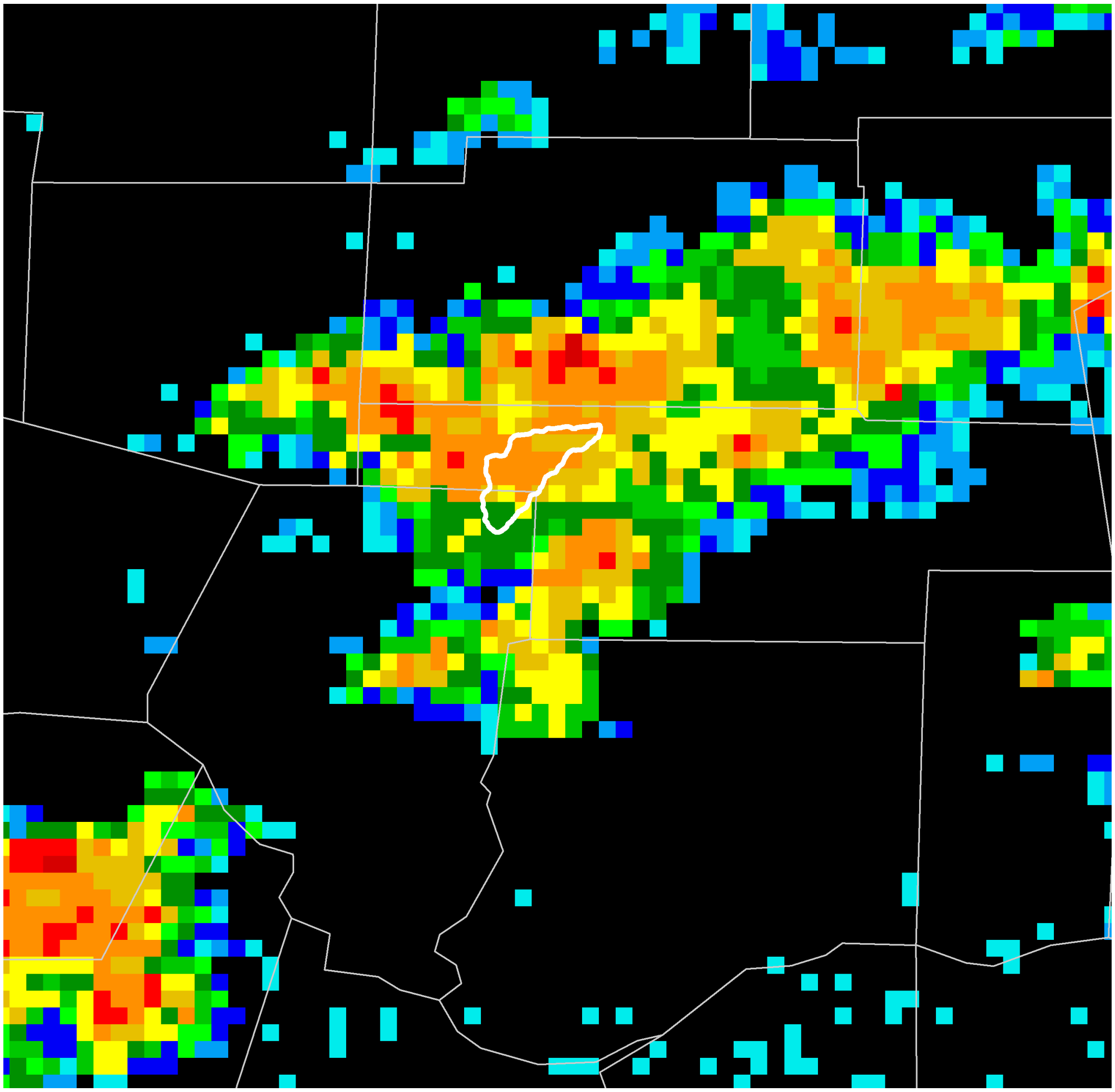

Figure D.7: A radar image during the August 27, 2004 at 18 UTC event is shown. The Goodwater Creek catchment is outlined in white and county boundaries are outlined in gray.

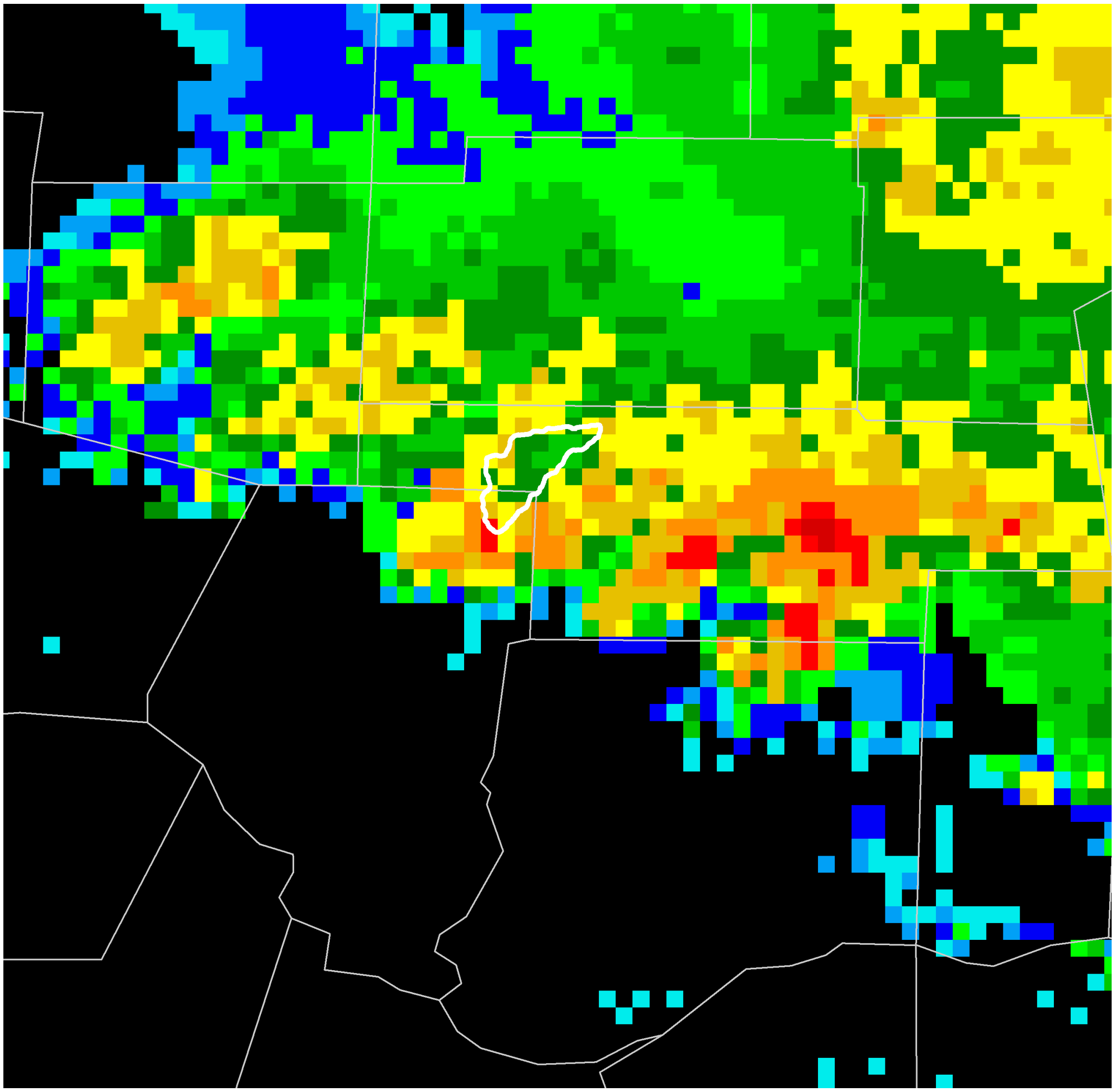

Figure D.8: A radar image during the October 18, 2004 at 10 UTC is shown. The Goodwater Creek catchment is outlined in white and county boundaries are outlined in gray.

Appendix E. Fourier Transform Math

The Fourier Transform (FT) decomposes a signal that is the result of adding together many signals of different frequencies that maintain their power throughout the duration of the signal. Each component signal is a wave and the original signal is the result of constructive and destructive interference. The original signal can be reconstructed through the Inverse Fourier Transform (IFT).

There are multiple forms of the FT and many algorithms exist for performing the FT. One important distinction is between the Continuous Fourier Transform (CFT) and the Discrete Fourier Transform (DFT). The CFT operates on a continuous signal and wave numbers of component signals need not be discrete. The DFT, however, operates on a signal that is sampled periodically and component signals have discrete wave numbers. Algorithms have been devised for reducing the complexity involved in calculating the DFT. One notable algorithm is the Fast Fourier Transform (FFT) because it is much faster than other algorithms at computing the FT over large domains.

The FT transforms a signal from the spatial domain to the frequency domain. The domain may be of more than one dimension. Some image processing and compression algorithms rely on the FFT and similar algorithms and work in two dimensions. The transformation is from (x,y) coordinates to (u,v) coordinates where x and y are coordinates in space and u and v are wave numbers.

One important property between the spatial and frequency domains is the relationship between multiplication and convolution. Multiplication in the spatial domain is equivalent to convolution in the frequency domain. Multiplication in the frequency domain is equivalent to convolution in the spatial domain. This property is known as the Convolution Theorem. Some operations, including some forms of filtering, can be easily implemented using multiplication in the frequency domain but may not be easily implemented using convolution in the spatial domain.

In the context of this discussion about the FT, f(x) and f(x,y) refer to functions in the spatial domain. The notations F(u) and F(u,v) are the result of performing the FT on the functions, respectively, and are in the spatial domain. Additionally, (x) and (x,y) are coordinates within the spatial domain. However, (u) and (u,v) are coordinates within the frequency domain and represent wave numbers.

Forms of the CFT and inverse CFT (ICFT) can be derived from simple equations to demonstrate how they are typically computed and how they contain wave equations. For the following equations, f(x) represents the signal within the spatial domain at position x. Also, F(u) represents the power within the frequency domain of wave number u.

The derivation of the CFT and ICFT will then be applied to discrete forms of the FT and IFT.

The CFT in a single dimension can be represented as the exponential function shown in equation (E.1). Although this is mathematically correct, it is not particularly instructive as to the implementation or behavior of the transform.

$$F(u)=\int_{-\infty}^{\infty} f(x)\,\mathrm{e}^{-2\mathrm{j}\pi ux}\,dx \qquad \text{(E.1)}$$

In the equation, j is used to represent an imaginary number. By using Euler's Formula, as shown in equation (E.2), it is possible to simplify equation (E.1) to a form that includes sinusoidal functions instead of an exponential function and is shown in equation (E.3).

$$\mathrm{e}^{j\theta}=\cos(\theta)+jsin(\theta) \qquad \text{(E.2)}$$

$$F(u)=\int_{-\infty}^{\infty} f(x)\left[\cos(-2\pi ux)+jsin(-2\pi ux)\right]dx \qquad \text{(E.3)}$$

Additional simplification may be performed using the knowledge that cosine is an even function and sine is an odd function. These simplifications can be expressed in equations (E.4) and (E.5), respectively. The resulting equation, when substituting into (E.3) is shown in equation (E.6), which is a typical form for the CFT.

$$\cos(-\theta)=\cos(\theta) \qquad \text{(E.4)}$$

$$\sin(-\theta)=-\sin(\theta) \qquad \text{(E.5)}$$

$$F(u)=\int_{-\infty}^{\infty} f(x)\left[\cos(2\pi ux)-jsin(2\pi ux)\right]dx \tag{E.6}$$

Equation (E.7) is a form of the one-dimensional ICFT, which can be simplified in a similar method to the CFT simplification. After simplifying the equation, a typical form of the ICFT is expressed in equation (E.8).

$$f(x)=\int_{-\infty}^{\infty} F(u)\,\mathrm{e}^{2\mathrm{j}\pi ux}\,du \tag{E.7}$$

$$f(x)=\int_{-\infty}^{\infty} F(u)\left[\cos(2\pi ux)+jsin(2\pi ux)\right]du \tag{E.8}$$

Mathematically, the ICFT and CFT are useful equations and demonstrate the properties of the FT. They are not, however, particularly practical applications of signal processing. Signals are not typically analyzed in continuous form. Instead, signals are sampled discretely to produce a representation that, if sampled frequently enough, may resemble the structure of the original signal. For discretely sampled signals, the DFT and inverse DFT (IDFT) are used. The equations are similar in nature to those used for the CFT and ICFT. When representing equations for the DFT and IDFT, M is used to represent the number of samples in a discretely sampled one dimensional signal. The signal begins at position 0 and ends at position M-1. For a two dimensional signal, N is used to represent the number of samples in the other direction. The signal begins at position 0 and ends at position N-1.

The DFT and IDFT in a single dimension can be derived in a similar way as to the CFT and ICFT. Because the steps are largely the same, only the initial equations and then the final form will be presented. The initial form of the DFT is presented in equation (E.9). Through the process of using Euler's Formula and using properties of the sine and cosine, the resulting equation in (E.10) is presented.

$$F(u)=\frac{1}{M}\sum_{x=0}^{M-1} f(x)\mathrm{e}^{\frac{-2\mathrm{j}\pi ux}{M}} \tag{E.9}$$

$$F(u)=\frac{1}{M}\sum_{x=0}^{M-1} f(x)\left[\cos\left(\frac{2\pi ux}{M}\right)-jsin\left(\frac{2\pi ux}{M}\right)\right] \tag{E.10}$$

Similarly, a typical form of the IDFT in a single dimension can be derived using the same process. The initial form of the IDFT is presented in equation (E.11). Simplification yields a more familiar form in equation (E.12).

$$f(x)=\sum_{u=0}^{M-1} F(u)\mathrm{e}^{\frac{2\mathrm{j}\pi ux}{M}} \tag{E.11}$$

$$f(x)=\sum_{u=0}^{M-1} F(u)\left[\cos\left(\frac{2\pi ux}{M}\right)+jsin\left(\frac{2\pi ux}{M}\right)\right] \tag{E.12}$$

Frequently, in computers, the pure real and pure imaginary components of a complex number may be stored separately. As a result, calculations of the pure real and pure imaginary parts of the output of the FT may be computed independently. In order to calculate this, f(x) will be split into two functions, a(x), which will be referred to as a, and b(x), which will be referred to as b. Therefore, f(x) can be defined by equation (E.13) and substituted into equation (E.10) to produce equation (E.14).

$$f(x)=a+bj \tag{E.13}$$

$$F(u)=\frac{1}{M}\sum_{x=0}^{M-1}\left[acos\left(\frac{2\pi ux}{M}\right)-ajsin\left(\frac{2\pi ux}{M}\right)+bjcos\left(\frac{2\pi ux}{M}\right)-bj^{2}\sin\left(\frac{2\pi ux}{M}\right)\right] \tag{E.14}$$

By simplifying equation (E.14), it is easy to split the equation into pure real and pure imaginary parts. Equation (E.15) is the pure real form of the FT and (E.16) is the pure imaginary part of the FT. Equivalent steps can be performed on the IDFT from equation (E.12) and substituting equation (E.17) to produce the pure real part of the IDFT in equation (E.18) and the pure imaginary part of the IDFT in equation (E.19).

$$F_{r}(u)=\frac{1}{M}\sum_{x=0}^{M-1}\left[acos\left(\frac{2\pi ux}{M}\right)+bsin\left(\frac{2\pi ux}{M}\right)\right] \tag{E.15}$$

$$F_{i}(u)=\frac{1}{M}\sum_{x=0}^{M-1}\left[-ajsin\left(\frac{2\pi ux}{M}\right)+bjcos\left(\frac{2\pi ux}{M}\right)\right] \tag{E.16}$$

$$F(u)=a+bj \tag{E.17}$$

$$f_{r}(x)=\sum_{u=0}^{M-1}\left[acos\left(\frac{2\pi ux}{M}\right)-bsin\left(\frac{2\pi ux}{M}\right)\right] \tag{E.18}$$

$$f_i(x)=\sum_{u=0}^{M-1}\left[ajsin\left(\frac{2\pi ux}{M}\right)+bjcos\left(\frac{2\pi ux}{M}\right)\right] \tag{E.19}$$

For image processing, typically the FT is evaluated in two dimensions. The equations for the DFT and IDFT will be shown after being split into pure real and pure imaginary parts. The equations are very similar in nature to those of the DFT and IDFT in one dimension with only very minor modifications. The pure real and pure imaginary parts of the DFT are shown in equations (E.20) and (E.21) respectively. For the IDFT, pure real and pure imaginary parts are shown in equations (E.22) and (E.23).

$$F_r(u,v)=\frac{1}{MN}\sum_{x=0}^{M-1}\sum_{y=0}^{N-1}\left[acos\left(2\pi\left(\frac{ux}{M}+\frac{vy}{N}\right)\right)+bsin\left(2\pi\left(\frac{ux}{M}+\frac{vy}{N}\right)\right)\right] \tag{E.20}$$

$$F_i(u,v)=\frac{1}{MN}\sum_{x=0}^{M-1}\sum_{y=0}^{N-1}\left[-ajsin\left(2\pi\left(\frac{ux}{M}+\frac{vy}{N}\right)\right)+bjcos\left(2\pi\left(\frac{ux}{M}+\frac{vy}{N}\right)\right)\right] \tag{E.21}$$

$$f_r(x,y)=\sum_{u=0}^{M-1}\sum_{v=0}^{N-1}\left[acos\left(2\pi\left(\frac{ux}{M}+\frac{vy}{N}\right)\right)-bsin\left(2\pi\left(\frac{ux}{M}+\frac{vy}{N}\right)\right)\right] \tag{E.22}$$

$$f_i(x,y)=\sum_{u=0}^{M-1}\sum_{v=0}^{N-1}\left[ajsin\left(2\pi\left(\frac{ux}{M}+\frac{vy}{N}\right)\right)+bjcos\left(2\pi\left(\frac{ux}{M}+\frac{vy}{N}\right)\right)\right] \tag{E.23}$$

Although derivations for many of these equations are not explicitly presented here, they are very similar to the derivations that have been performed earlier in this chapter. The output of the FT is complex and any processing should be performed on both the pure real and pure imaginary components of the output. As the above equations show, both the real and imaginary components of the output of the FT are necessary to properly recombine the signal into the spatial domain using the IFT. When recombining an image into the spatial domain, it is only necessary to use equation (E.22). It is not necessary to use equation (E.23) and recombine the imaginary portion of the signal.

Appendix F. Spectral Analysis Algorithm

This appendix contains a detailed description of the algorithm used for spectral analysis. It was originally submitted to the 88th Annual Meeting of the American Meteorological Society and the relevant details contained within have not been modified since.

J2.4 AN AUTOMATED METHOD FOR DETECTING PRECIPITATION AND CELL TYPE FROM RADAR PRODUCTS

George L. Limpert[1], Steven A. Lack[2], Neil I. Fox[1], and E. John Sadler[3]

University of Missouri-Columbia, Columbia, Missouri[1]
NOAA/ESRL/GSD/CIRES University of Colorado, Boulder, Colorado[2]
USDA-ARS Cropping Systems and Water Quality Research Unit, Columbia, Missouri[3]

1. INTRODUCTION

It is of interest for many purposes, including nowcasting, to evaluate the structure of radar images in an effort to produce more accurate estimates of rainfall totals from radar data. Although subjective analysis can reliably determine the structure of radar imagery, computational techniques exist to analyze a radar image using algorithms that can be automated. Many of these techniques use some form of multiresolution analysis or Fourier analysis to accomplish structure identification.

One method of identifying structures of differing sizes and scales within an image is to use high, low, and band pass filters to highlight features of interest. This is frequently accomplished by decomposing an image into the frequency domain using a transform and performing the filtering operation within the frequency domain. A variety of transforms exist for accomplishing this including the Wavelet Transform (WT) and many transforms related to the Fourier Transform (FT).

An algorithm, based on the FT and Gaussian filters, has been developed to analyze a radar image and identify structures within the image. A variety of cases are then presented to demonstrate the performance and robustness of this algorithm. Primarily this algorithm delineates regions of convective and stratiform precipitation and identifies convective structures on multiple scales. Properties of convective features are also determined by the algorithm including finding a centroid and attempting to fit an ellipse to define the structure. Additional properties of convective features are determined within the classification scheme.

2. FOURIER TRANSFORM

The FT decomposes a signal in the spatial domain into a linear combination of sinusoidal orthonormal basis functions, which are represented in the frequency domain. Mathematically, the Continuous Fourier Transform (CFT) can be expressed in a single dimension as (1),

$$F(u) = \int_{-\infty}^{\infty} f(x) e^{-2\pi i u x} dx \qquad (1)$$

which produces sinusoidal waves as shown by Euler's Formula. A corresponding similar equation, the Inverse Fourier Transform (IFT), exists to recompose the signal from the frequency domain into the spatial domain.

There are a number of implicit assumptions of the FT. These include that the signal is periodic and the pattern observed in the spatial domain is due entirely to patterns of constructive and destructive interference. That is to say that the power of a given frequency remains constant throughout the entire domain. Although these assumptions may not be realistic, the FT is still suitable for analyzing a signal.

When computing the FT, a signal is sampled at discrete intervals, and a similar pair of equations known as the Discrete Fourier Transform (DFT) and Inverse Discrete Fourier Transform (IDFT) are used. If computed by solving the equation for each (u), or (u,v) if in two dimensions, the computation will be of $O(n^2)$, which may not be feasible for large domains. Instead, the FT is calculated using the Fast Fourier Transform (FFT), which is of the complexity $O(n \log n)$, and can be computed more readily even when the domain is large.

The FT, along with similar transforms, can be used in multiple dimensions. The FT, and other related transforms, can be used for image processing and compression applications. The signal is decomposed into a linear combination of orthonormal basis images.

---

* *Corresponding Author Address:* George L. Limpert, 302 ABNR Bldg., Univ. of Missouri-Columbia, Dept. of Soil, Environmental, and Atmospheric Science, Columbia, MO, 65211; E-mail: gll883@mizzou.edu

One important property in Fourier analysis and synthesis is the Convolution Theorem. The theorem states that convolution and multiplication are related between the spatial domain and frequency domain. Convolution in one domain corresponds to multiplication in the other domain.

3. SIGNAL FILTERING

Although many filters exist for filtering signals, including ideal filters and Butterworth filters, the research herein will focus on Gaussian filters. In this context, filtering refers to attenuating or boosting a component of a signal based on the frequency of the component. As it might appear, this can be accomplished through multiplication in the frequency domain. By the Convolution Theorem, filtering would be accomplished in the spatial domain through convolution.

A low pass filter attenuates high frequency components of a signal while retaining lower frequency components. In two dimensions, the Gaussian function is given by (2),

$$G(u,v)=\frac{1}{2\pi\sigma^2}e^{-\frac{u^2+v^2}{2\sigma^2}} \qquad (2)$$

and is multiplied by the signal in the frequency domain to perform a Gaussian filtering operation. A high pass filter attenuates low frequency components of a signal and retains the higher frequency components. The portion of a signal attenuated by a low pass filter is the same as the portion of a signal retained by a high pass filter. A band pass filter retains components within a range of frequencies while attenuating signals with frequencies above and below the range. This can be performed through a low pass filter to remove signals below the low cutoff frequency followed by a high pass filter to remove signals above the high cutoff frequency.

4. SPATIAL ANALYSIS OF PRECIPITATION

Previous work has been done in analyzing the spatial characteristics of rainfall. Much of this work has been done for the purposes of developing nowcasting systems. Some nowcasting systems decompose an image into various spatial scales using the FT with the purpose of advecting or evolving features of different scales at least partially independent of other scales.

Seed (2003) devised the Spectral Prognosis (S-PROG) nowcasting scheme which uses the FT and band pass filtering to produce pseudo-reflectivity radar images. In this scheme, the FT decomposes a radar image into the frequency domain and the image is then filtered in the frequency domain into multiple scales using a Gaussian band pass filter. In addition to forecasting based on advection, high frequency features are attenuated more rapidly than low frequency features because high frequency features are more transient and therefore are less predictable.

Precipitation systems can be classified based on reflectivity gradients. Klazura et al. (1999) characterized precipitation systems into four categories based on the temporal evolution of the systems and horizontal gradients in reflectivity within the systems. The categories were systems that had high reflectivity gradients, systems that began with high reflectivity gradients and transitioned to lower reflectivity gradients through the life of the system, systems with high reflectivity gradients embedded within lower reflectivity gradients, and systems with low reflectivity gradients. Systems with high reflectivity gradients were noted to have small cores with reflectivity power of 40 to 60 dBZ with high reflectivity gradients around the core. In systems with lower reflectivity gradients, weaker reflectivity power of 25 to 40 dBZ was noted over a more widespread area.

Hagelberg and Helland (1995) used a variation of the Morlet Wavelet in two dimensions to detect radar thinlines. The wavelet function is symmetric and directionally selective. Application of the wavelet at different directions and scales was done. Areas where strong power is present in the output of the transform suggest the presence of a possible thinline. The WT is similar in nature to the FT in that it decomposes an image in the spatial domain into frequency bands. However, unlike the FT, the power in a given frequency is not fixed across the entire domain. Power can be localized in portions of the domain in a frequency band. Multiscale analysis can be accomplished by either downsampling the image or by scaling the wavelet function. Wavelets may also be useful to analyze radial velocity images for tornado vortex signatures (Liu et al. 2007) and to analyze oceanic velocity data derived from sea surface height maps for vortexes (Turiel et al. 2007).

5. METHODOLOGY

Several cases have been chosen to demonstrate the performance of the algorithm under a variety of conditions. These cases are examined using subjective analysis and then are processed using the algorithm to objectively analyze the image. The algorithm used relies only on radar-derived products with no knowledge of the environmental conditions producing the structures observed by radar. Although using additional data such as model derived parameters may provide for a better interpretation, whether subjective or automated, only radar-derived products are used for demonstrating the concept.

A primary use of the algorithm is to distinguish convective and stratiform precipitation. Cases of pure stratiform precipitation, pure convective precipitation, and stratiform precipitation with convective elements are chosen. In cases with convective precipitation, it is useful to identify structures within the image of different scales. For example, individual cells may be embedded within a larger complex, such as individual thunderstorm cells within a squall line. However, there are also cases with scattered or isolated thunderstorm activity in which individual cells are not contained within larger complexes. To test the performance of the algorithm, cases with isolated cells and with thunderstorm complexes are chosen as well.

Algorithms within the Warning Decision Support System – Integrated Information (WDSS-II) software (Lakshmanan et al. 2007) are used to prepare radar data for use within the algorithm. The ldm2netcdf algorithm is used to ingest level II data and convert it to the Network Common Data Form (NetCDF) format. The w2merger algorithm (Lakshmanan et al. 2006) is used to produce a latitude-longitude-height grid from the radar data, which is on a polar grid. Data from a single radar is used to generate the grid, which has a grid point spacing of 1 km horizontally and vertically, a size of 256 km by 256 km horizontally, and is centered on the radar site. Reflectivity at an elevation of 3 km is used in the algorithm because lower elevations have missing data at the edges of the grid.

6. ALGORITHM DESCRIPTION

The crux of the classification scheme involves decomposing a radar image to identify structures of different scales within the image. This is accomplished through the DFT, applying various Gaussian low pass, band pass, and high pass filters within the frequency domain, and recomposing the filtered images into the spatial domain. Examining the filtered images yields information about how much power is within an image at each point within the selected frequency band.

Identification of convective and stratiform structures is done independently. That is to say that a region of the image may be identified both as being convective and stratiform. This is realistic because convection is frequently embedded within larger systems that contain stratiform precipitation. Stratiform precipitation occurs on a lower frequency and may contain higher frequency signals indicating embedded convection.

6.1. Precipitation Classification

Stratiform precipitation is identified as areas that meet two criteria. The reflectivity of the original image at the point identified must be at or above 10 dBZ. At least 5 dBZ must be concentrated within a selected low frequency band.

Convective precipitation is also identified by two criteria. Power is determined by summing the weighted power within three frequency bands. If the power is above a certain reflectivity threshold and the reflectivity from the original image is above a threshold as well, the point is marked as convective. If reflectivity within the original image is weak, a strong signal within the bands used for identifying convection is required to mark the point as convective. Conversely, if reflectivity within the original image is strong, a weaker signal within the bands for identifying convection is required to mark the point as convective. If reflectivity in the original image exceeds the hail cap (53 dBZ in this scheme) the point is marked as convective regardless of the power within frequency bands.

To determine convection, two values are compared against a series of thresholds. One of the values, signal strength within bands used for identifying convection, is computed by weighting and summing power within three bands. Values of σ given in the equation are based on a square domain with a length of 256 km and a grid point spacing of 1 km. The first subscript is the lower cutoff frequency and the second subscript is the higher cutoff frequency of the band. This value is calculated by (3),

$$R_{bpf}(x,y)=B_{3,12}+B_{12,30}+\frac{B_{1,4}}{2} \qquad (3)$$

and is used to represent the signal in bands that would represent convection. The other value is based on reflectivity within the original image. Table 1 shows the thresholds for R_{bpf} and R used for identifying convection. If the criteria are both satisfied, the point is marked as convective.

R Threshold	**R_{bpf} Threshold**
≥ 7 dBZ	≥ 25 dBZ
≥ 16 dBZ	≥ 20 dBZ
≥ 25 dBZ	≥ 15 dBZ
≥ 34 dBZ	≥ 10 dBZ
≥ 43 dBZ	≥ 5 dBZ
≥ 53 dBZ	N/A

Table 1: *Thresholds used for identifying convection*

Additional echoes stronger than 5 dBZ that have not been identified as convective or stratiform are additionally marked. Although these echoes are not classified as precipitation, they may be useful in identifying other structures such as boundaries along which strong convergence is occurring.

An attempt is made to classify embedded convection within larger stratiform structures. Such regions must be classified both as convective and stratiform by the previous classification scheme. Additionally, criteria must be met so that ratios of power in frequency bands associated with convection compared to power in bands associated with convection is below a threshold. The purpose of this is to require that, although the region is classified as convective and stratiform, the stratiform signal is relatively strong compared to the convective signal. Without these additional criteria, it is likely that many larger convective systems would meet both the convective and stratiform requirements and would have large areas classified as embedded convection that would likely not be classified as embedded convection in a subjective analysis by a forecaster.

6.2. Structure Identification

The cluster, segment, and cell identification schemes work by identifying structures of different scales within an image. Structures of different scales may be contained within one another to represent a hierarchy of structures within a reflectivity image. That is to say a cluster may contain multiple segments, each of which may contain multiple cells. Segments are not required to be contained within clusters and cells are not required to be contained within segments or clusters. Clusters are not required to contain segments or cells and segments are not required to contain cells. Each scale is identified independently of other scales.

As with the convective and stratiform identification scheme, each cluster, segment, and cell must meet a series of criteria for that scale. Clusters, segments, and cells must consist entirely of points that have been marked as convective. Other power thresholds within frequency bands must also be satisfied to meet each classification. Cluster identification only examines power within the lowest frequency band associated with convection whereas segment and cell identification examine progressively higher frequency bands.

Upon tagging clusters, segments, and cells, additional filtering is performed to remove very small structures at each scale. To accomplish this, the image is eroded and dilated using the same mask, which can be defined separately for each scale if desired. By specifying larger masks, larger structures will be removed. This not only has the effect of removing structures that are smaller than the mask, but also of removing detail around the edges of structures.

To identify structures within a scale, the filtered image is examined for points within a structure. When a point in a structure is identified within the filtered image, a scanline fill is performed starting from the identified point, but the fill is performed within the unfiltered image. This identifies only structures present within the filtered image, however, the structures retain their shape from the unfiltered image. Small structures are removed by the filtering operation while larger structures remain unaltered by the filtering operation.

6.3. Shape Determination

A variety of metrics are computed on the clusters, segments, and cells once they have been identified. Three simple metrics computed are the area of the structure, the maximum reflectivity power within the structure, and the average reflectivity of the structure.

It is of interest to determine a centroid of a structure, which is useful in some shape analysis algorithms. The centroid is determined by computing a penalty function for every point within the structure. The point for which the penalty is lowest is determined to be the centroid. The algorithm for finding the centroid attempts to place the centroid near the spatial center of the structure but also near the core as indicated by the strongest reflectivity within the structure (reflectivity-weighted centroid). The penalty function is computed by summation of (4),

$$P(x,y)=R(x,y)\times D \quad (4)$$

where R is the reflectivity at (x,y) and D is the distance from (x,y) to the centroid for all (x,y) within the cell. The penalty function is computed for all points within the structure. The point where the penalty function is minimized is determined to be the centroid. The centroid must be within the structure, regardless of the shape of the structure. The reflectivity at the centroid of the structure is computed as another metric.

Edge detection is used within the shape analysis to approximate the shape of the structure. The best method for identifying structure edges is to consider four directions adjacent to a pixel, which are north, south, east, and west. For a point within a structure, it is on the edge of a structure if at least one of the pixels in one of the four adjacent directions directly next to the pixel is not in the structure. Also, if at least one of the four neighboring pixels is not within the domain, the pixel is considered to be at the edge of the structure. This is typically sufficient for detecting the edge of a structure. However, for the purposes of shape analysis, if any of the eight directly neighboring pixels to a pixel are not part of the structure, the pixel is considered to be an edge.

Although there are many methods for representing the shape of a structure, a simple method that is useful in shape analysis is to approximate the structure as an ellipse. An ellipse can be represented by a center point, major axis, and minor axis.

From the centroid, the distance to each point that is considered to be an edge is computed. The line through the centroid to the most distant edge point from the centroid is considered to be the major axis of the ellipse. From the centroid, the most distant edge point perpendicular to the major axis is considered to be the minor axis of the ellipse. By adding 0.5 to the length of the major axis in pixels and dividing by the length of the minor axis plus 0.5, eccentricity can be computed. It is possible, using this method of computing the shape of the cell, to have a minor axis of length zero. Depending on the shape of a cell and the position of the centroid, it is possible for the minor axis to be zero pixels in length. Division by zero when computing the eccentricity is prevented by adding 0.5 to both the length of the minor axis and the length of the major axis so that neither axis can ever have a length of zero.

7. CASES SELECTED AND RESULTS

Several cases of varying types are selected to demonstrate the robustness of the classification scheme used. Subjective analysis of each of the cases is compared with the objective analysis performed by the algorithm.

The ten cases were prepared and processed using the algorithm described previously. Each case will be discussed independently with analysis of the performance of the algorithm. In the images, each cell, segment, and cluster is uniquely colored. In images showing the classification of precipitation types, dark red indicates convection, with other colors indicating stratiform precipitation, other echoes above 5 dBZ, and no precipitation as the color scale progresses to blue.

1) KEAX at 2000 UTC on March 12, 2006

Shown in figure 1a, several supercells are evident in the image with three distinct clusters of cells. Some of the clusters contain three or four cells. In addition to the several reflectivity cores, weak echoes are noted to the east of the cores, likely associated with thunderstorm anvils.

As shown in figure 1b, the algorithm correctly identified the intense reflectivity cores as convective in nature. The structures detected by the algorithm are shown in figures 1c through 1e. There are several distinct cells in the image, which seem to correspond well to the cells identified by the algorithm. Three distinct clusters are identified by the algorithm, which seems reasonable. Even though precipitation was not occurring in the areas beneath the thunderstorm anvils, the algorithm is not provided information as to the vertical extent of the structures. Identifying those regions as stratiform precipitation is reasonable given the information provided to the algorithm. The algorithm performs well in this case both on discriminating convective and stratiform precipitation and identifying structures at multiple scales.

2) KMLB at 1100 UTC on February 2, 2007

A line of supercells is present in the image, shown in figure 2a, with additional isolated to scattered convection just ahead of the line, to the north of the line, and to the southwest of the line. Weak echoes are noted to the southeast of many of the thunderstorms, likely present as a result of thunderstorm anvils.

The convection in the image is properly classified by the algorithm in figure 2b. Figures 2c through 2e show the structures present at the spatial scales examined. Although the convective precipitation is correctly identified, it would appear that there are more cells than are identified individually by the algorithm. Several of the cells that are identified have an elongated appearance, which is due to the presence of multiple cells located adjacent to one another that are being identified as a single cell. Although one of the clusters identified appears too small to actually qualify as a cluster, three other distinct clusters of cells apparent in the radar image are correctly identified by the algorithm. Convective and stratiform precipitation are identified well by the algorithm. The algorithm performs moderately well at identifying features at multiple scales.

3) KILX at 2100 UTC on July 13, 2004

In figure 3a, two large clusters of thunderstorms are evident in the radar image. The northwestern cluster has several distinct reflectivity cores embedded within it. The southeastern cluster is at the edge of the domain and the structure is less clear. Scattered thunderstorm cells are also present to the northwest of the clusters and between the clusters. Weak echoes are present to the south and northeast of the clusters, likely associated with thunderstorm anvils.

The identification of convective and stratiform precipitation, shown in figure 3b, by the algorithm appears to be reasonable. Figures 3c through 3e show the structures present at the spatial scales examined. Although one of the clusters that is identified appears to be small enough to not qualify as a cluster, the other two clusters are identified correctly. The identification of convective cells within the clusters appears mostly reasonable. It is difficult to subjectively discern cells within some portions of the clusters, so it is reasonable that some portions of clusters do not have cells identified within them. Overall, the performance of identifying convective precipitation is good. However, the algorithm performs moderately well at identifying features at multiple scales.

4) KSGF at 0230 UTC on June 21, 2000

As shown in figure 4a, a line of thunderstorms with embedded cells extends across the domain oriented from the west-southwest to the east-northeast. Scattered convection is occurring to the south of the line of thunderstorms. Weaker echoes are noted to the north of the line likely due to thunderstorm anvils and stratiform precipitation.

The identification of the line of thunderstorms and isolated cells as convective with much of the precipitation to the north of the line identified as stratiform seems reasonable. Convective and stratiform areas are shown in figure 4b. Figures 4c through 4e show the structures present at the spatial scales examined. Although numerous cells are properly identified within the line, there are many more that are not identified. Identification of segments and clusters was better. However, there are clusters identified that are too small to be subjectively identified as a cluster. The algorithm performed well at identifying convective and stratiform precipitation. The performance of identifying features at multiple scales was moderately good.

5) KSGF at 2230 UTC on January 12, 2005

Figure 5a shows a broken line of thunderstorms extends across much of the domain from south-southwest to north-northeast. The thunderstorm activity is embedded within a larger region of weaker echoes likely due to thunderstorm anvils and stratiform precipitation. Some evidence of a melting layer is evident in the image. Scattered convective cells and some weaker echoes are present to the east of the line in the southern portion of the image. Additional convective cells are present in the northwest corner of the image embedded within some weaker echoes likely due to thunderstorm anvils and stratiform precipitation.

In figure 5b, he algorithm appears to identify a few regions of the image as convective that may not be convective in nature. However, regions that should be identified as convective appear to be properly identified. Figures 5c through 5e show the structures present at the spatial scales examined. There are a few cells within the image that are not identified. The algorithm appeared to perform better at identifying segments and clusters, however. The algorithm performed moderately well both at identifying convection and identifying features at multiple scales within the image.

6) KSGF at 2330 UTC on April 22, 2004

Shown in figure 6a, scattered thunderstorms are noted throughout much of the southwest and northeast corners of the image. A region of weaker reflectivity is noted extending east from two cells located in the far southwest corner of the image, likely due to thunderstorm anvils from the cells.

Although there may be a couple of false positives in identifying convection within the image, shown in figure 6b, overall the performance is quite good. Figures 6c through 6e show the structures present at the spatial scales examined. Cells within the image are mainly discrete, and the identification appears to be quite good. Because the cells are discrete but somewhat large in size, it seems reasonable that they are also identified as segments and sometimes as clusters. Both the identification of convective and stratiform precipitation and the identification of features at multiple scales appears to be quite good in this case.

7) KEAX at 0600 UTC on December 1, 2006

In figure 7a, a large region of weak echoes associated with stratiform precipitation extends over all but the far western and northwestern part of the radar image. The precipitation is mainly in the form of snow with possibly sleet and freezing rain in the southern and eastern part of the image. A band of stronger reflectivity extends east-northeast from nearly the center of the image, likely associated with a convective band of precipitation.

Figure 7b shows that the convective band in the radar image is not identified by the algorithm. Because the convective band is not identified, it is not possible to identify features within this band. A region near the edge of the image is identified as convective. This region may have been properly identified as stratiform if it was not near the edge of the domain. Figures 7c through 7e show the structures present at the spatial scales examined. Overall, the algorithm performed poorly in this case. Structure identification performed poorly in this case due to poor performance of identifying convective and stratiform precipitation. The failure to detect the convective band within the image is likely due to the weak reflectivity gradients in and around the convective band.

8) KSGF at 0200 UTC on June 14, 2005

A curved broken line of thunderstorms extends from the southwest corner to the northeast corner of the image, shown in figure 8a, with additional thunderstorms located near the center of the image. Little stratiform precipitation is observed. Weaker echoes are noted in the vicinity of reflectivity cores and are likely due to thunderstorm anvils.

The classification of convective and stratiform precipitation, shown in figure 8b, is reasonable. Figures 8c through 8e show the structures present at the spatial scales examined. Some cells that are small and close together in the image are identified as one elongated cell when they should be identified as multiple cells. However, the identification of segments and clusters within the image is reasonable. The performance of the algorithm at identifying convective and stratiform precipitation was very good. The algorithm performed moderately well at identifying features of multiple scales within the image.

9) KSGF at 0330 UTC on June 26, 2003

In figure 9a, a broken line of thunderstorms extends north and east from the southwest part of the image through the northeast part of the image. Large region of stratiform precipitation is present to the north and west of the line of thunderstorms. Some convective cells are embedded within the stratiform precipitation and possibly along the northwest edge of the stratiform precipitation.

Although it appears in figure 9b that all convective features are properly identified, some stratiform regions are also identified as convective. Figures 9c through 9e show the structures present at the spatial scales examined. Many small cells are not identified within the image. Identification of segments and clusters appears more reasonable. However, there are regions that do not appear particularly convective in nature that are identified as segments. The algorithm performed moderately well at identifying convection and stratiform precipitation. The performance of identifying features of multiple scales was moderate.

10) KSGF at 1900 UTC on December 6, 2007

Figure 10a shows a large area of stratiform precipitation is spread over almost the entire domain. The heaviest precipitation is spread over the southern portion of the domain. Much of the precipitation is frozen during this event. No convection is obvious within the domain.

As shown in figure 10b, most of the image is correctly identified as stratiform precipitation. The regions identified as convective may be false positives. Figures 10c through 10e show the structures present at the spatial scales examined. No cells are identified within the image. However, considering that the precipitation is stratiform in nature, the identification of a segment and cluster is not reasonable. The performance was moderately good at identifying convective and stratiform precipitation. Identification of structures within the image was moderately poor. Had no convection been identified, there would not be structures to the identify, and the algorithm would have exhibited better performance.

8. ANALYSIS OF RESULTS

The algorithm generally performed quite well over the selected cases in identifying convective and stratiform precipitation. Although there were a few false positives and missed regions of convection, nearly all convective and stratiform precipitation was correctly identified. In the cases where convective and stratiform precipitation did not appear to be identified correctly, the precipitation was marginally convective or stratiform. In cases of obvious convection and obvious stratiform precipitation, the algorithm performed very well.

Larger features appeared to be identified more correctly than smaller features. Although many cells were identified correctly, too few cells were identified by the algorithm. One common problem was the identification of two or more nearby cells identified as a single cell. Generally, identification of segments and clusters was done well. However, at times, features that appeared to be too small to qualify as a segment or a cluster were identified as such. The algorithm performed better in identifying larger features than it did in identifying smaller features. Discrete cells and cells within clusters that had distinct strong reflectivity cores were identified quite well.

The algorithm performance was also degraded when irregular features of a variety of spatial scales were present in the image, such as in case (8). Although the algorithm performed well under a variety of conditions, this may be a limitation of using Fourier analysis. In these cases, wavelet analysis may outperform algorithms that are based on the FT.

9. FUTURE WORK

The cell identification and classification scheme is being incorporated into a larger cell classification scheme based on cell attributes and near storm environment data (Lack and Fox 2008). When completed, the cell classification scheme will identify convective cells and calculate attributes of the convective cells to classify the cells. The cell classification can be used as part of a nowcasting scheme for the purpose of applying conceptual models to forecast cell behavior.

The identification of convective structures on multiple scales is useful in verification of output of nowcasting schemes. This algorithm delineates convective structures on three scales, which may be useful in evaluating the performance of nowcasting schemes in forecasting the evolution of structures of different scales within a radar image. The classification of precipitation type can be used to select and apply different Z-R relationships to different portions of a radar image. This may improve the estimates of rainfall accumulation. Additionally, rainfall accumulation estimates generated through this method may be useful for verifying the performance of precipitation generated within numerical models.

10. CONCLUSION

Convective and stratiform regime identification is a strength of this algorithm. Although the identification of structures within an image at multiple scales did not perform as well, the issues occurred largely when convective features were small, very closely spaced, or exhibited relatively weak reflectivity. Additionally, because of the nature of the algorithm, identification of structures within the radar image depends on the identification of convective and stratiform precipitation. Some of the failures of the structure identification scheme were caused by poorly identified convection and stratiform precipitation.

Although multiscale advection of structures within a radar image has been implemented in nowcasting schemes, use of multiscale analysis is very limited in analyzing structures within a radar image. The FT, or a similar transform, may be useful in identification and analysis of convective and stratiform structures within a radar image.

11. ACKNOWLEDGEMENTS

The authors of this paper would like to acknowledge that the USDA-ARS Cropping Systems and Water Quality Research Unit funded this research.

Additionally, the authors of this paper would like to acknowledge the following people for contributions to this research or related projects:

Dr. Wenjun Zeng
Dr. Kannappan Palaniappan
Kelly Scott
Kara Bourn

12. REFERENCES

Hagelberg, C. and J. Helland, 1995: Thin-line detection in meteorological radar images using wavelet transforms. *J. Atmos. Oceanic Technol.*, **12** (3), 633-642.

Klazura, G. E., J. M. Thomale, D. S. Kelly, and P. Jendrowski, 1999: A comparison of NEXRAD WSR-88D radar estimates of rain accumulation with gauge measurements for high- and low-reflectivity horizontal gradient precipitation events. *J. Atmos. Oceanic Technol.*, **16** (11), 1842-1850.

Lack, S. A. and N. I. Fox, 2008: An automated approach for identifying convective storm type using reflectivity and near-storm environment data. Preprints, *6th Conference on Artificial Intelligence Applications to Environmental Science*, Amer. Meteor. Soc., New Orleans, J4.3.

Lakshmanan, V., T. Smith, K. Hondl, G. J. Stumpf, and A. Witt, 2006: A real-time, three dimensional, rapidly updating, heterogeneous radar merger technique for reflectivity, velocity, and derived products. *Wea. Forecasting*, **21** (5), 802-823.

———, T. Smith, G. J. Stumpf, and K. Hondl, 2007: The warning decision support system – integrated information (WDSS-II). *Wea. Forecasting*, **22** (3), 596-612.

Liu, S., M. Xue, and Q. Xu, 2007: Using wavelet analysis to detect tornadoes from doppler radar radial-velocity observations. *J. Atmos. Oceanic Technol.*, **24** (3), 344-359.

Seed, A. W., 2003: A dynamic and spatial scaling approach to advection forecasting. *J. Appl. Meteorol.*, **42** (3), 381-388.

Turiel, A., J. Isern-Fontanet, and E. García-Ladona, 2007: Wavelet filtering to extract coherent vortices from altimetric data. *J. Atmos. Oceanic Technol.*, **24** (12), 2103-2119.

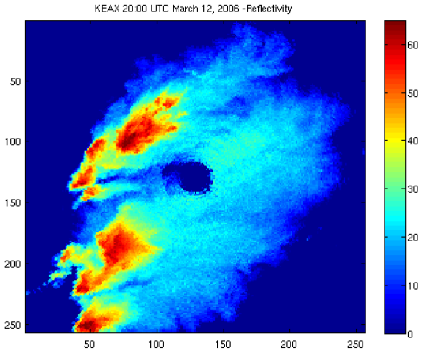

Figure 1a: *Radar reflectivity observed by KEAX at 20:00 UTC on March 12, 2006*

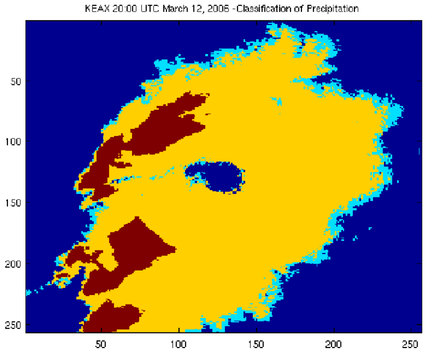

Figure 1b: *Precipitation classification for the radar image from KEAX at 20:00 UTC on March 12, 2006*

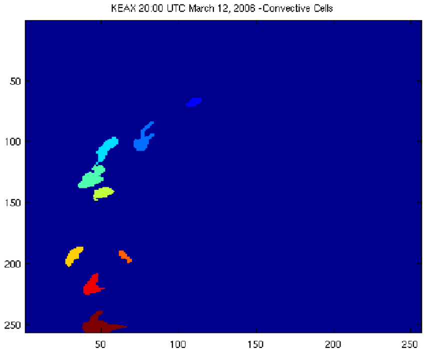

Figure 1c: *Cells identified within the radar image from KEAX at 20:00 UTC on March 12, 2006*

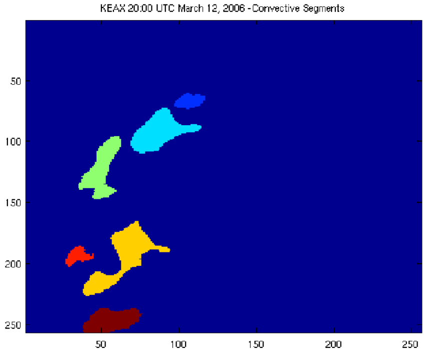

Figure 1d: *Segments identified within the radar image from KEAX at 20:00 UTC on March 12, 2006*

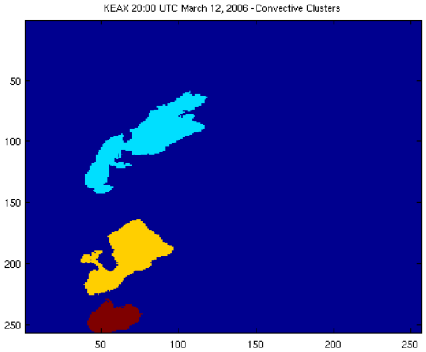

Figure 1e: *Clusters identified within the radar image from KEAX at 20:00 UTC on March 12, 2006*

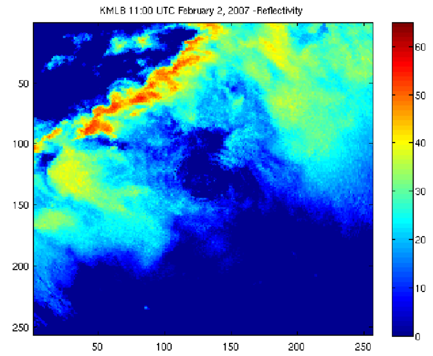

Figure 2a: Radar reflectivity observed by KMLB at 11:00 UTC on February 2, 2007

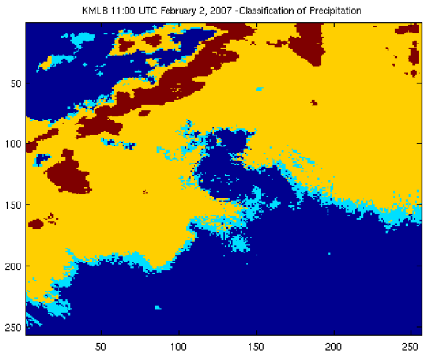

Figure 2b: Precipitation classification for the radar image from KMLB at 11:00 UTC on February 2, 2007

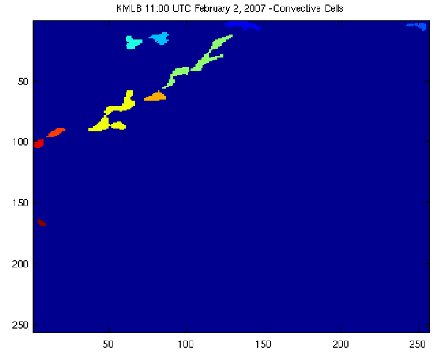

Figure 2c: Cells identified within the radar image from KMLB at 11:00 UTC on February 2, 2007

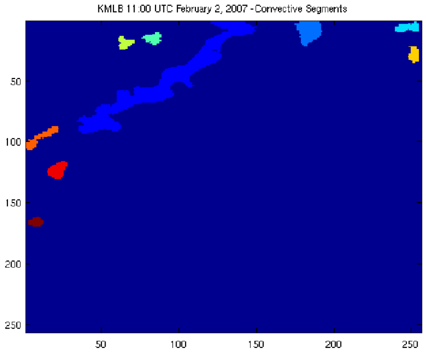

Figure 2d: Segments identified within the radar image from KMLB at 11:00 UTC on February 2, 2007

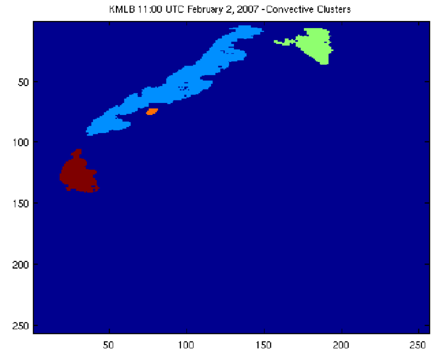

Figure 2e: Clusters identified within the radar image from KMLB at 11:00 UTC on February 2, 2007

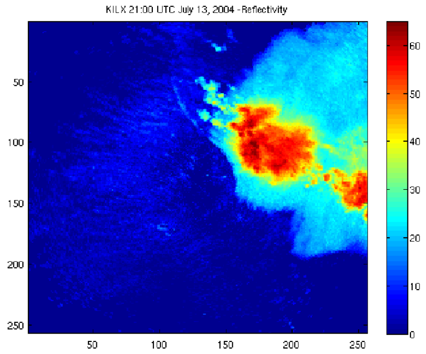

Figure 3a: *Radar reflectivity observed by KILX at 21:00 UTC on July 13, 2004*

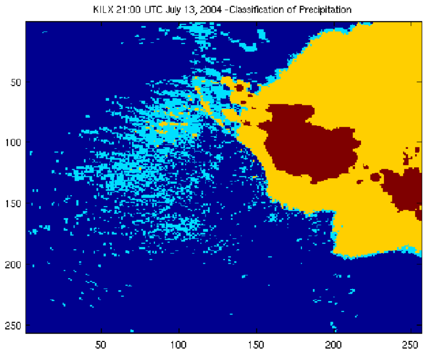

Figure 3b: *Precipitation classification for the radar image from KILX at 21:00 UTC on July 13, 2004*

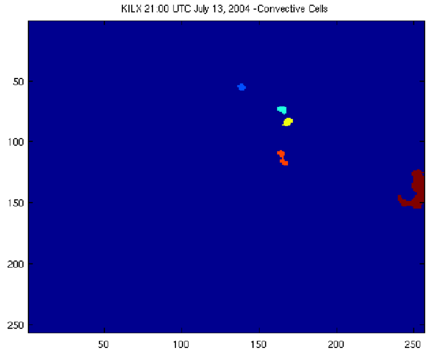

Figure 3c: *Cells identified within the radar image from KILX at 21:00 UTC on July 13, 2004*

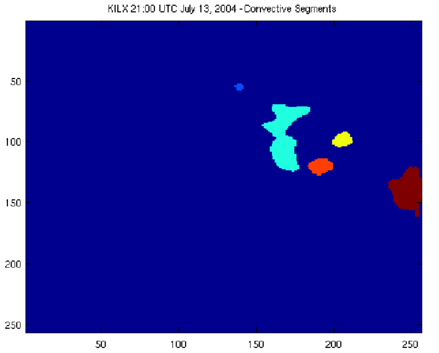

Figure 3d: *Segments identified within the radar image from KILX at 21:00 UTC on July 13, 2004*

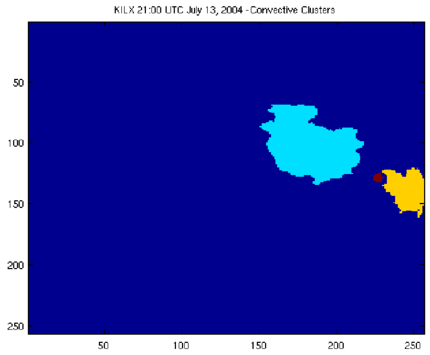

Figure 3e *Clusters identified within the radar image from KILX at 21:00 UTC on July 13, 2004*

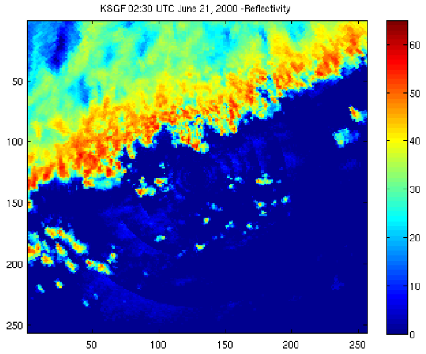

Figure 4a: *Radar reflectivity observed by KSGF at 02:30 UTC on June 21, 2000*

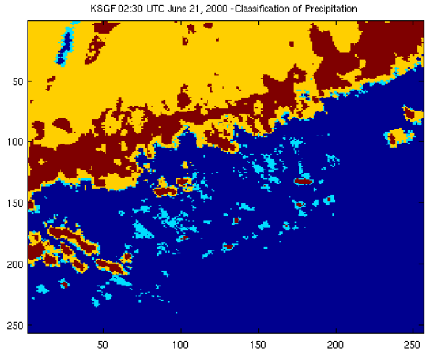

Figure 4b: *Precipitation classification for the radar image from KSGF at 02:30 UTC on June 21, 2000*

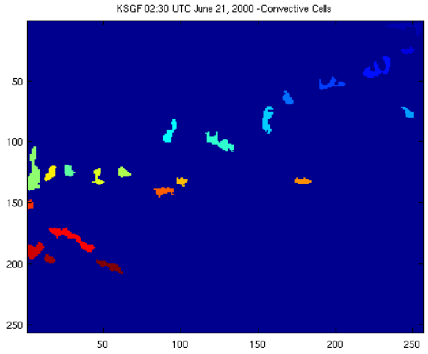

Figure 4c: *Cells identified within the radar image from KSGF at 02:30 UTC on June 21, 2000*

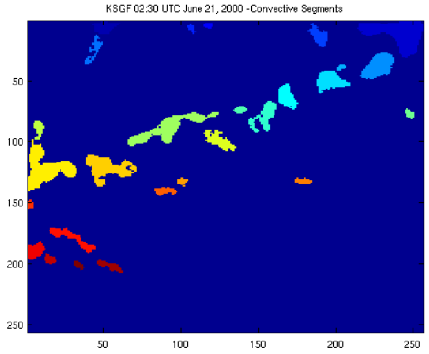

Figure 4d: *Segments identified within the radar image from KSGF at 02:30 UTC on June 21, 2000*

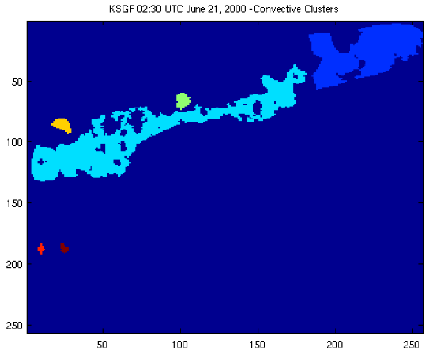

Figure 4e: *Clusters identified within the radar image from KSGF at 02:30 UTC on June 21, 2000*

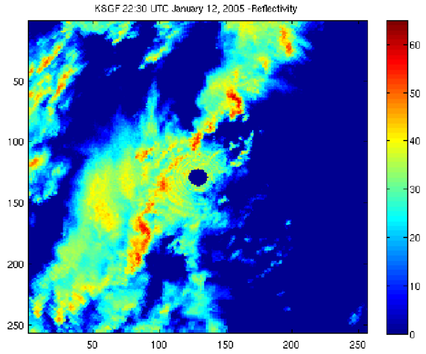

Figure 5a: *Radar reflectivity observed by KSGF at 22:30 UTC on January 12, 2005*

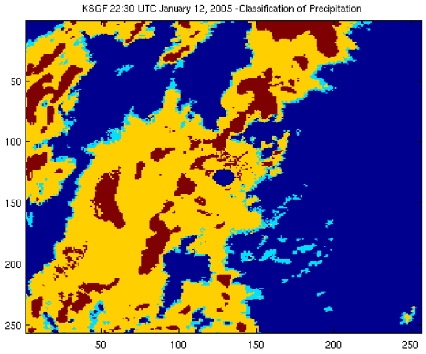

Figure 5b: *Precipitation classification for the radar image from KSGF at 22:30 UTC on January 12, 2005*

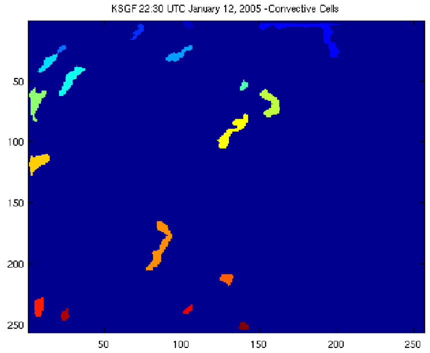

Figure 5c: *Cells identified within the radar image from KSGF at 22:30 UTC on January 12, 2005*

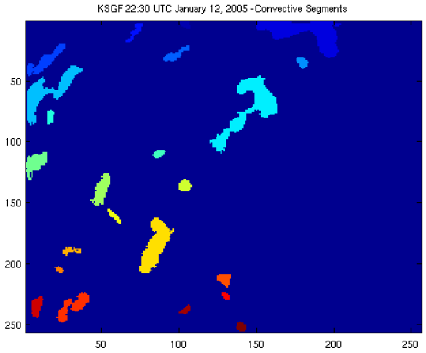

Figure 5d: *Segments identified within the radar image from KSGF at 22:30 UTC on January 12, 2005*

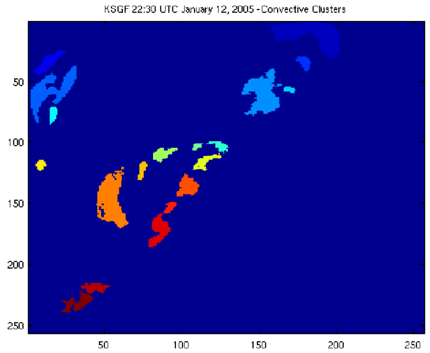

Figure 5e: *Clusters identified within the radar image from KSGF at 22:30 UTC on January 12, 2005*

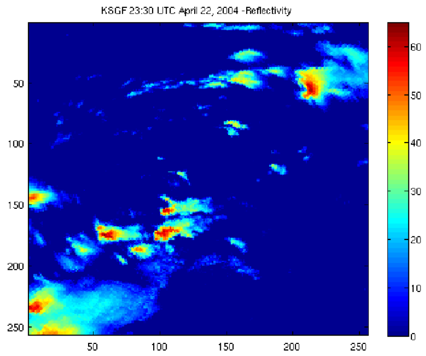

Figure 6a: *Radar reflectivity observed by KSGF at 23:30 UTC on April 22, 2004*

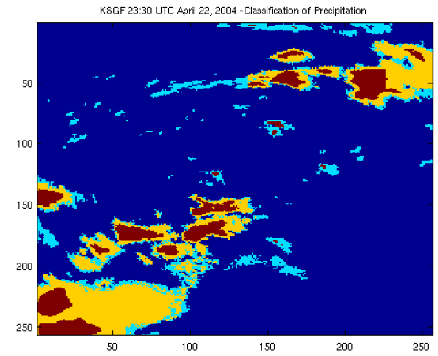

Figure 6b: *Precipitation classification for the radar image from KSGF at 23:30 UTC on April 22, 2004*

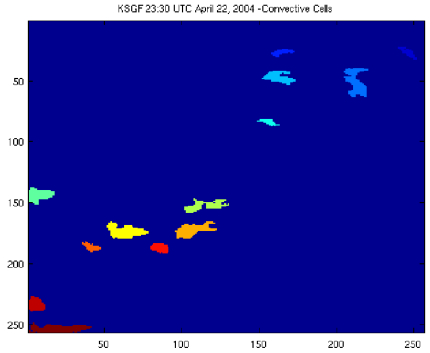

Figure 6c: *Cells identified within the radar image from KSGF at 23:30 UTC on April 22, 2004*

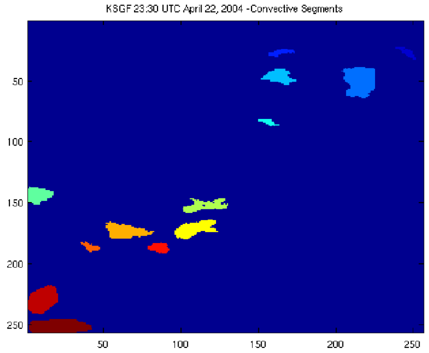

Figure 6d: *Segments identified within the radar image from KSGF at 23:30 UTC on April 22, 2004*

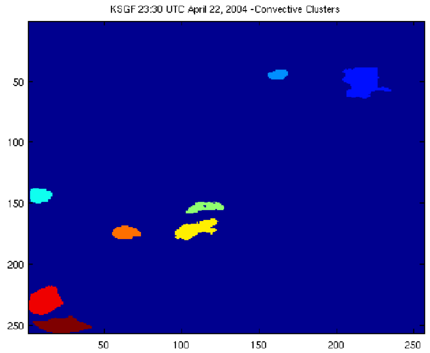

Figure 6e: *Clusters identified within the radar image from KSGF at 23:30 UTC on April 22, 2004*

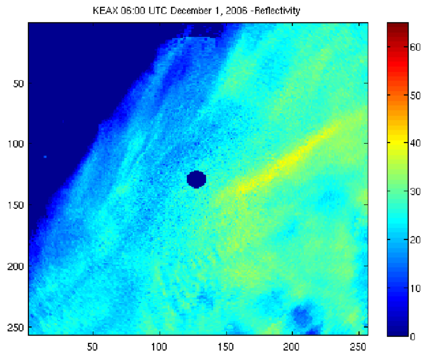

Figure 7a: *Radar reflectivity observed by KEAX at 06:00 UTC on December 1, 2006*

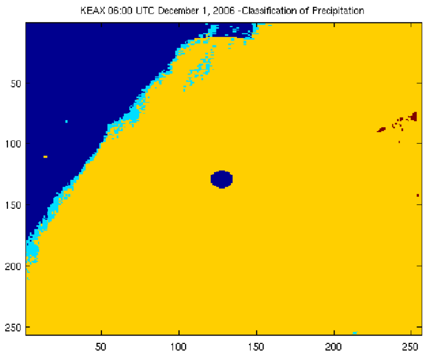

Figure 7b: *Precipitation classification for the radar image from KEAX at 06:00 UTC on December 1, 2006*

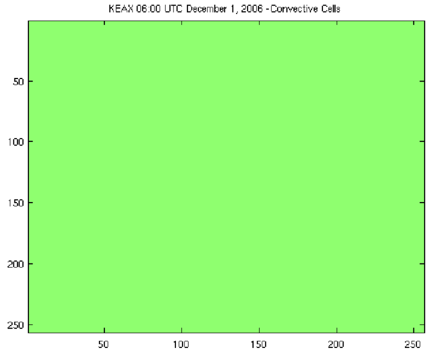

Figure 7c: *No cells identified within the radar image from KEAX at 06:00 UTC on December 1, 2006*

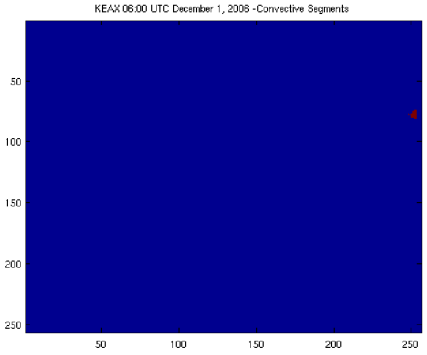

Figure 7d: *Segments identified within the radar image from KEAX at 06:00 UTC on December 1, 2006*

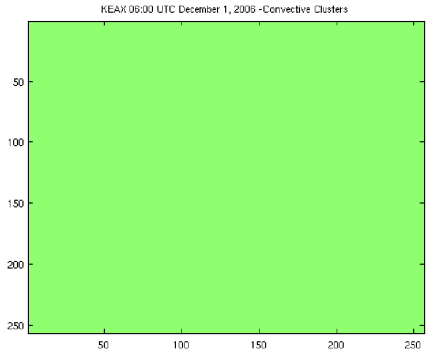

Figure 7e: *No clusters identified within the radar image from KEAX at 06:00 UTC on December 1, 2006*

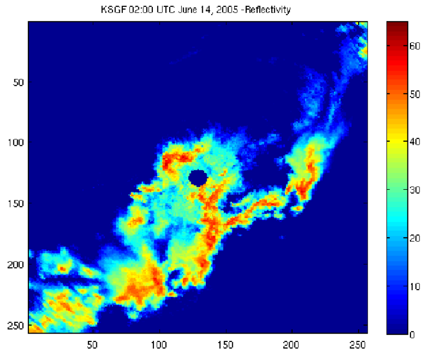

Figure 8a: *Radar reflectivity observed by KSGF at 02:00 UTC on June 14, 2005*

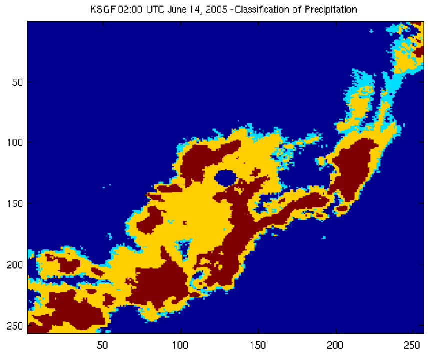

Figure 8b: *Precipitation classification for the radar image from KSGF at 02:00 UTC on June 14, 2005*

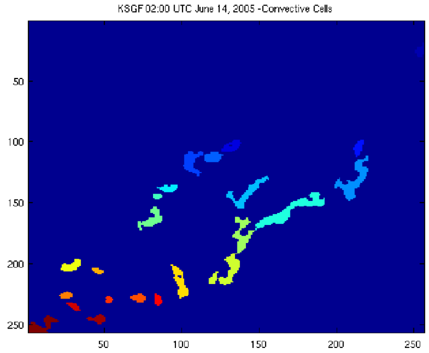

Figure 8c: *Cells identified within the radar image from KSGF at 02:00 UTC on June 14, 2005*

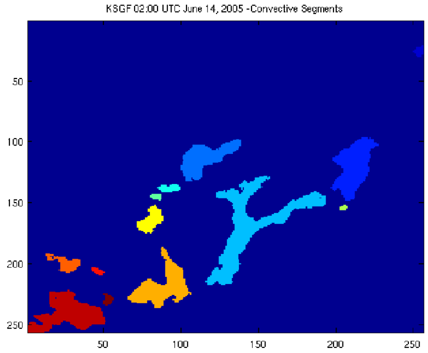

Figure 8d: *Segments identified within the radar image from KSGF at 02:00 UTC on June 14, 2005*

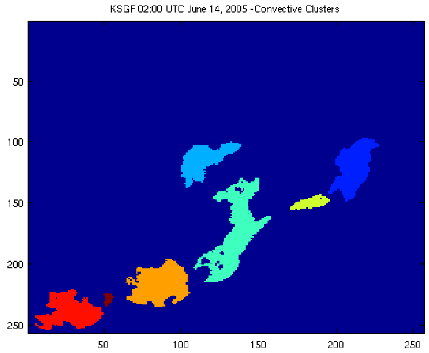

Figure 8e: *Clusters identified within the radar image from KSGF at 02:00 UTC on June 14, 2005*

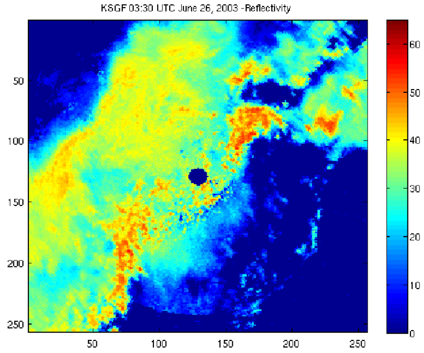

Figure 9a: *Radar reflectivity observed by KSGF at 03:30 UTC on June 26, 2003*

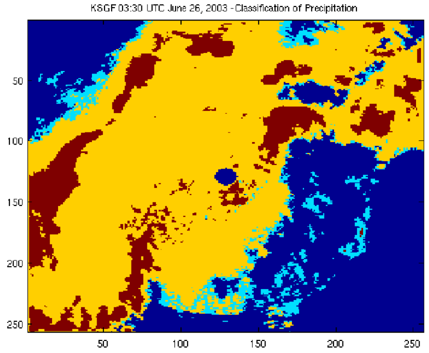

Figure 9b: *Precipitation classification for the radar image from KSGF at 03:30 UTC on June 26, 2003*

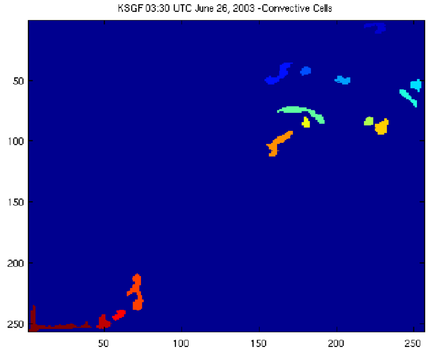

Figure 9c: *Cells identified within the radar image from KSGF at 03:30 UTC on June 26, 2003*

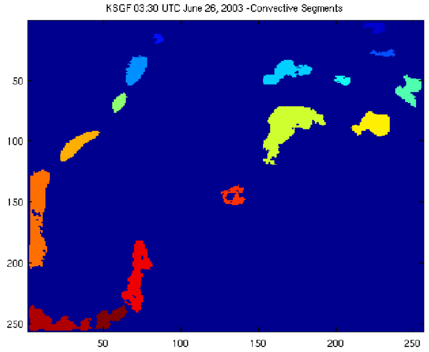

Figure 9d: *Segments identified within the radar image from KSGF at 03:30 UTC on June 26, 2003*

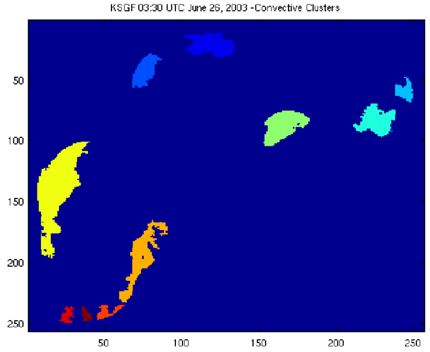

Figure 9e: *Clusters identified within the radar image from KSGF at 03:30 UTC on June 26, 2003*

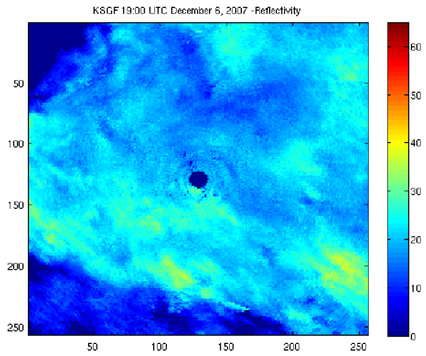

Figure 10a: *Radar reflectivity observed by KSGF at 19:00 UTC on December 6, 2007*

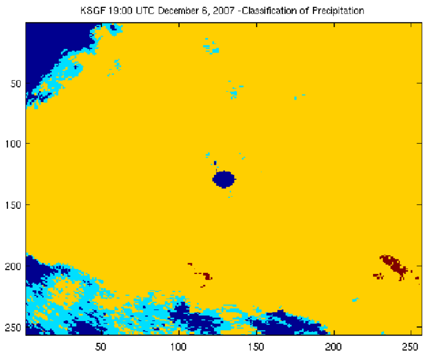

Figure 10b: *Precipitation classification for the radar image from KSGF at 19:00 UTC on December 6, 2007*

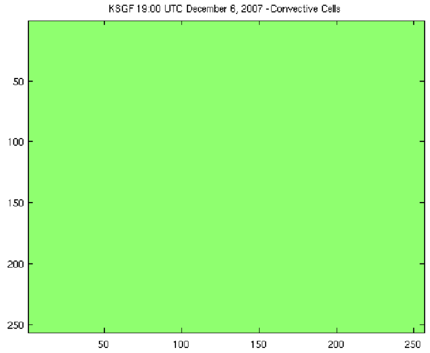

Figure 10c: *No cells identified within the radar image from KSGF at 19:00 UTC on December 6, 2007*

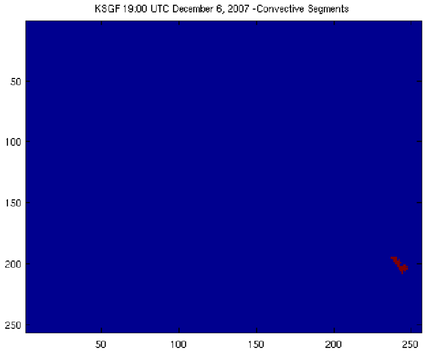

Figure 10d: *Segments identified within the radar image from KSGF at 19:00 UTC on December 6, 2007*

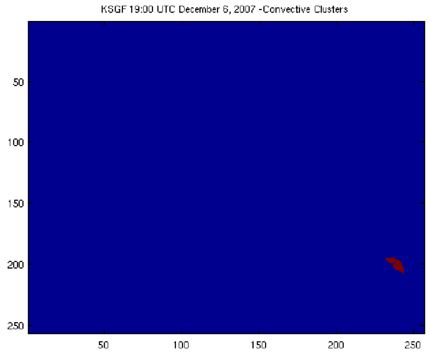

Figure 10e: *Clusters identified within the radar image from KSGF at 19:00 UTC on December 6, 2007*